2023

On The Gaussian-Core Vortex Lattice Model for The Analysis of Wind Farm Flow Dynamics

Apurva Baruah
Michigan Technological University, baruah@mtu.edu

ON THE GAUSSIAN-CORE VORTEX LATTICE MODEL FOR THE ANALYSIS OF WIND FARM FLOW DYNAMICS

By

Apurva Baruah

A DISSERTATION

Submitted in partial fulfillment of the requirements for the degree of

DOCTOR OF PHILOSOPHY

In Mechanical Engineering - Engineering Mechanics

MICHIGAN TECHNOLOGICAL UNIVERSITY

2023

This dissertation has been approved in partial fulfillment of the requirements for the Degree of DOCTOR OF PHILOSOPHY in Mechanical Engineering - Engineering Mechanics.

Department of Mechanical Engineering - Engineering Mechanics

Dissertation Advisor:	*Dr. Fernando Ponta*
Committee Member:	*Dr. Leonard Bohmann*
Committee Member:	*Dr. Hassan Masoud*
Committee Member:	*Dr. Kazuya Tajiri*
Department Chair:	*Dr. Jason Blough*

Dedication

To Mamma

Contents

List of Figures

List of Tables

Acknowledgments

First and foremost, it has been my privilege to work under the guidance of Dr. Fernando Ponta. I am grateful for his inspiration to pursue scientific research and for introducing the new passion of sailing in me. "*Muchas gracias*" falls immensely short of my full gratitude to you. *Skipper* Ponta has been a good friend and I shall forever cherish our adventures - both on and off the water. I sincerely thank my doctoral advisory commitee, Dr. Leonard Bohmann, Dr. Hassan Masoud, and Dr. Kazuya Tajiri for their feedback and time. The kindness, warmth, and assistance of Karen Bess and Cindy Wadaga are indispensable.

I'm grateful to Sandia National Laboratories for their financial support towards the development of this highly impactful scientific endeavor. I wish to thank the Department of Physics for providing me with the wonderful opportunity to teach undergraduate students. In addition to the sheer pleasure and joy of sharing Physics with first year students, their employment significantly supported my stay in Houghton. To the Department of Mechanical Engineering-Engineering Mechanics, I am extremely grateful for honoring me with the Alumni Fellowship. I'd like to acknowledge Dr.Predebon, Dr.Friedrich, and the ME-EM Alumni Board, particularly Marie Cleveland, for this award that provided invaluable financial backing of my scholarship. I'm extremely thankful to the Graduate School for supporting me with their GADI assistantship for

two years.

I'm indebted to Dr.Sunil Mehendale for his role during my early steps in the realm of scientific research. Your wisdom, philosophical and spiritual teachings have made me a better, life-long student of learning. I'm especially grateful to Dr.Pushpalatha Murthy. Your unwavering support, patience and mentorship have tremendously shaped my development as a holistic, responsible professional.

I would like to acknowledge and thank all the phenomenal teachers that I have met throughout my life. Especially from Lok Puram Public School - for laying the strong bedrock of my growth and success.

I'm grateful to the members of the WindGroup research team. You have been amazing colleagues and I thank you for the highly enriching discussions and constant support.

To all my friends - near and far, I am honored and humbled to receive your love and support. "*It takes a village*", and while I unfortunately can't fit all your names, you have my deepest and sincerest gratitude for uniquely and individually inspiring me all along.

Thank you also to my *Umrigar* family for your endless love.

Finally, Mamma - to you I owe it all.

Abstract

Wind power science has seen tremendous development and growth over the last 40 years. Advancements in design, manufacturing, installation, and operation of wind turbines have enabled the commercial deployment of wind power generation systems. These have been due, in a large part, to the expertise in the simulation and modeling of individual wind turbines. The new generation of wind energy systems calls for a need to accurately predict and model the entire wind farm, and not just individual turbines. The commercial deployment of these wind farms depends on model's ability to accurately capture the different physics involved, each at its respective scale, and then make accurate predictions of acceptable fidelity at a manageable computational cost.

The work presented in this dissertation extends the capabilities of a multi-physics suite to provide the capability to simulate the wakes of multiple turbines in a wind farm. By the implementation of a novel vortex lattice model, it enables the effective representation of the complex vortex wake dynamics of the turbines in a farm subject to transient inflow conditions. It explores the effect of different types of blades on the turbine wake. The goal is to obtain an accurate representation of the turbine-to-turbine wake interaction in a wind farm, which is demonstrated by simulations of two, four, nine and twenty turbine wind farms.

Chapter 1

Introduction

1.1 Wind energy overview

Since ancient times, humans have harnessed the wind in several ways - from wind mills that ground grain and pumped water, to the sailing vessels that shaped much of the world today. The foundations of the modern science of wind power generation have been laid by the pioneering efforts by Albert Betz and others in the early 20th century.

Initially considered a niche source of electricity generation, sustained research, development, and innovations have consistently increased the commercial adoptions of wind energy systems. The large-scale commercial deployment of wind turbines has

led to a decline in the levelized cost of energy (LCOE) [3]. These levelised costs for wind energy are a mere fraction of what they were almost half a decade ago and are competitive, without subsidies, with other *newly* installed sources of power generation. This has in turn led to an increase in the installation of wind energy systems across the globe.

This reduction in the LCOE has primarily been driven by advancements in wind turbine technology, particularly the increased hub-height, rotor diameter, and consequently, the rated power. These economies-of-scale factors have been augmented by innovations in wind turbine blades. Modern blades are sophisticated aerodynamic structures, manufactured using highly advanced materials and processes. The blades today also possess the modular capabilities of incorporating several after-market upgrades with relative ease. These developments have ensured that today's wind turbines are able to maximise power production while keeping costs low.

However, even with these advancements, some of the classical problems still remain. Especially the well-known "*square-cube law*" associated with the upscaling of wind turbines. For a particular wind speed, the mass of the rotor scales with the cube of the rotor radius (the *volume*) whereas the power generated scales with the square (rotor area). And even though the increasing costs can be balanced elsewhere in this large wind energy conversion system, future advancements are bound by this law.

Maximising the energy extraction process for the future calls for a holistic view of

all aspects of a wind power system. Developmental efforts need to be broadened to include not just single turbines, but the optimization of the collective wind farm, and moreover, the fleet of wind farms connected to the overall electricity grid. This calls for comprehensive analyses of the various multi-scale phenomena involved, beginning from the local flow and response of the turbines, to the complex flows through a wind farm, and finally the regional and global weather phenomena. To this end, the IEA Wind TCP has articulated the *Grand Challenges* ([4],[5]) that position wind power as the primary form electricity providing one-third to (potentially) one-half of the demand. The first grand challenge emphasizes the need for an improved understanding in the physics of the complex flows within wind farms. Simplification of complex physics involved has allowed for the proliferation of wind power plants, however, there are major gaps in our thorough understanding of all the underlying phenomena. This understanding is critical for ensuring the optimal design and operation of the next generation of wind farms.

1.2 Wind Farm Modeling and Simulation

Fundamental to the design of a wind farm is the understanding of the evolution, interaction and consequent impact, of the wakes of turbines in the farm. Intuitively, the presence of the wakes of upstream turbines significantly impacts the power production of downstream turbines. These wakes also lead to varying loads on the downstream

turbine. The complex wakes vary according to the size and type of turbine, and the prevalent wind and turbine operating conditions. Hence, their analyses is crucial in order to maximize energy production and lower the capital and operational costs.

Studying the wakes at scale, in "test" wind farms is impossible because of the uncontrollable, transient and spatially-varying nature of wind. Computational models and simulations are indispensable tools available for the understanding of the wind turbine wakes for the design and development of wind farms.

Several models have been developed for the analyses of the wind turbines wakes, from simplified, analytical models, to CFD techniques, like Reynolds-Averaged Navier-Stokes (RANS), Large Eddy Simulation (LES), and Direct Numerical Simulation (DNS). All of these have varying degrees of fidelity and associated computational costs. Typically, higher fidelity models tend to require more computational power - with DNS, despite its high-fidelity and least number of modeling assumptions, being practically intractable for wind-farm simulations. While LES has been a favored candidate in contemporary research, it still requires a large amount of computational resources (albeit far less than DNS).

One family of techniques that can fill this gap is Vortex Methods. Vortex methods do not involve the large number of simplifications inherent to low-fidelity models, and at the same time, do not require the large modeling and computational resources of conventional high-fidelity CFD-based techniques (LES). Belonging to the Lagrangian

framwork, vortex methods, in contrast of the Eulerian techniques, significantly reduces the computational requirements since the computations are performed only at the lagrangian markers. These lagrangian markers (or the nodes of the vortex filaments) are naturally tracked to along their evolution exactly where they are instead of the really large computational domain of conventional Eulerian techniques. These methods can compute the velocity field at any arbitrary location as a simple, independent post-processing operation. After a certain limit, the Eulerian (or grid-based) methods are completely ill-suited for such complex flows.

1.3 Focus of this study

Tremendous progress has been made in the design and development of diverse set of modeling tools that individually address the different multi-physics aspects of wind power systems. The structural dynamics of the turbine can be studied using reduced order models, modal analysis, and all the way up to complete 3D finite elements. The aeroelastic response of the blades can be studied using the models belonging to the BEM family, or 3D, coupled FSI codes. We've already seen the numerous flow models available in the previous section.

However, the continued growth in the deployment of new wind energy systems rests on the successful integration of the interlinked multi-scale physics. The coupling of

the aero-elasto-intertial physics of an individual turbine with the farm flow models is an indispensable step for any coupled multi-physics modeling system. With such a system, other aspects of the wind farm dynamics like the farm-collective control strategies involving the different electro-mechanical components, the farm microgrid, and ultimately the overall grid dynamics, can then be successfully included. This *unified* modeling framework shall enable the development and deployment of future wind farms.

The comprehensive modeling system needs to have the capabilities to solve all the non-linear, coupled, physics involved at their appropriate spatial and temporal scales - using manageable computational resources. Thus, the challenge is to develop a coupled, multi-physics, transient modeling system that can provide solutions of appropriate fidelity at a minimum computational cost.

Various modeling techniques integrate a subset of the different physics of wind energy systems, at varying levels of abstraction and fidelity. There are none that possess capacity to include all while being computationally economical. It is the aim of the current endeavor to develop a system on this unified paradigm. Building upon the existing Common ODE Framework (CODEF), and leveraging the capabilities of the Lagrangian, vortex-based methods, this dissertation describes the next leap in the development of modeling systems capable of capturing several aspects of a wind farm at a moderate computational cost.

1.4 Organisation of the Dissertation

In *Chapter 2* we shall discuss the multi-phyics, CODEF suite, its operation, and modular features that enable its expansion for the simulation of complex wind farm flows. We shall briefly visit the theoretical background of the existing single-turbine structural and aero-elasto-intertial modules - the Generalised Timoshenko Beam (GTBM) Model and the Dynamic Rotor Deformation-Blade Element Momentum (DRD-BEM) model. We also discuss some fundamental concepts of vorticity, and vortex methods.

In *Chapter 3* we shall describe the Gaussian-core Vortex Lattice Model (GVLM) implementation in CODEF. This new module expands CODEF's capabilities to simulate wind farms, in addition to its existing features to model the coupled, dynamic, transient response of wind turbine rotors with different control strategies.

In *Chapter 4* we present the numerical experiments conducted with the newly expanded CODEF suite. We begin with the preliminary verification of the GVLM using the NREL 5MW reference wind turbine. We shall provide the context for the different simulations conducted as part of our association with Sandia National Laboratories. This includes a description of their SWiFT facility in Texas, followed by details of their newly developed NRT blade, and the details of the instrumentation and data used for our comparative wake studies . And finally, a brief description of

the multi-turbine simulations as well.

In *Chapter 5* we present the results of our simulations with the turbines at the SWiFT facility. We shall discuss the results of the GVLM i.e. the wake of a turbine and its comparison with the *in situ* lidar measurements obtained from SWiFT. We shall also see the results of the effect of varying stiffness on the vortex wake, using the NRT blade and its several flexible variations, for different wind conditions.

In *Chapter 6* we present the results of twin-, NRT turbines in a tandem configuration. We shall describe the effect of the wake of the upwind turbine on the aeroelastic response and power production of the downwind rotor for different wind conditions. We shall also present the wake-to-wake interaction of the tandem twin-turbine configuration.

In *Chapter 7* we present results of the evolution and interaction of the wake of multiple turbines in a wind farm. These results showcase the capability of CODEF for easily simulating wind farms of different sizes. We present the results for wind farms consisting of four, nine and twenty turbines.

Finally, in *Chapter 8*, we present the conclusions of this dissertation and the outlook for future work.

Chapter 2

Theoretical Background

In this chapter we shall discuss CODEF, the multi-physics system whose capabilities have been expanded by the body of work presented in this dissertation. We shall briefly describe its underlying structural and aerodynamic modules that seamlessly integrate with the new module used for wind farm simulations. Finally we shall visit some concepts of vorticity and vortex wake models which form the basis for the vortex lattice model developed through the current endeavor.

2.1 The Common ODE Framework (CODEF)

CODEF is an adaptive, variable-timestep/variable-order ODE solver for wind turbine dynamics. The modularity of this *common framework* allows for easy integration of all the dynamic components of a wind turbine to solve a master ODE system. Aspects affecting the dynamics of the turbine like the rotor flow, blade structure, control system, and electro-mechanical device can be added to the feedback system in the form of modules comprised of their representative differential equations and

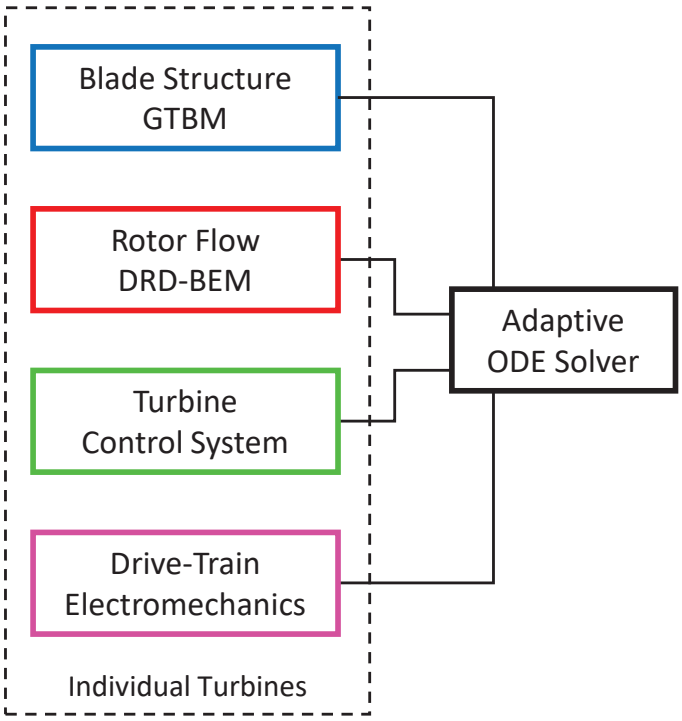

GTBM : Generalised Timoshenko Beam Model
DRD-BEM: Dynamic Rotor Deformation-Blade Element Momentum

Figure 2.1: Common ODE Framework for individual turbines.

modifications to the boundary conditions. CODEF thus is able to treat these modules individually while interfacing with them using a computationally efficient, non-linear, adaptive ODE routine. By monitoring the local truncation error at each time step, it integrates all the different multi-physics aspects of the problem, improving the efficiency and ensuring stability of the time marching numerical scheme. Figure 2.1 shows a flow-diagram of CODEF outlining the interrelations between the different modules.

Such modularity supports the independent development of the existing modules, and

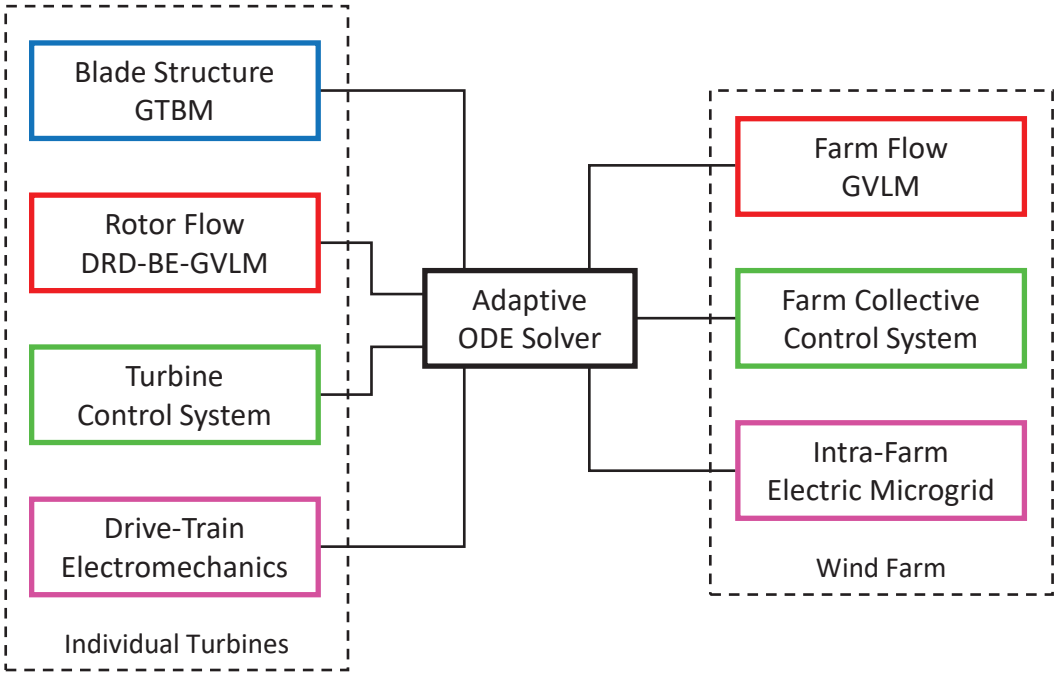

Figure 2.2: Common ODE Framework with expanded capabilities for farm simulations.

at the same time promotes the expansion of CODEF's capabilities. CODEF is perfectly suited for seamlessly interconnecting the dynamics of an individual turbine with new modules intended for the farm-scale flow, the wind-farm collective control system and the intra-farm microgrid. Figure 2.2 shows CODEF with the newly added capabilities to simulate wind farms.

Before discussing these expanded capabilties resulting from the current endeavor, let us briefly review the existing CODEF modules for an individual wind turbine.

2.2 Dynamic Rotor Deformation - Blade Element Momentum (DRD-BEM)

Wind turbines are complex structures that undergo highly dynamic, cyclical loads owing to the changing wind conditions. Factors that make a wind turbine an extremely complex system include the fluctuating loads on the wind turbine rotor, the coupled aero-structural-inertial behavior of the turbine blades, their interaction with the tower, and the control system of the turbine. Since these multi-physics parameters scale differently, the consistent upscaling of modern wind turbine rotors significantly limits the suitability of any wind-tunnel studies. This necessitates full-scale investigations which can only be accomplished using computer models. The challenge of

computer models is the large computational cost involved in solving a complex, transient, non-linear, and coupled multi-physics problem. Numerically this problem can be resolved either as some 3D model or involve some form of dimensional reduction techniques. Full 3D simulations are computationally demanding and severely limit the ability of an exploration of wide variety of cases/scenarios. Dimensional reduction techniques provide a healthy balance in adequately capturing the physics at a significantly reduced/acceptable computational effort.

Effective coupled reduced order models are able to alternate between the aerodynamic behavior and the structural response of the wind turbine blade. Such approaches typically model the turbine blade structure as a Bernoulli or Timoshenko beam - either using a discretisation method (like finite elements) or by a modal description using a limited number of deformation modes in the solution. The flow aspects are typically solved using the well-known Blade Element Momentum (BEM) model. Combining these two approaches leads to a coupled, non-linear scheme that represents all the complexities involved.

Proposed almost a century ago [6, 7], the BEM model[8, 9] is one of the most common tools used in the design and analysis of wind turbines. Over the years, several modifications [10, 11, 12] have been made improving the underlying main theoretical base.

In the classical BEM implementation, it is assumed that the blade sections are perpendicular to a radial line in the rotor's plane (refer figure 2.3). Hence, the classical BEM is unable to consider any misalignment of the turbine blade sections. This leads to significant misrepresentations of the coupled, dynamic, aeroelastic behavior of the rotor owing to inadequate capture of the large scale deformations and the aerodynamic forces - both affecting one another.

The novel BEM model forming the base of the current study is the Dynamic Rotor Deformation-Blade Element Momentum model (DRD-BEM). This model accounts for the aerodynamic effects of the misalignment of every blade section. It is achieved by the transformation of the velocity and force vectors across the different coordinate systems, from that of the free-stream wind to that of the blade section. These transformations are done by a set of orthogonal matrices that account for all the misalignments - including those brought about by the deformation of the blade, mechanical inputs like pitch and yaw, and even the pre-conformed misalignments like the pre-bend of the turbine blade.

Figure 2.3 shows a schematic view of the annular actuator swept by a blade element, its instantaneous position, and its span-wise length, δl, which are projected onto the hub coordinate system, h (figure 2.4). The actual area of the annular actuator swept by the blade element, defined by the radial thickness, δr_h, and the radius r_h, is constantly updated.

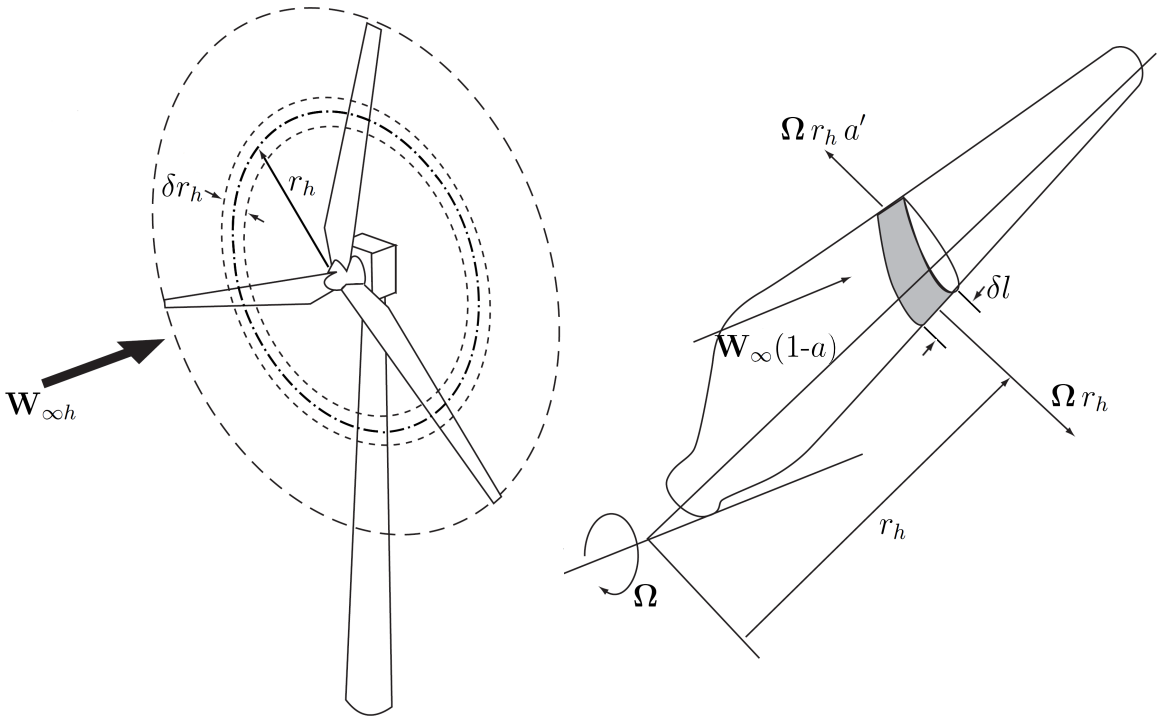

Figure 2.3: A schematic showing an annular actuator swept by a blade element (based on the classical BEM).

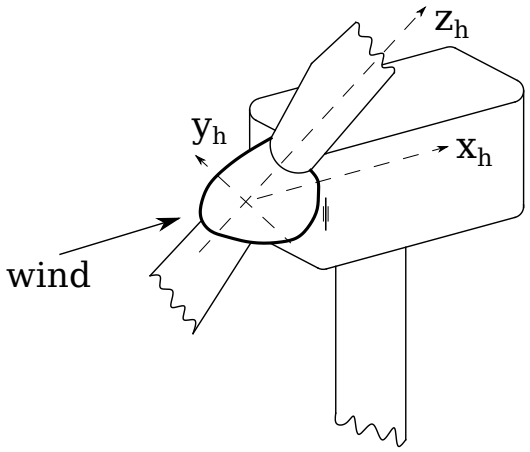

Figure 2.4: The hub coordinate system in accordance with the International Electrotechnical Commission (IEC) standards [1]

2.2.1 Blade Structural Model: The Dimensional-Reduction Technique

Wind turbine blades have complicated internal structures and heterogeneous material distribution [13], and hence are challenging to model using classical beam theories like the Standard Timoshenko Beam Model. Furthermore, blade analyses with classical beam theories can have significant errors due to *ad hoc* kinematic assumptions. The Generalised Timoshenko Beam Model (GTBM) was developed to account for these limitations. This sections briefly describes the advanced technique based on the GTBM used in DRD-BEM to capture and simulate the structural response of the blade. Detailed descriptions can be found in Ponta et al. [14] and Otero and Ponta [15].

GTBM, a dimensional reduction method, has the same parameters as the traditional Timoshenko model and can work for complex beams that may have twisted or curved shapes. In this model, originally introduced by Dr.Hodges [16, 17], the beam section does not remain planar after deformation and a 2D finite element mesh is used to interpolate the warping of the deformed section.

Figure 2.5 shows the GTBM model for a generic beam section and the reference-line, beam section and respective coordinate system before and after deformation. A

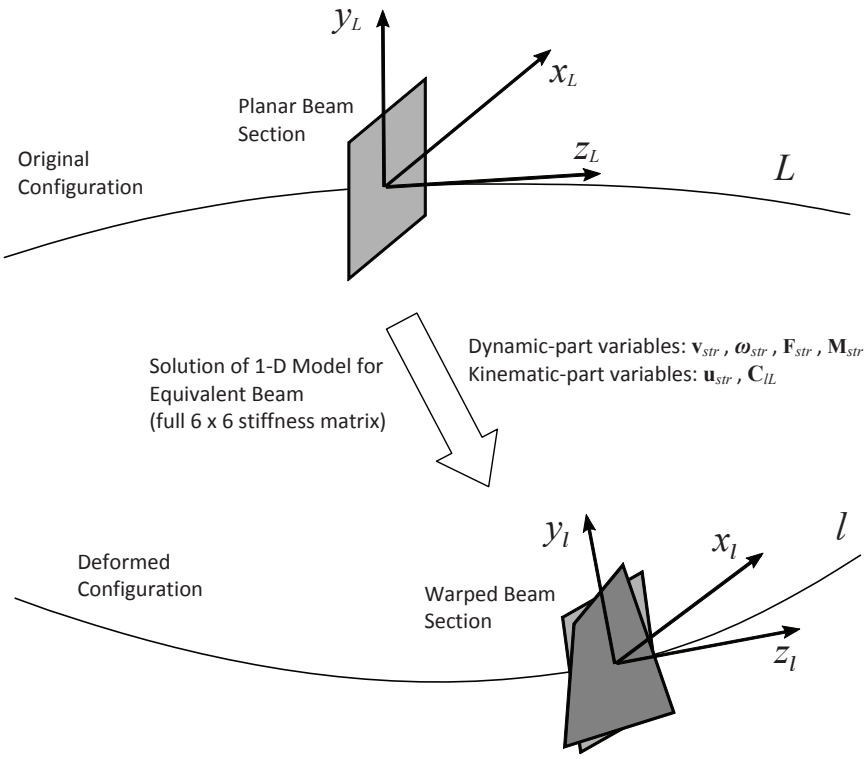

Figure 2.5: A schematic representation of GTBM where the reference line, the beam section and the coordinate system are shown before and after deformation.

mathematical formulation is used to write the 3D strain energy in terms of the classical 1D Timoshenko model. Therefore, the complexity of the 3D model and geometry of the blades are reduced into a stiffness matrix for the corresponding 1D beam which can then be solved along a reference-line, L, representing the beam's axis on the original configuration. This ensures a fully populated 6×6 symmetric stiffness matrix instead of only 6 stiffness coefficients obtained in the classical Timoshenko theory. Therefore, using the GTBM technique we can decouple a 3D nonlinear problem into a linear 2D analysis at the cross-sections and a nonlinear 1D unsteady beam problem which, for the aeroelastic analysis, we solve at each time step using an advanced ODE algorithm.

The 2D analysis computes the stiffness matrix and the 3D warping functions for the equivalent beam. After the 1D beam deformation for the ODE solution is acquired, the 3D strains, stresses and displacements for each blade section at different time steps can be obtained using the warping functions.

A new coordinate system (x_L, y_L, z_L) is introduced to represent the dynamic and kinematic variables along the reference line L, which can curve in any direction. This system follows the blade deformation into the instantaneous configuration l, becoming, x_l, y_l and z_l. Thus, the blade sections in the chord normal, chord-wise and span-wise directions stay aligned with the intrinsic system. Therefore, an accurate position tracking can be achieved by using this technique even in cases of large displacements or rotations of the blade section.

Inertia properties are also dimensionally reduced to produce a 6×6 inertia matrix for equivalent beam along the reference line L . This inertia matrix contains the moments of inertia of both first and second order for blade sections along the span. These are acquired from a 2D integration that operates over the area of each blade section and also considers the distribution of material properties and the details of blade section shape. This matrices operate on the linear and angular velocities giving the linear and angular momentum of the vibrational motion, and the inertia forces and moments association with them. We can also calculate the inertia forces of the rotation of the main shaft and mechanisms like pitch and yaw. Therefore, all parameters such as

angular, linear, centrifugal and acceleration effects are taking into account in a full 3D representation.

2.2.2 DRD-BEM Algorithm Summary

We begin with the velocity vector of the incoming flow aligned with the hub coordinate system h (the flow through an annular actuator). Its components are affected by the axial induction factor, a, which represents a decrease in the axial velocity across the actuator disk and the tangential induction factor, a', representing an increase in tangential velocity across the actuator disk.

$$\mathbf{W}_h = \begin{bmatrix} W_{\infty h_x}(1-a) \\ W_{\infty h_y} + \Omega\, r_h a' \\ W_{\infty h_z} \end{bmatrix}, \tag{2.1}$$

Equation 2.1 represents the velocity vector of the wind that is going through the annular actuator. $\mathbf{W}_{\infty h}$ is the undisturbed wind velocity in h coordinate system, Ω is the angular velocity of the rotor, and r_h is instantaneous radial distance (see figure 2.3). These three components of $\mathbf{W}_h$ show that the stream-tubes associated with the blades element are aligned with the wind direction in h system. The forces

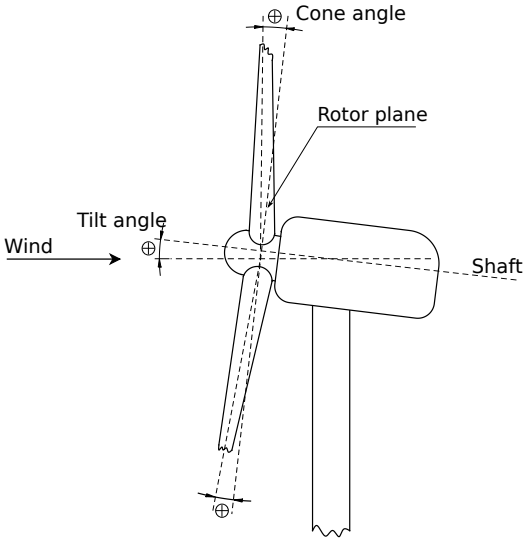

Figure 2.6: Cone angle θ_{cn} and tilt angle θ_{tlt} for upwind turbines, as given by the International Electrotechnical Commission (IEC) standards [1]

"exerted" by the annular actuator will change the path of flow particles and consequently, alter the path of the stream-tubes as well. The three dimensional $\mathbf{W}_{\infty h}$, takes into account the wind direction and the yaw angle changes by means of a set of orthogonal matrices that transform $\mathbf{W}_{\infty wind}$ into $\mathbf{W}_{\infty h}$. Here $\mathbf{W}_{\infty wind}$ represents the undisturbed wind velocity in a coordinate system aligned with the wind. The tilting matrix, $\mathbf{C}_{\theta_{tlt}}$, as defined by IEC standards [1], accounts for the vertical misalignment around the horizontal axis of the nacelle system (figure 2.6). The azimuthal orthogonal matrix, $\mathbf{C}_{\theta_{az}}$, transforms wind velocity into hub system by rotating the blade around main shaft to its instantaneous position. The orthogonal matrix, $\mathbf{C}_{\Delta\theta_{yaw}}$, considers misalignment between nacelle orientation and wind direction.

$$\mathbf{C}_{\Delta\theta_{yaw}} = \begin{bmatrix} \cos(-\Delta\theta_{yaw}) & \sin(-\Delta\theta_{yaw}) & 0 \\ -\sin(-\Delta\theta_{yaw}) & \cos(-\Delta\theta_{yaw}) & 0 \\ 0 & 0 & 1 \end{bmatrix}, \tag{2.2}$$

where $\Delta\theta_{yaw}$ is the difference of the direction between incoming wind direction and the nacelle orientation. The negative sign is due to positive definition of the *TS 61400-13 EIC:2001* for the $\Delta\theta_{yaw}$.

These matrices transform $\mathbf{W}_{\infty wind}$ to $\mathbf{W}_{\infty h}$:

$$\mathbf{W}_{\infty h} = \left(\mathbf{C}_{\theta_{az}}\mathbf{C}_{\theta_{tlt}}\mathbf{C}_{\Delta\theta_{yaw}}\mathbf{W}_{\infty wind}\right). \tag{2.3}$$

$\mathbf{W}_h$ subsequently undergoes coordinate system transformation from the hub coordinate system to the system aligned with the blade section. First, the matrix $\mathbf{C}_{\theta_{cn}}$, which represents the coning angle for the rotor. The coning angle could either be fixed (like NREL 5MW reference wind turbine [18]) or a variable matrix that is based on a real-time turbine operation control. For a detailed description of the concept of coning rotors see Crawford [10], Jamieson [19], Crawford and Platts [20]. Next is the pitching transformation matrix, $\mathbf{C}_{\theta_p}$, which takes into account the pitching angle and is associated with the rotation of the blade around the pitch axis.

$$\mathbf{C}_{\theta_\mathbf{p}} = \begin{bmatrix} \cos(-\theta_p) & \sin(-\theta_p) & 0 \\ -\sin(-\theta_p) & \cos(-\theta_p) & 0 \\ 0 & 0 & 1 \end{bmatrix}, \tag{2.4}$$

Pitch angle at each section θ_p, is the sum of fixed pitch angle at the hub, θ_{p_0} and $\theta_{p_{ctrl}}$ which can be varied by the turbine's control system. The sign of the pitch angle is also based on IEC standards definition.

Two more transformation matrices are still needed. The first set is based on the geometrical alignment of the blade sections when the blades were manufactured such as pre-bending. $\mathbf{C}_{Lb}$ takes into account these characteristic for each position along the L . The next orthogonal matrix,$\mathbf{C}_{lL}$, comes from the kinematic equation solution of the structural model, which takes into account the instantaneous deformation of each blade section. After the application of these orthogonal matrices, the velocity vector $\mathbf{W}_h$ is now represented in the coordinate system of the blade section. Then two other parameters are added, $\mathbf{v}_{str}$ and $\mathbf{v}_{mech}$, which are blade section vibrational velocities coming from structural model and the motion of the blade section caused by mechanical devices (such as yaw, azimuth, pitch). Since these parameters are already in the l coordinate system so the wind velocity relative to the blade section, $\mathbf{W}_l$ is:

$$\mathbf{W}_l = \left(\mathbf{C}_{lL}\mathbf{C}_{Lb}\mathbf{C}_{\theta_p}\mathbf{C}_{\theta_{cn}}\mathbf{W}_h\right) + \mathbf{v}_{str} + \mathbf{v}_{mech}. \tag{2.5}$$

The lift and drag forces per unit length of span can be found by using the magnitude of this relative wind velocity (2.6), $W_{rel} = \sqrt{W_{l_x}^2 + W_{l_y}^2}$, and angle of attack, α.

$$dF_{lift} = \frac{1}{2}\rho\, C_l\, W_{rel}^2\, c\,, \qquad\qquad dF_{drag} = \frac{1}{2}\rho\, C_d\, W_{rel}^2\, c, \tag{2.6}$$

where C_l is the lift coefficient, and C_d is the drag coefficient, depend on the airfoil profile and the angle of attack, α; c is the chord length, and ρ is the air density. This eventually gives us the aerodynamic load on the blade element as:

$$\delta\mathbf{F}_{rel} = \begin{bmatrix} dF_{lift} \\ dF_{drag} \\ 0 \end{bmatrix} \delta l, \tag{2.7}$$

$\delta\mathbf{F}_{rel}$ can be transformed back to the h coordinate system using the inverse of the same orthogonal matrices. Since the inverse and transpose of orthogonal matrices are the same, the load $\delta\mathbf{F}_{rel}$ on the blade element in h coordinate system is:

$$\delta \mathbf{F}_h = \mathbf{C}_{\theta_{cn}}^T \mathbf{C}_{\theta_p}^T \mathbf{C}_{Lb}^T \mathbf{C}_{lL}^T \mathbf{C}_{Lthal}\, \mathbf{dF}_{rel}\, \delta l, \tag{2.8}$$

In equation 2.8, $\mathbf{C}_{Lthal}$ is the matrix that projects lift and drag forces onto the blades section's chord-wise and chord-normal direction, aligned with the coordinate system l.

Based on Equation 2.7, since:

$$\delta \mathbf{F}_h = \begin{bmatrix} \delta F_{h_x} \\ \delta F_{h_y} \\ \delta F_{h_z} \end{bmatrix} = \begin{bmatrix} dF_{h_x} \\ dF_{h_y} \\ dF_{h_z} \end{bmatrix} \delta l, \tag{2.9}$$

where $\mathbf{dF}_h = \mathbf{C}_{\theta_{cn}}^T \mathbf{C}_{\theta_p}^T \mathbf{C}_{Lb}^T \mathbf{C}_{lL}^T \mathbf{C}_{Lthal}\, \mathbf{dF}_{rel}$, the equation 2.8 can be written as $\delta \mathbf{F}_h = \mathbf{dF}_h\, \delta l$.

In this step, each component of $\delta \mathbf{F}_h$ from blade elements theory is equated to the change of momentum through the corresponding annular actuator.

δF_{h_x}, normal to the annular actuator, is equal to the change in momentum on $W_{\infty h_x}$ associated with axial interference factor a (equation 2.1) and δF_{h_y}, the tangential component, is equal to the change in the momentum on $W_{\infty h_y}$ associated with tangential induction factor a'. Once the solution for a and a' in the previous steps has converged,

we can calculate the aerodynamic forces on each blade section. Equation 2.10 and equation 2.11 shows the calculation of dF_{h_x} and dF_{h_y}.

$$dF_{h_x} = f_{th} \frac{4\pi\,\rho\,r_h}{B} \left(W^2_{\infty h_x}\, a\,(1-a) + (a'\Omega\,r_h)^2 \right) \frac{\delta r_h}{\delta l}, \tag{2.10}$$

$$dF_{h_y} = f_{th}\, \frac{4\pi\,\rho\,r_h}{B}\, |W_{\infty h_x}|\,(1-a)\,(\Omega\,r_h)\,a'\,\frac{\delta r_h}{\delta l}. \tag{2.11}$$

f_{th} represents the loss tip and hub loss factors, and B represent the number of blades. $\frac{\delta r_h}{\delta l}$ transforms δl into δr_h coordinate system using the orthogonal matrices previously mentioned. The $(a'\Omega\,r_h)^2$ term takes into account the actuator pressure drop, for more information see [14].

Since a and a' are the unknowns in equations (2.10) and (2.11), these equations are solved by using an initial guess value for each blade element.

After finding the a and a', by repeating the $\mathbf{dF}_{rel}$ calculation, we can find the aerodynamic forces by transfer them into the l coordinate system by using this equation :

$$\mathbf{dF}_l = \mathbf{C}_{Lthal}\,\mathbf{dF}_{rel} \tag{2.12}$$

A detailed description of the implementation of the DRD-BEM model can be found in Ponta et al. [14] and the references therein. Menon and Ponta [21] reports results of the DRD-BEM applied to the analysis of the aeroelastic dynamics of rotors undergoing rapid pitch-control actions, and Otero and Ponta [22] uses the model to analyze the effects of blade-section misalignment on rotor cyclic loads. Ponta et al. [14] and Otero and Ponta [15] contain the details of the structural model. Additionally, Ponta et al. [14] also includes results of the DRD-BEM model applied to the analysis of vibrational modes of composite laminated wind-turbine blades, together with validation results against the works of Jonkman et al. [18] and Xudong et al. [23].

2.3 Vorticity and Vortex Methods

Vorticity, ω of the fluid at the point considered is the vector curl $\mathbf{V}$,

$$\omega = \text{curl } \mathbf{V} \tag{2.13}$$

The *circulation* Γ around any closed curve $\mathscr{C}$ and vorticity are related by the following equation,

$$\Gamma \equiv \oint_{\mathscr{C}} V \cdot \mathbf{ds} = \iint_{S} \text{curl } \mathbf{V} \cdot \mathbf{n} \; dS$$
$$= \iint_{S} \omega \cdot \mathbf{n} \; dS \tag{2.14}$$

where S is any (capping) surface whose boundary is the curve $\mathscr{C}$.

The field lines of the vorticity field are called *vortex lines*. They are described as

$$\omega \times \mathbf{ds} = 0 \tag{2.15}$$

where **ds** is an element of a vortex line. At any point in the fluid field, the direction of the vorticity vector is given by the direction of the vortex line passing throught that point.

If we consider a closed curve and draw all the vortex lines passing through it, a *tube* is formed. Such a tube is called a *vortex tube*. A vortex tube of infinitesimal cross-sectional area is known as a *vortex filament*. The circulation, Γ, around any closed curve embracing a vortex tube (or line/filament), is a characteristic of the tube as a whole and is called the *strength of the vortex tube (or line/filament)*.

2.3.1 Velocity Induced by a Vortex Filament : Biot-Savart Law

Consider a vortex filament of strength Γ. As per the Biot-Savart law, the velocity induced at any point $\mathbf{r}$ by the vortex element of cross-sectional surface $\mathbf{n}\ dS$ and length $\mathbf{dl}$,

$$\delta\mathbf{V} = \frac{\Gamma}{4\pi}\int \frac{\mathbf{dl}\times(\mathbf{r}-\mathbf{s})}{|\mathbf{r}-\mathbf{s}|^2} \tag{2.16}$$

This presents us with the following three conditions:

a. An infinitely long vortex filament For an infinitely long vortex filament, the velocity induced at a point which is at a normal distance of h from it, is given by

$$\mathbf{V} = \frac{\Gamma}{4\pi h}\mathbf{e} \tag{2.17}$$

where $\mathbf{ds}$ is an element of the filament located at $\mathbf{s}$ and $\mathbf{e}$ denotes the direction of $\mathbf{ds}\times(\mathbf{r}-\mathbf{s})$ as seen from Figure 2.7.

b. A semi-infinite vortex filament For a semi-infinite vortex filament, the velocity

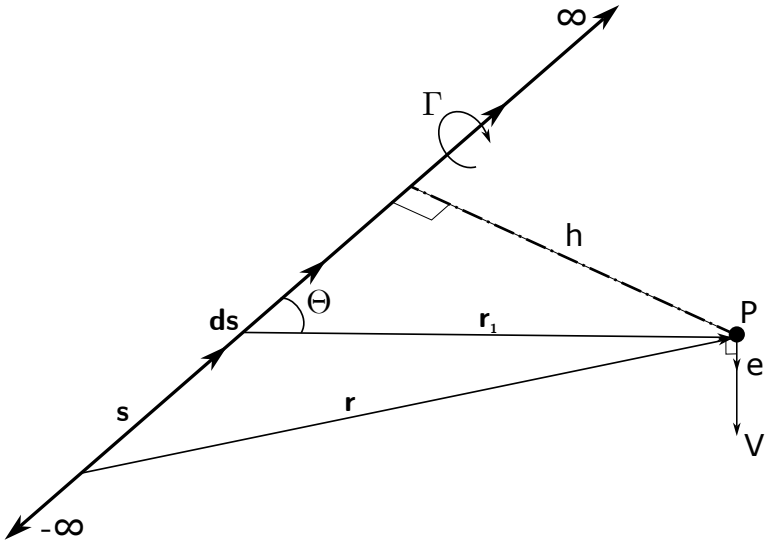

Figure 2.7: Velocity induced on a point by an infinitely long vortex filament.

induced is obtained as

$$\mathbf{V} = \mathbf{e}\frac{\Gamma}{4\pi h}(1 + \cos\theta_0) \tag{2.18}$$

c. A Finite vortex filament And finally, or a vortex filament of finite length, the induced velocity is

$$\mathbf{V} = \mathbf{e}\frac{\Gamma}{4\pi h}(\cos\theta_1 + \cos\theta_2) \tag{2.19}$$

Result 2.19 forms the basis of the vortex system used in the representation of the blade elements in vortex lattice methods.

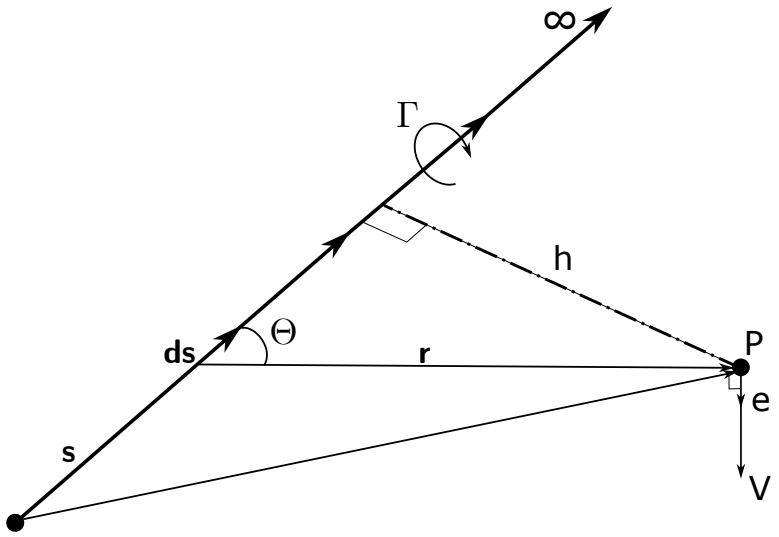

Figure 2.8: Velocity induced on a point by a semi-infinite vortex filament.

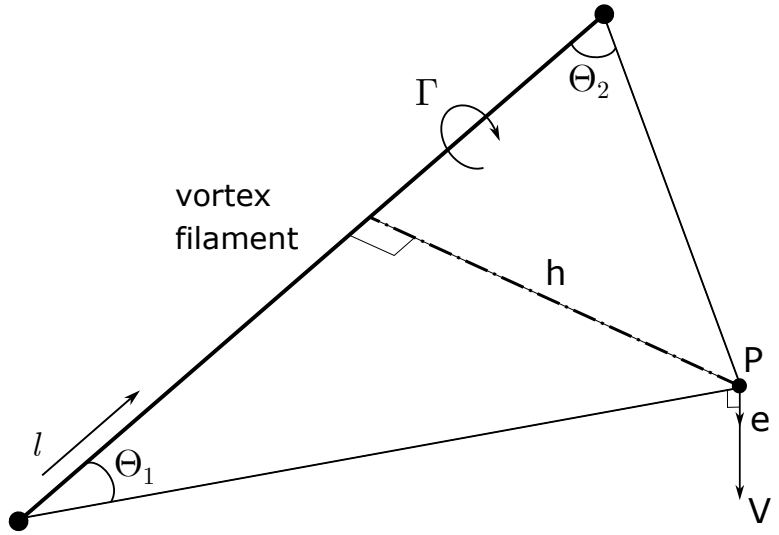

Figure 2.9: Velocity induced on a point by a vortex filament of finite length.

2.3.2 Vortex Methods

Vortex methods were initially developed for helicopter applications [24] [25]. However, these early methods suffered from numerical convergence with their time marching schemes. This led to the development of prescribed vortex wake methods which were used for wind turbine applications as well. Despite being simple and computationally efficient, the assumption / a priori specification of the position of the vortex elements from experiments, limits the application of such formulations.

In contrast to the prescribed wake methods, free vortex methods do not require the positions of the vortex elements be specified/known. Under this model, the vortex elements are freely allowed to distort according to the existing velocity field. At each time step, the wake positions are calculated using the Biot-Savart law to obtain the induced velocities. These methods rely on the representation of the turbine blades by a set of vortex filaments or vortex "blobs".

In the case of the *lifting line* model, the blade section/element is replaced by a bound vortex filament. Spanwise vortex filaments are shed at each time step and are assumed to remain straight, with their ends being convected with their local fluid velocities. Hence, these filaments may stretch, translate and rotate over time. At the end of each blade element, a trailing vortex filament is shed as a consequence of the Helmholtz

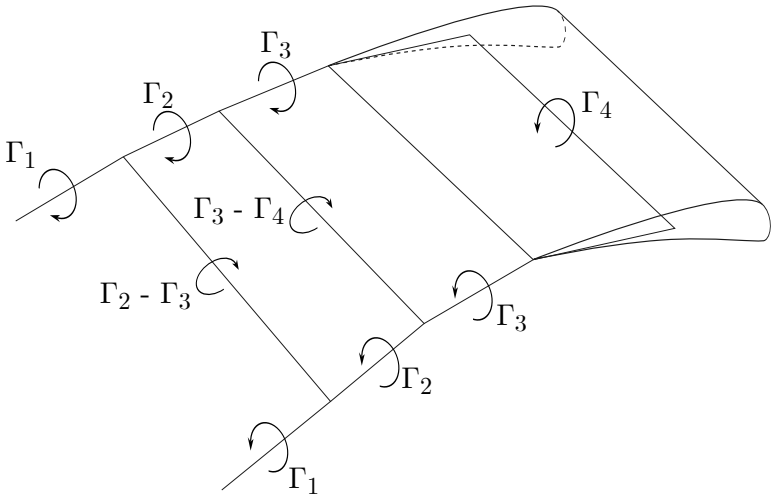

Figure 2.10: Vortex lattice of a single blade element.

theorem of vorticity. This results in the shedding of a system of vortex *filaments* whose end points constitute the nodes of a *vortex lattice*. Figure 2.10 shows the bound, shed and trailing filaments associated with a single blade element.

Chapter 3

The Gaussian-Core Vortex Lattice Model

In this chapter we shall discuss the implementation of the Gaussian-core Vortex Lattice Model (GVLM) in the CODEF environment. We shall describe aspects of the GVLM implementation that lead to an accurate representation of the complex dynamics of a wind turbine wake and those of several turbines in a farm.

3.1 Vortex Formation, Evolution and Transport

3.1.1 Gaussian-core model

The Biot-Savart formulation is an idealised model. 2.19 indicates that as the point moves closer to the filament, the induced velocity increases dramatically and becomes infinite (indeterminate) if it lies on the filament itself $\sim$ which is completely unrealistic. In fact, the velocity induced by a vortex filament on itself is zero.

The solution proposed by [26] (Chap. XI, Art. 334a), known as the Lamb Vortex model, provides a realistic representation of the vorticity. This Gaussian vorticity distribution is given as

$$\omega = \frac{\Gamma}{4\pi\nu t}(e^{-r^2/4\nu t}) \tag{3.1}$$

And the corresponding induced velocity is given by

$$\mathbf{V} = \frac{\Gamma}{2\pi r}(1 - e^{-r^2/4\nu t}) \tag{3.2}$$

At any instant of time, $\mathbf{V}$ is maximum for a radius r_c such that

$$\begin{aligned} \frac{{r_c}^2}{4\nu t} &= 1.26 \\ i.e. \qquad r_c &= 2.245\sqrt{\nu t} \end{aligned} \tag{3.3}$$

Along with this Gaussian distribution of vorticity, the viscous core expands due to diffusion thereby resulting in a better representation of the vortex evolution process. [27] provides a comparison between direct numerical simulation and experimental data of the effect of viscosity on the vorticity distribution and its rate of decay in a Karman vortex street behind a circular cylinder. By decomposing the incompressible velocity field in the frame of reference of the cylinder into its solenoidal and harmonic components, it is demonstrated that the vortex cores exhibit a Gaussian vorticity profile and the peak vorticity in the core decays downstream with a hyperbolic decay rate which can be determined by the amount of circulation contained in the core in the early stages of the street. This determination is particularly useful in the development of vortex lattice methods as it ensures a realistic representation of vortex decay and the interactions of the vortex filaments.

Figure 3.1 shows the Gaussian vorticity distribution and Figure 3.2 shows the corresponding induced velocity of filaments of an arbitrary strength and different viscous core radii.

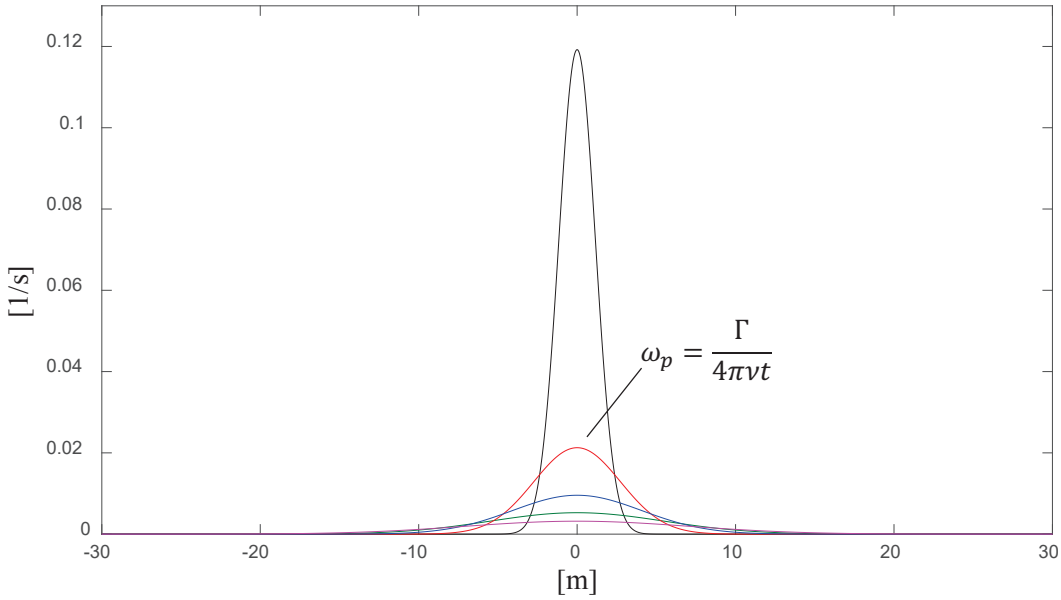

Figure 3.1: Gaussian distribution of a generic vortex filaments of arbitraty strength and different core radii.

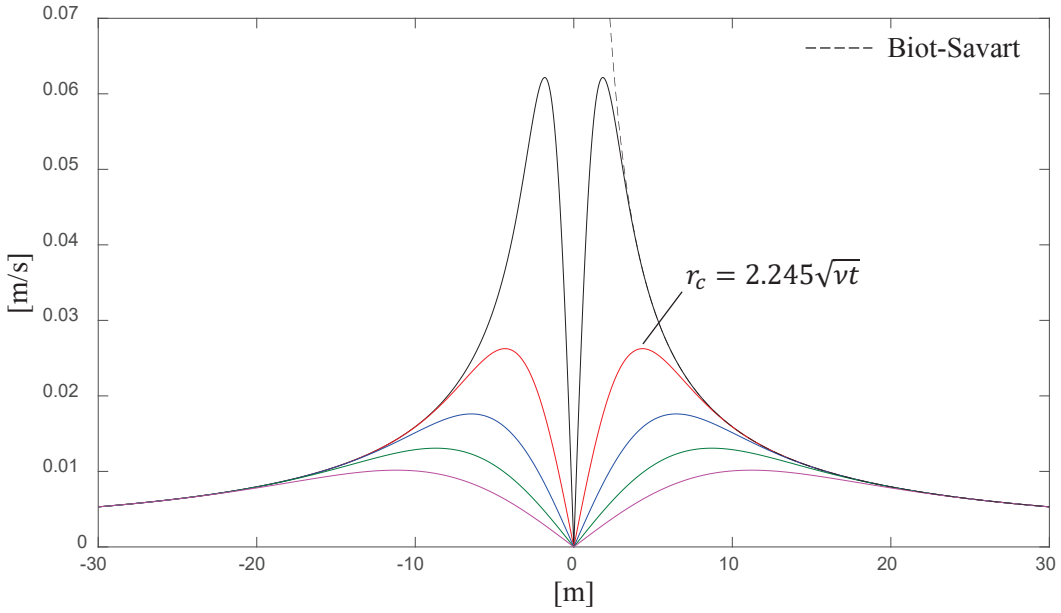

Figure 3.2: Induced velocity by Gaussian filament of arbitrary strength and different core radii.

The following two key features of the Gaussian-core model enable its use for accurate representation of the underlying physics:

1. The Gaussian distribution of vorticity enables the representation of the natural viscous decay of the vortex filaments. This allows the free-up of the memory from vortices that have significantly "dissipated" or "*aged*"

2. The Guassian distribution also avoids the mutual high-speed satellisation of vortex filaments in close proximity thereby avoiding unrealistically high tangential velocities. This ensures the stability of the vortex lattice which enables it to be extended to large distance downstream of the rotor.

3.1.2 Viscous Core Radius and Turbulent Diffusivity Coefficient

From 3.2, it can be seen that the swirl velocity at the time of the creation of the vortex filament is singluar, and this leads to unrealistically high velocities at young vortex ages. Furthermore, the core growth rate obtained from 3.3 is unrealistically slow. In order to address these, a finite viscous radius core, R_{VorCre} is implemented. We currently define the R_{VorCre} on the thickness of the airfoil section of the blade element/vortex filament. The blade section airfoil's thickness can be suitably scaled to obtain the R_{VorCre}.

In addition to this unique implementation of R_{VorCre}, there is a need to augment the viscosity to account for the turbulent eddy viscosity in the inflow. To this end, we introduce the *Turbulent Diffusivity Coefficient*, ν_T as a replacement for the original viscosity ν. This ν_T affects both, the diffusion of the vortex core and the vortex filament decay process.

Very much akin to the k-*epsilon* model, it can be seen that the current Gaussian-core implementation involves two *tunable* parameters - the vortex filament's viscous core radius at the time of creation, R_{VorCre} and the turbulent diffusivity coefficient, ν_T. These parameters are based on the wind turbine blade, the operational conditions and the inflow inputs to the model. Of particular care is the choice of ν_T since it must also consider the inflow inputs - specifically how the inflow turbulence is introduced in the model. This can be thought to be similar to the modeled and resolved scales of turbulence for contemporary LES codes.

3.1.3 Vortex Transport and Stretching

The Lagrangian markers or the "nodes" of the vortex filaments, are convected through the flow field which causes strain in the vortex filaments. The stretching (or contraction) of the vortex filaments in turn modifies the vortex filament core and ultimately

the induced velocities. Since the flow is incompressible, the net circulation of any filament remains constant. In the current implementation, the vorticity is assumed to be concentrated inside a corresponding cylinder of its viscous core radius, and length equal to the length of the filament. The conservation of this filament "volume" provides the change in the radius due to the change in length of the filament. This modified core radius is then used to compute the induced velocities by the stretched vortex filaments.

The lagrangian markers are convected at the local fluid velocities. This velocity is the vector sum of the free stream velocity (including any external sources of disturbance/perturbance), U_{wind} and the velocity induced by the vortex wake, U_{ind} i.e.

$$\mathbf{U} = \mathbf{U}_{wind} + \mathbf{U}_{ind} \tag{3.4}$$

where U_{ind} for each node is obtained as the resultant of the velocity induced on it by all the filaments in the lattice given by

$$\mathbf{U}_{ind} = \frac{\Gamma}{4\pi h}(1 - e^{-r^2/4\nu_T t})(\cos\theta_1 + \cos\theta_2) \tag{3.5}$$

The propogated/advected positions of the filament nodes are obtained from the 2nd

order explicit Adams-Bashforth (AB2) time integration:

$$\Delta x_i = \left[\frac{3}{2}(\mathbf{U}_i)_{t_{curr}} - \frac{1}{2}(\mathbf{U}_i)_{t_{prev}}\right]\Delta t \tag{3.6}$$

Being an "open" method, the AB2 scheme is conditionally stable and offers an acceptable trade-off between stability, accuracy, and computational cost. Hence it is suitable for the simulation of the vortex wakes of multiple wind turbines in a wind farm.

3.2 Gaussian-core Vortex Lattice Model

The GVLM combined with CODEF's blade structural and rotor flow models leads to highly accurate farm simulations when compared to traditional BEM-based codes but at significantly reduced computational costs when compared to DNS/LES codes. The general approach of a vortex lattice technique involves the division of the wind turbine blade into a number of segments/elements along their span. This blade element is represented by the *bound* vortex filament. The use of a single bound vortex to represent the blade element adequately represents the flow field at distances greater than one chord length from the airfoil.

The strength of this bound vortex filament, Γ_{Bn} is obtained using the Kutta-Joukowski theorem. At each time step, DRD-BEM provides the accurate angle of attack, α of the blade section, and, consequently its aerodynamic coefficients. With the accurate coefficient of lift, C_l, using the Kutta-Joukowski theorem, we obtain Γ_{Bn} as

$$\Gamma_{Bn} = \frac{1}{2} U_{rel} C_l c \tag{3.7}$$

where U_{rel} is the local relative velocity for the airfoil section, and c is the airfoil section chord.

From the Helmholtz theorem, the strength of the *trailing* filament is equal to the bound filament. The strength of the *shed* filaments is equal to change in the bound filament as per Kelvin's theorem. Figure 3.3 shows the vortex *"lattice"* consisting of the Bound, Shed and Trailing filaments of a generic turbine blade. The intensities of the *ith* shed and trailing filaments associated with the current time step j are obtained from the bound filaments as below:

$$\Gamma_{Sh_i}^{j-1} = \Gamma_{Bn_i}^{j-1} - \Gamma_{Bn_i}^{j} \tag{3.8}$$

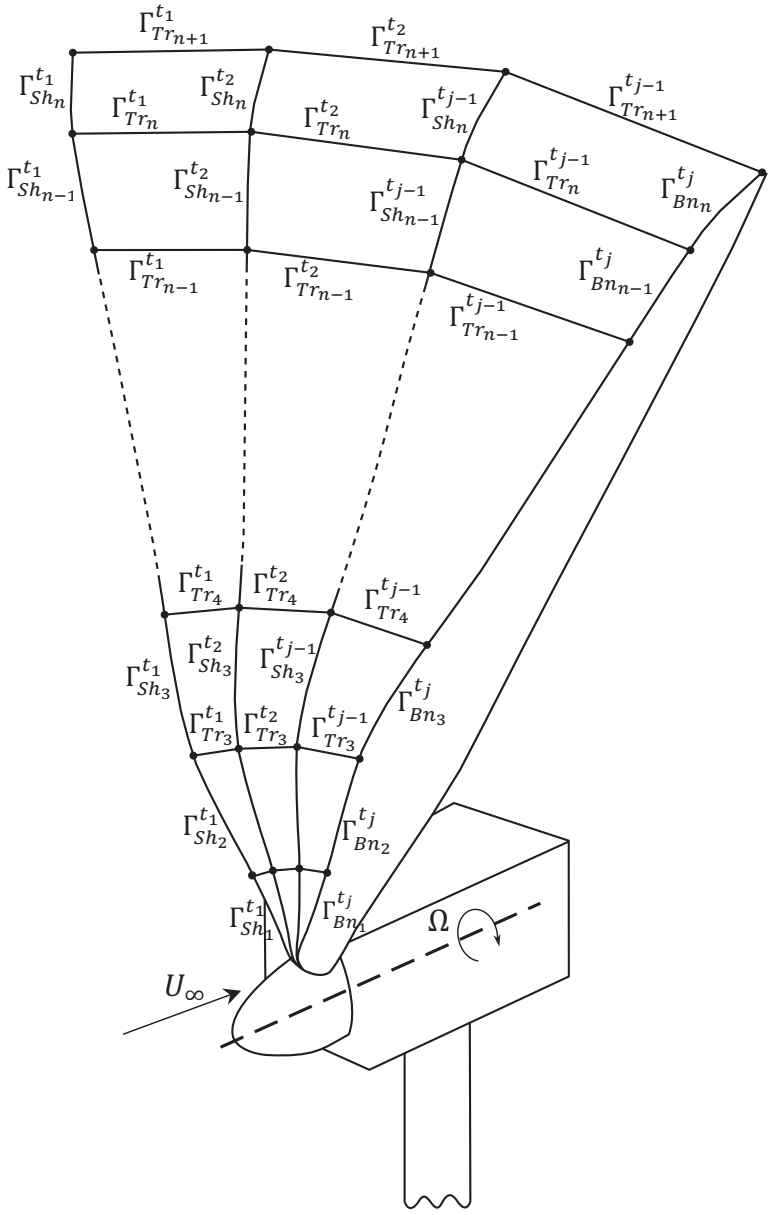

Figure 3.3: A schematic showing an bound, trailing and shed vortex filaments from a generic wind turbine blade.

$$\Gamma^{j-1}_{Tr_i} = \Gamma^{j}_{Bn_i} - \Gamma^{j}_{Bn_{i-1}} \tag{3.9}$$

At every time step, the induced velocity for every filament node is obtained by obtaining the induction from all the other filaments of the vortex lattice. In this manner, a system of shed and trailing vortex filaments is created and convected.

This implies that as the vortex shedding process progresses, the *vortex lattice* extends with time. This leads to an increase in computational time per time step. We manage this increase through several ways discussed in the following subsections.

3.2.1 Lattice Wake Growth

In the current implementation of GVLM, the time step of the aeroelastic solver, DRD-BEM and the vortex wake module, GVLM are different but coupled. The method retains the capability of shedding a vortex filament system at every aeroselastic time-step but such small time steps could lead to a vortex lattice with a large number of filaments. For the purpose of studying the wake of the turbine and its interaction with other turbines in the farm, such large vortex lattice ensembles are superfluous and render the method computationally prohibitive. Furthermore, the scales of the vortex dynamics phenomena of interest do not necessitate such numerous steps. Small scale phenomena can be represented very effectively through model parameters like ν_T, akin to the sub-grid scale modeling in LES. Hence, having different time steps effectively compartmentalizes the two different, yet closely-related, aspects of the overall

simulation. Currently, the vortex shedding process takes places upon completion of a certain number of DRD-BEM steps. This relationship can be implicitly or explicitly specified as inputs to the solver.

3.2.2 Lattice Wake Size

Since the GVLM is a lagrangian method, the domain is essentially infinite. The "mesh" points/nodes are computed and solved exactly when and where necessary. However, the growth of the vortex lattice at every time step necessitates a finite limit. In the current implementation, we cap the growth of the lattice at a certain number of shedding events/time-steps. This number can be implicitly or explicitly specified as an input. Beyond this maximum number, the vortex filaments are deleted. The choice of this maximum lattice size is a balance of the domain required for an appropriate/acceptable description of the vortex wake and the computational expense incurred. Some of the factors considered in arriving at this limit include the age and distance downstream of the filaments, the operating conditions including the input wind conditions, turbine operation parameters, and the location of the vortex wake filaments.

3.2.3 Computational Approaches

The framework of GVLM's mathematical and computational representation inherently supports parallelisation of the induced velocities calculations. The current computational structure enables the parallel computation of vortex wakes of the individual blades of each turbine. This choice has been based on maximising the use of the current type and trend of multi-core CPU hardware available, and the accompanying software improvements like AVX routines etc. This enables the simulation of a large number of turbines in a wind farm on a workstation computer - as opposed to the requirement of large computational clusters for a corresponding LES of comparable fidelity. It must be noted that the sequential GVLM computations for more than two turbines is prohibitively slow even on the fastest, high instructions per cycle/clock (IPC), high-end desktop (HEDT) CPUs currently available.

Chapter 4

Numerical Experiments

In this chapter we shall discuss the premise of the numerical study conducted with the newly expanded CODEF suite. The experiments/simulations and the code development/enhancement process evolved over three, overlapping stages. We begin with an initial verification campaign of the GVLM for a single turbine. This was followed by a field validation campaign as part of our collaboration with Sandia National Laboratories (SNL). Finally, we shall describe the "exploratory campaign" that consisted of simulations of multi-turbine wind farms, based on our findings with SNL.

4.1 Preliminary Verification

The primary goal of this phase of the numerical study was to ensure the stability of the vortex lattice code and its interface with the existing DRD-BEM module+s. The NREL 5MW Reference Wind Turbine (N5M-RWT) [18], designed for onshore as well as offshore installations, is still considered a good representation of the state-of-the-art, utility-scale, multi-megawatt commercial turbines. Initial simulations in this phase were conducted with the N5M-RWT operating in a uniform wind stream at its nominal design conditions of 11.4m/s and 12.1rpm. The simulation process involves an initial run with a fixed maximum lattice size ("shedding" times). This "*warm-up*" ensures that the "transience" of early filaments in the vortex lattice is eliminated. Subsequently, the simulation was continued to run for a longer time with the vortex lattice being allowed to grow. This ensures that the vortex lattice evolves without any artifacts from the early filaments. Figure 4.1, shows the complete vortex lattice of the N5M-RWT at its nominal, steady state conditions. We can see the regularity in the vortex lattice extend far downstream ($\sim$15D) of the turbine. This verified that the GVLM implementation was stable, and if continued for a longer time, the vortex lattice would also steadily grow without any artifacts or convergence/singularity problems.

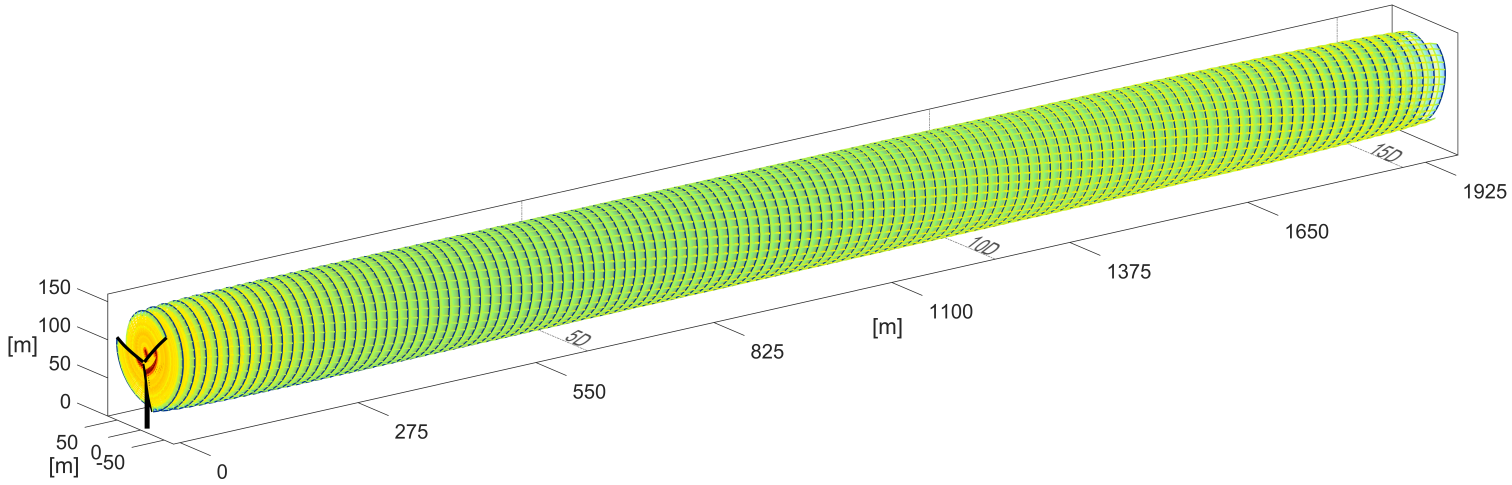

Figure 4.1: The complete, stable vortex lattice of the N5M-RWT extending more than 15D downstream of the turbine at its nominal, steady-state conditions.

Before we proceed, it must be noted that in the current implementation of the GVLM, the turbine's tower and nacelle, including the hub, have not been modeled and hence, the vortex lattice filaments flow "through" them. This leads to the the lack of drag from the tower and presence of an unrealistic "jet" in the center of the turbine wake. Preliminary efforts to include the tower and nacelle effects have been made but these would require a separate treatment in the future for their accurate representation.

The absence of any singularity errors or computational irregularities provided sound confirmation for the next phase of our simulations.

4.2 SNL-NRT Simulations

This stage of our numerical experiments involved simulations representative of the wind turbines at SNL's Scaled Wind Farm Technology (SWiFT) facility. The SWiFT facility is very unique with the vast amount of *in situ* measurements, that are publicly available to verify, validate and tune computational models. Future plans at the site involving extensive wind turbine wake and waked rotor blade measurements shall further enrich the development of computational models.

In the following subsections, we shall briefly discuss some of the saliant features of the SWiFT facility, a newly developed wind turbine blade by SNL, and the field

measurement data that we used for our simulations.

4.2.1 SWiFT Facility Overview

Located in Lubbock, TX, SNL's SWiFT facility consists of three modified Vestas V27 variable-speed, variable-pitch turbines rated at 225kW and two 60m anemometry towers. The facility has been designed to support investigations to reduce the turbine-to-turbine interactions and enhance wind farm performance. It has also been used for the development and testing of novel wind turbine rotors. The facility consists of heavily instrumented anemometry towers and wind turbines with a suite of sensors.

As a part of DOE's Atoms to Electrons (A2e) research initiative, SWiFT is the primary facility for the study of wind turbine wakes. Figure 4.2 shows the layout of the SWiFT site. With over 2 years of historical data, the atmospheric conditions are well characterised, especially at scales important for wind power. The site is located in the flat Texas Panhandle with a consistent wind from the south (average 180.5°N). The two met towers are placed 2.5 rotor diameters upwind of the wind turbines. The three turbines are placed in a right-triangular layout. Two turbines (WTGa1 and WTGb1) are placed side-by-side, three rotor diameters apart. And the third turbine (WTGa2) is placed five rotor diameters downwind of WTGa1. This configuration of the turbines enables the study of complex wake flows, and the consequential rotor loads and overall

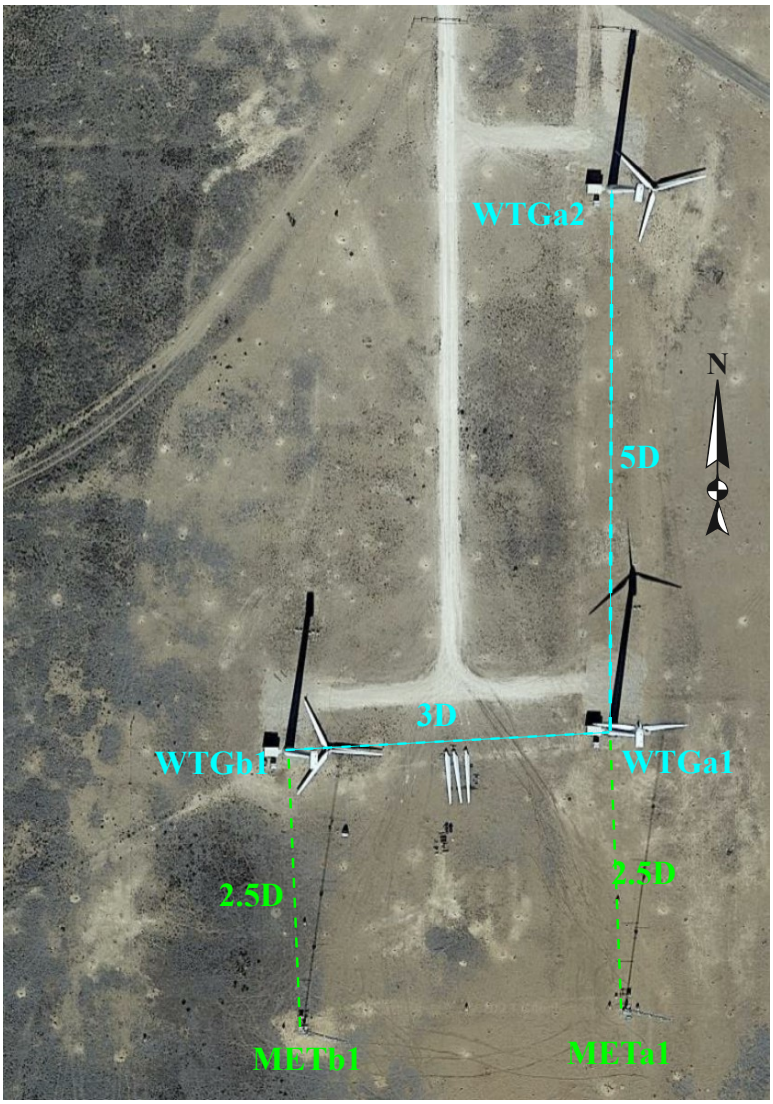

Figure 4.2: Layout of SNL's SWiFT site in Lubbock,TX.

wind farm performance. Of the numerous sensors and instrumentation on the met towers and turbines, the following are of particular interest to us:

1. cup anemometers at three different heights of the met tower,

2. 3D sonic anemometers at five different heights of the met tower,

3. yaw measurement sensor on the turbines, and

4. the DTU Spinner LiDAR located in the nacelle of turbine WTGa1.

The Vestas V27 turbine is based on design philosophies belonging to the generation of turbines represented by the N5M-RWT. We conducted our vortex wake simulations using a version of the N5M-RWT scaled down (herein referred to as the *N5M27*) to the V27 turbine at three different inflow conditions as reported in [2]. The values of the different parameters of these inflow conditions are 10minute averages of the anemometer measurements. We term these as the "steady-in-the-average" (SITA) values/cases, since the mean of the wind speed, direction, the vertical shear profile - alpha, and veer are then used as the constant-valued inputs for the duration of the CODEF simulations. These SITA cases, representative to the average anemmometry measurements, are summarized in Table4.1.

Table 4.1
Inflow details of the representative field measurements and corresponding figure in [2] used for N5M27 simulations.

Scenario (Fig. no)	**Wind Speed** [m/s]	**Alpha**	**Veer** [deg]	**Yaw Offset** [deg]
Scenario 1 (Fig. 7)	8.2	0.12	1.3°	5.9°
Scenario 2 (Fig. 9)	6.9	0.37	14.6°	-0.12°
Scenario 3 (Fig. 11)	4.8	0.15	-5.0°	10.9°

4.2.2 NRT Blade Overview

The next series of simulations involved a novel wind turbine blade developed by SNL as part of their National Rotor Testbed (NRT) project [28]. The NRT blade has been designed to be used at SWiFT with a specific focus for studying scaled wakes. It has been conceptualised to produce a wake that has the similitude to the wakes of utility scale turbines despite the difference in its size and the atmospheric boundary layer. In addition to the original "baseline" (BsLn) design of the NRT, several variants of the same blade with different stiffnesses were also simulated to study the effect on the turbine wake. The different variants were created by scaling the thicknesses of the shell and spar cap as a fraction of the original, BsLn version. The span-wise distributed blade properties obtained can be seen in the subsequent plots.

The total mass of the each variant of the NRT blade is summarised in Table4.2.

Table 4.2
Mass of the Baseline NRT blade and its different flex variants.

Blade Variant	**Mass** [kg]	**Mass % of BsLn**
BsLn	551.156	-
60% SpSh	360.594	65.42
40% SpSh	260.445	47.25
20% SpSh	156.286	28.35

The simulations for the NRT BsLn blade and its variants were conducted with the

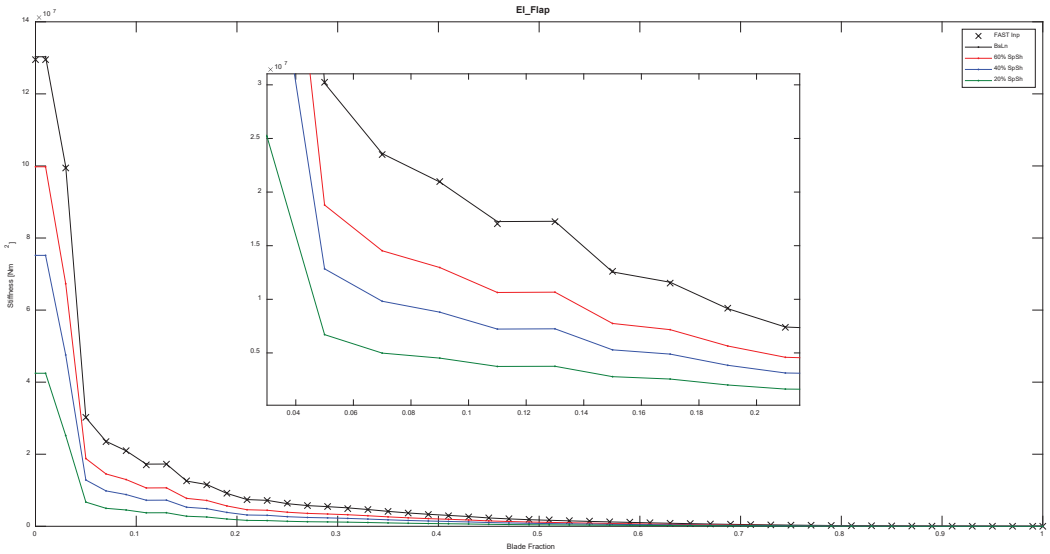

Figure 4.3: Spanwise distribution of the Flapwise Stiffness for the NRT Baseline Blade and its flex variations.

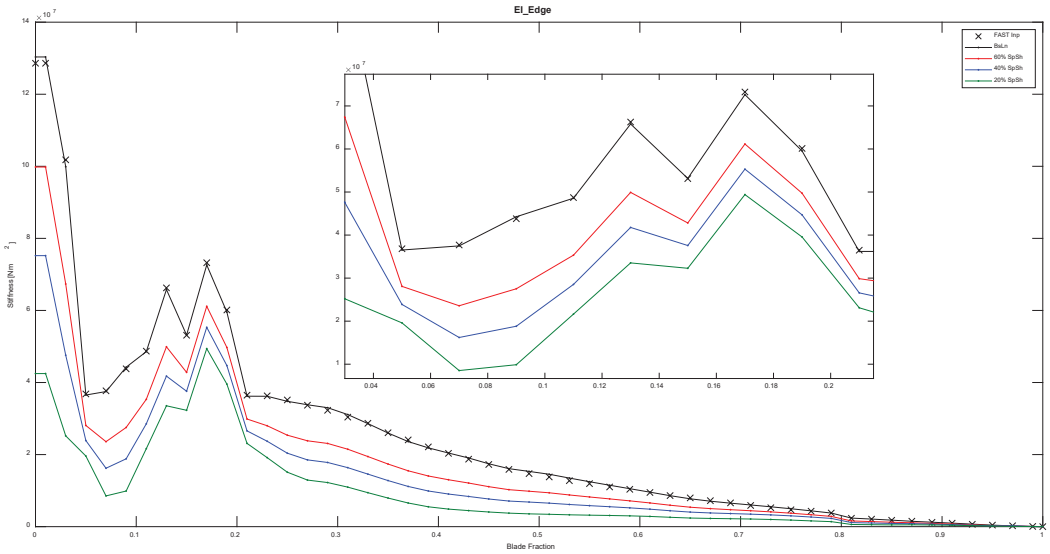

Figure 4.4: Spanwise distribution of the Edgewise Stiffness for the NRT Baseline Blade and its flex variations.

inflow conditions representative of typical day and night time conditions at SWiFT. These simulations included a yaw offset and vertical wind shear but no veer, and are

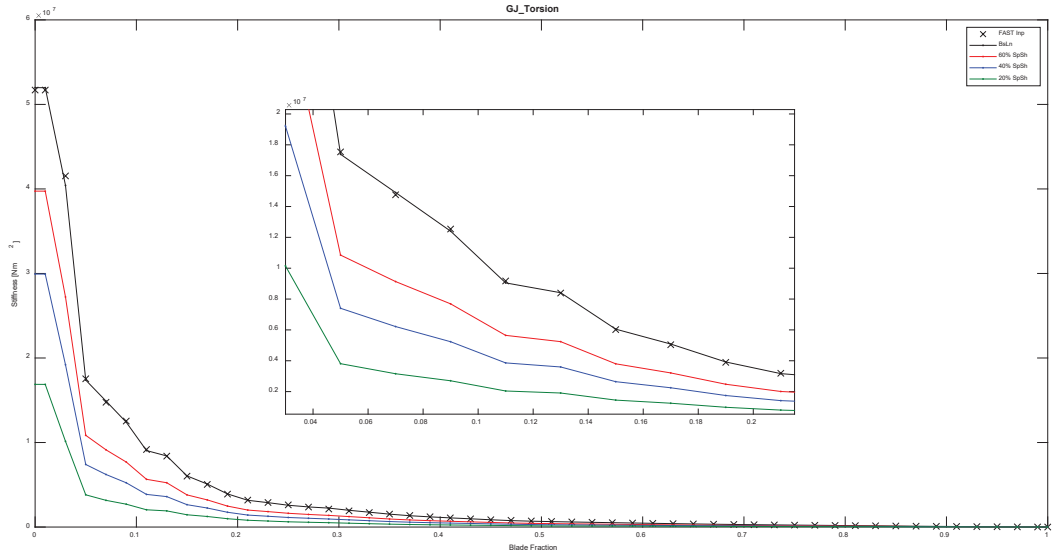

Figure 4.5: Spanwise distribution of the Torsional Stiffness for the NRT Baseline Blade and its flex variations.

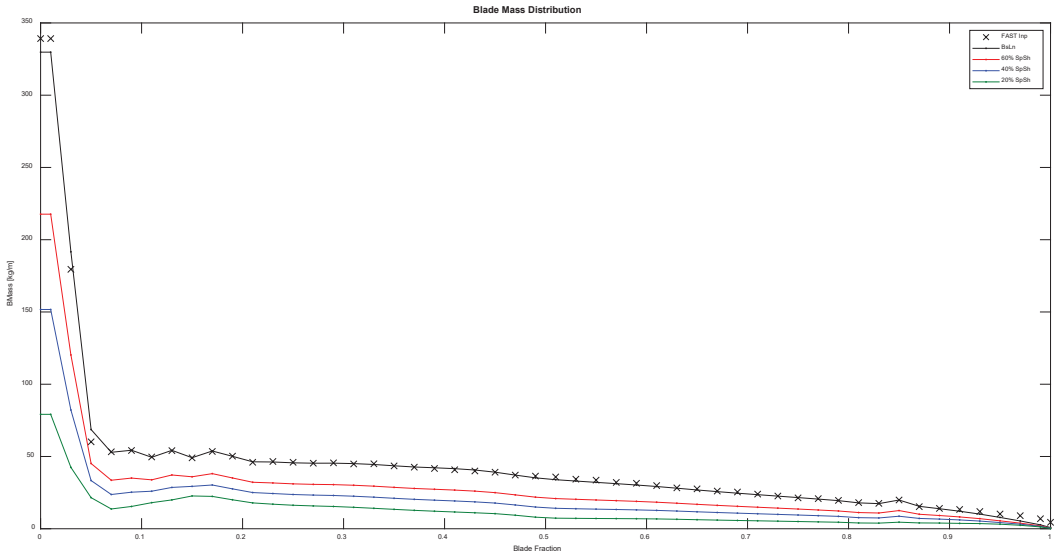

Figure 4.6: Spanwise distribution of the mass per unit length for the NRT Baseline Blade and its flex variations.

summarized in Table4.3

Table 4.3
Summary of typical day and night conditions at SWiFT facility for NRT blade simulations 10°.

Scenario	**Wind Speed** [m/s]	**Alpha**	**TSR**	**Yaw Offset** [deg]
NRTD1	6.0	0.06	9	0°
NRTD2	6.0	0.06	9	10°
NRTN1	6.0	0.30	9	0°
NRTN2	6.0	0.30	9	10°

4.2.3 Field measurements/Data availability

The numerical study also involved processing of the publicly available SWiFT field measurement data to obtain the different inputs for the simulations. The inputs consisted of (in increasing complexity) steady-state, the steady-in-the-average (SITA) values, and finally the complete, transient values of the complicated inflow parameters. An interesting note about the inputs is the optimum choice of downsampling required for reported measurement data. This downsampling needs to go hand in hand with the choice of ν_T and the appropriate turbulence indicators in the prevalent wind conditions - akin to the temporal choice of the resolved vs modelled scales in any LES.

The central position of the field measurements is certainly held by the DTU Spinner lidar mounted in the nacelle of the southeastern turbine WTGa1. Details about it can

be found in [29], [30], and [31]. The lidar is capable at measuring the downstream wake at the necessary temporal and spatial resolution for the SWiFT facility. It can scan distances upto five rotor diameters downwind. One scan consists of 984 measurement points, completed in about 2sec and it takes 2sec to refocus to a different scanning distance. [32], [33], and [34] provide the details of the lidar's alignment and calibration. The lidar measurements provide the line-of-sight speed v_{los} at each of its rosette scan points. This scattered rosette scan pattern is then interpolated to a regular grid using a smoothing surface fit to provide the v_{los} contour at that particular scanning distance. The v_{los} results and contours obtained in CODEF simulations used the same points of the regular grid obtained from the SWiFT lidar dataset.

4.3 Wind Farm Array Simulations

The ultimate goal of CODEF is to run farms consisting of several wind turbines with control strategies designed for optimizing its performance - while maintaining adequate resolution for the study of the loads on waked rotors. To this end, we conducted several experiments involving more than one turbine in several layouts operating at different inflow conditions. We began with 2-turbine simulations replicating the SWiFT layout. The inflow conditions were the representative typical day and night conditions at the SWiFT site as listed in 4.3. The twin-turbine tandem

configuration allows the comparison of the wake measurements and the aeroelastic response and loads of the downwind rotor with field measurements that will be obtained from the NRT campaign at the SWiFT site.

Continuing our experiments, we conducted simulations of wind farms consisting of four and nine turbines, in 2x2 and 3x3 farm layout, respectively. While there aren't any corresponding field measurements for a direct comparison, the goal of these experiments was to verify the implementation of the parallelisation routines, and iterate computational enhancements. The final experiment that we shall discuss is a 20-turbine, 5x4 layout wind farm. This experiment was setup to run at the limit of the currently available computational hardware.

Chapter 5

Simulation of the Wake Dynamics of the SNL-NRT Rotor and its Flexible Variations

In this chapter, we shall discuss the results and observations from the numerical campaigns. We begin with the results of the prelimiinary single, N5M-RWT wake. This will be followed by the extensive SWiFT campaign and comparisons with the lidar measurements. And finally we shall visit results of the exploratory wind farm simulations and the effect on waked rotors therein.

5.1 SNL-SWiFT Simulations

For this stage of the numerical experimentation campaign, we first worked with the N5M27 turbine - as a representation of the V27 turbines installed at the SWiFT facility. By the time we moved to this phase, the model had been expanded to include veer as an input parameter for the inflow. This enabled the comparison of the CODEF simulations to the lidar measurement cases reported in [2]. The CODEF line-of-sight velocity, v_{los} is computed at the same distance downwind as that of the lidar. This v_{los} data can be obtained with no restrictions to the grid spacing. This discretisation of the v_{los} surface only affects the smoothness of the output grid and does not effect CODEF's vortex filament computations. In this post-processing step, in addition to the v_{los} we can obtain the individual components of the wake-induced velocities with/without the superposition of the inflow wind. Thus CODEF can easily and accurately provide the velocity field anywhere in the domain being considered.

The first set of our simulation studies based on the field measurements that represented the operation conditions of the SWiFT turbines demonstrates the complex evolution of the vortex wake. We can observe the dynamic wake of the N5M27 turbine as compared to the uniform wake of the N5M-RWT seen earlier. Despite being highly mutable, the wake does not suffer from any singularities / irregularities. Figure 5.1 shows the vortex lattice wake extending 5D downstream of the turbine.

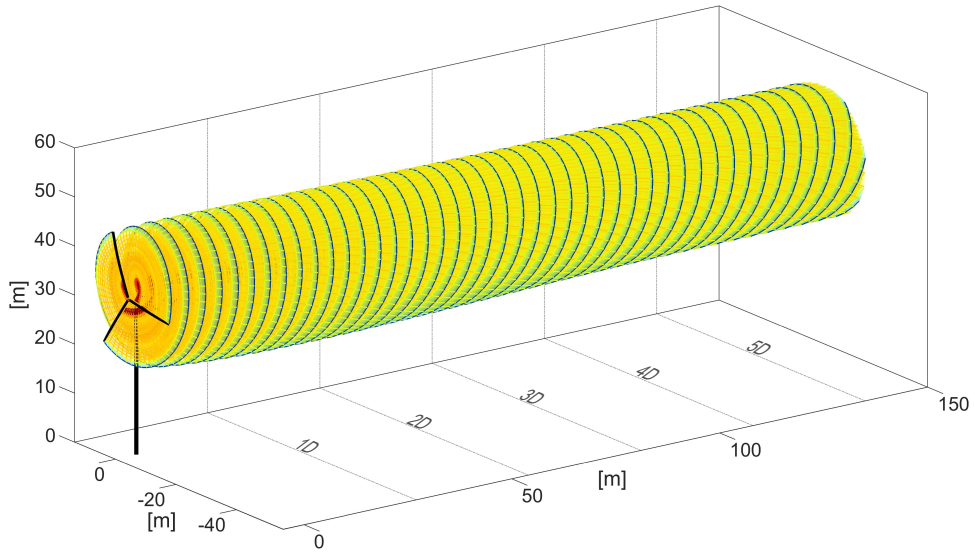

Figure 5.1: Complete vortex lattice wake for Table4.1 scenario 1

The dynamics of the wake can be better appreciated if consider cut-section at several downstream locations and view the resultant lattice structure. Figure 5.2 shows the vortex lattice at six different downstream locations.

The filaments represented by this lattice were used to obtain the *line-of-sight* velocity akin to that measured by the lidar located in the SWiFT turbine's nacelle. The v_{los} was obtained at a surface located at downstream distances mentioned in [2]. Figure 5.3 shows the lidar wake measurement reported by [2] and figure 5.4 shows the GVLM results. For comparative v_{los} figures henceforth, we recommend that readers switch between the figures being observed while keeping the same "view" and "zoom" levels when viewing this document electronically. It can be seen how well the GVLM technique captures the major features of the turbine's wake.

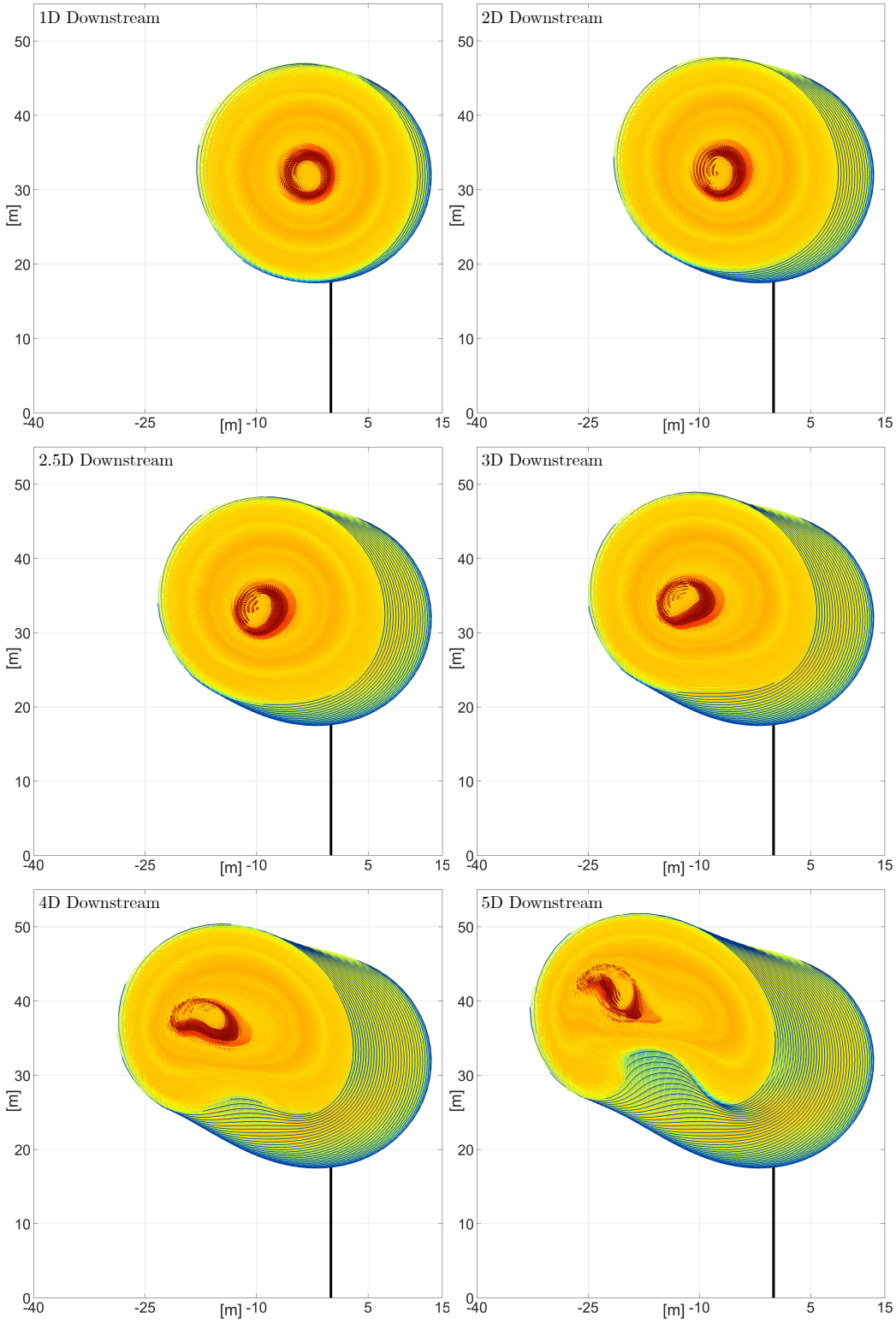

Figure 5.2: Rear view of vortex lattice wake at different distances downstream of the turbine for Table4.1 scenario 1

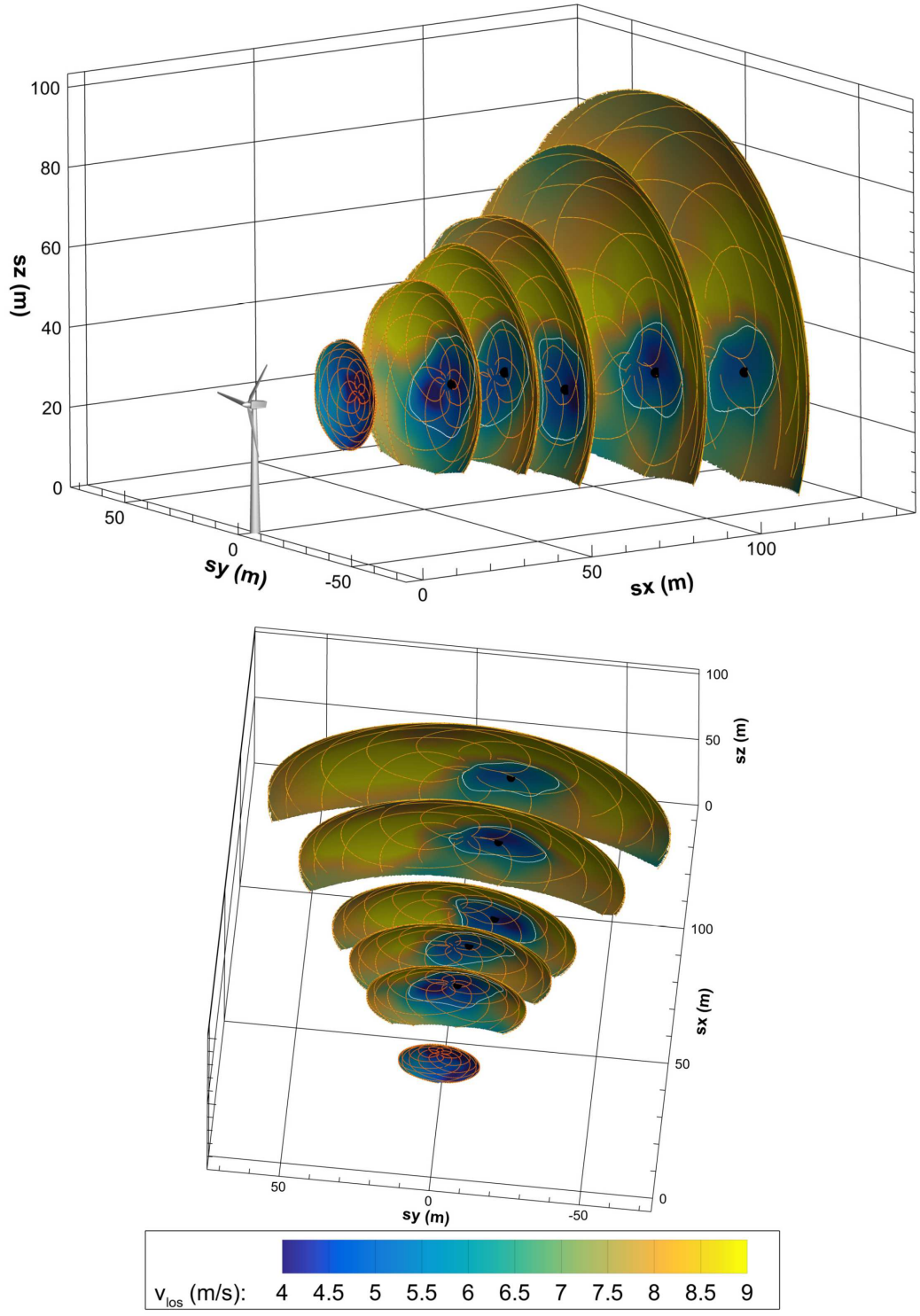

Figure 5.3: Lidar wake measurement 1-5D from [2] figure 7

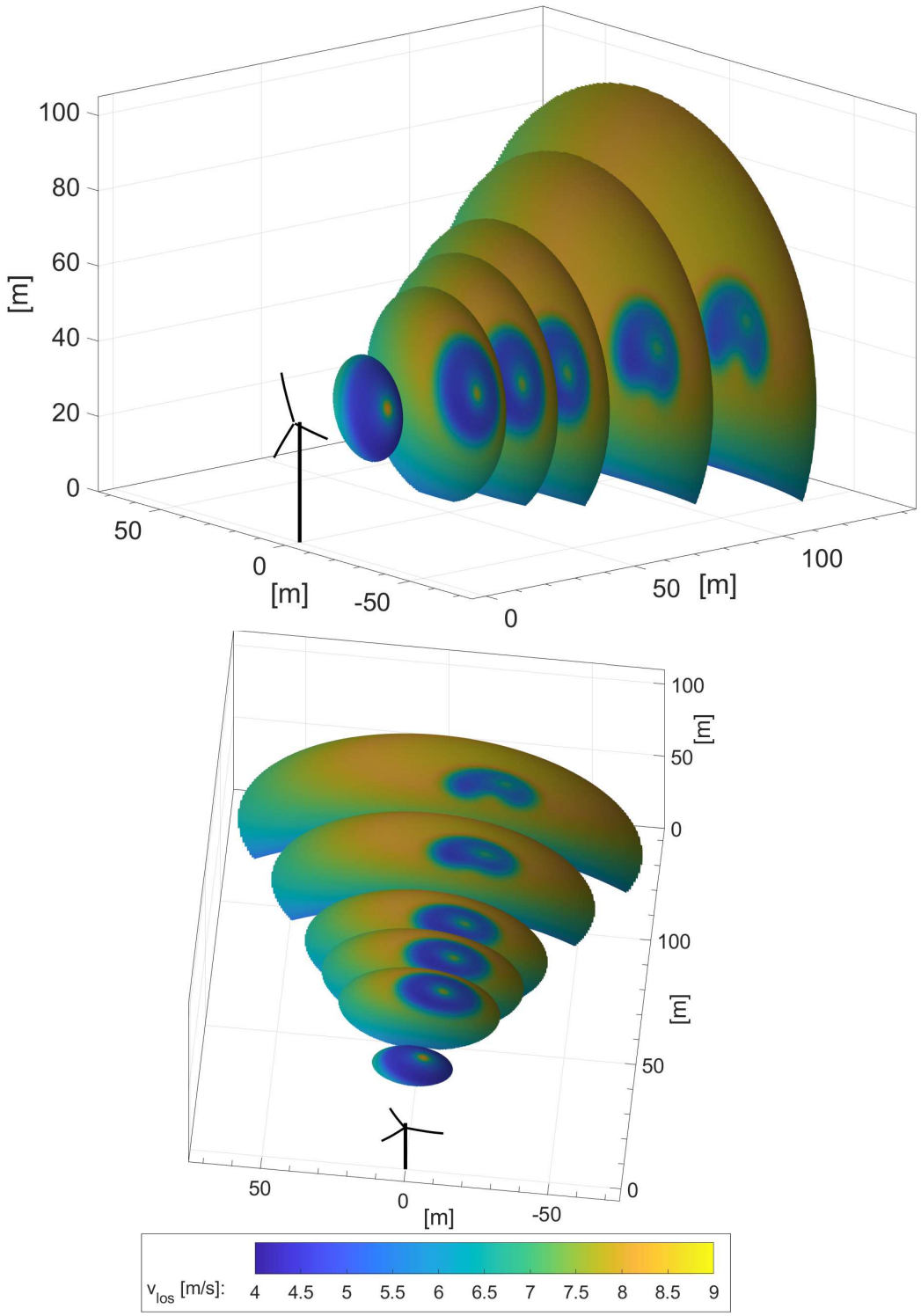

Figure 5.4: GVLM wake result 1-5D for Scenario 1

The subsequent figures show the vortex lattice wake and the v_{los} comparison with the lidar measurements for scenarios 2 and 3 from Table4.1.

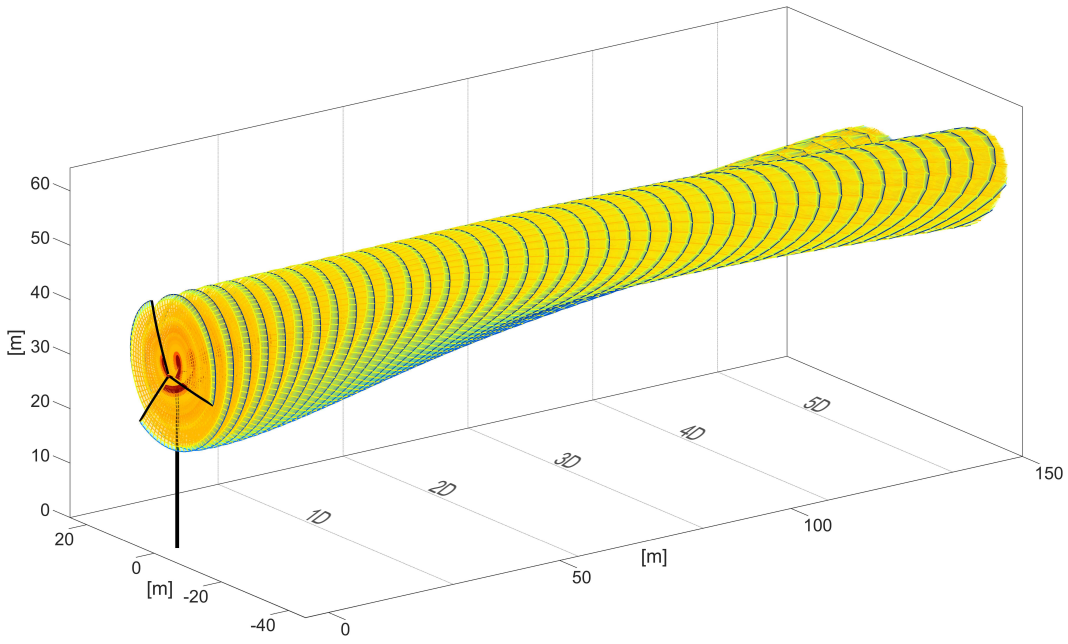

Figure 5.5: Complete vortex lattice wake for Table4.1 scenario 2

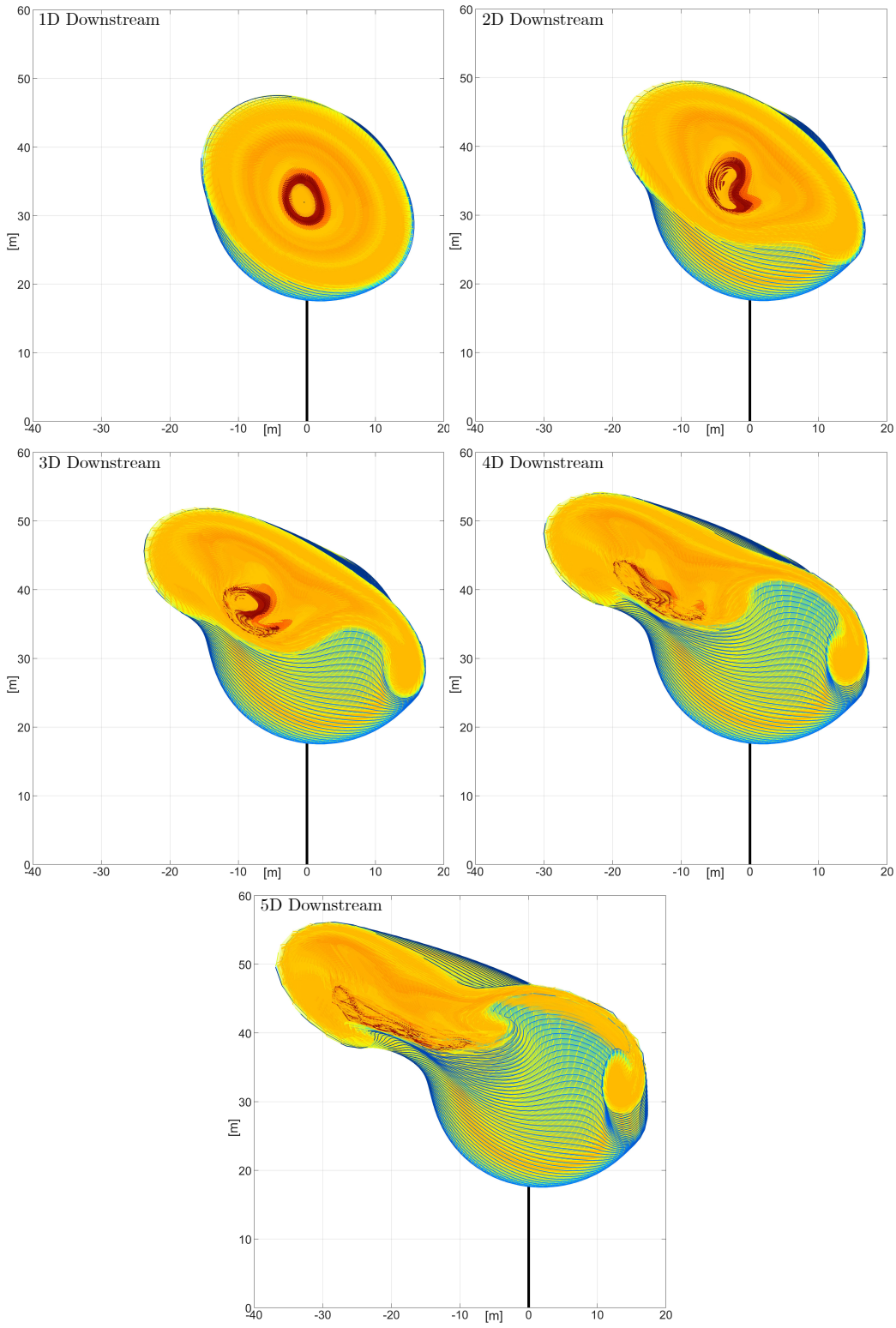

Figure 5.6: Rear view of vortex lattice wake at different distances downstream of the turbine for Table4.1 scenario 2

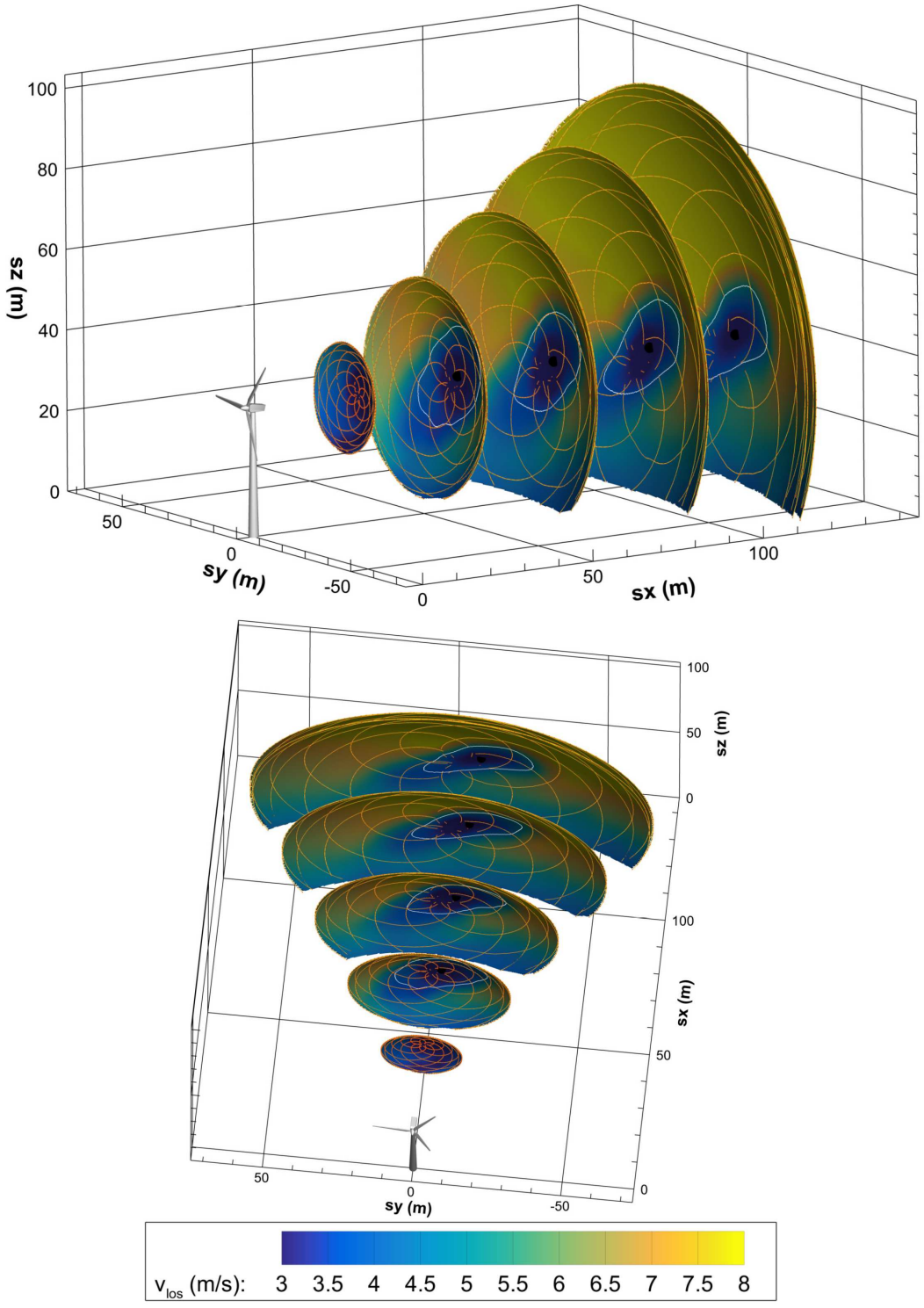

Figure 5.7: Lidar wake measurement 1-5D from [2] figure 9

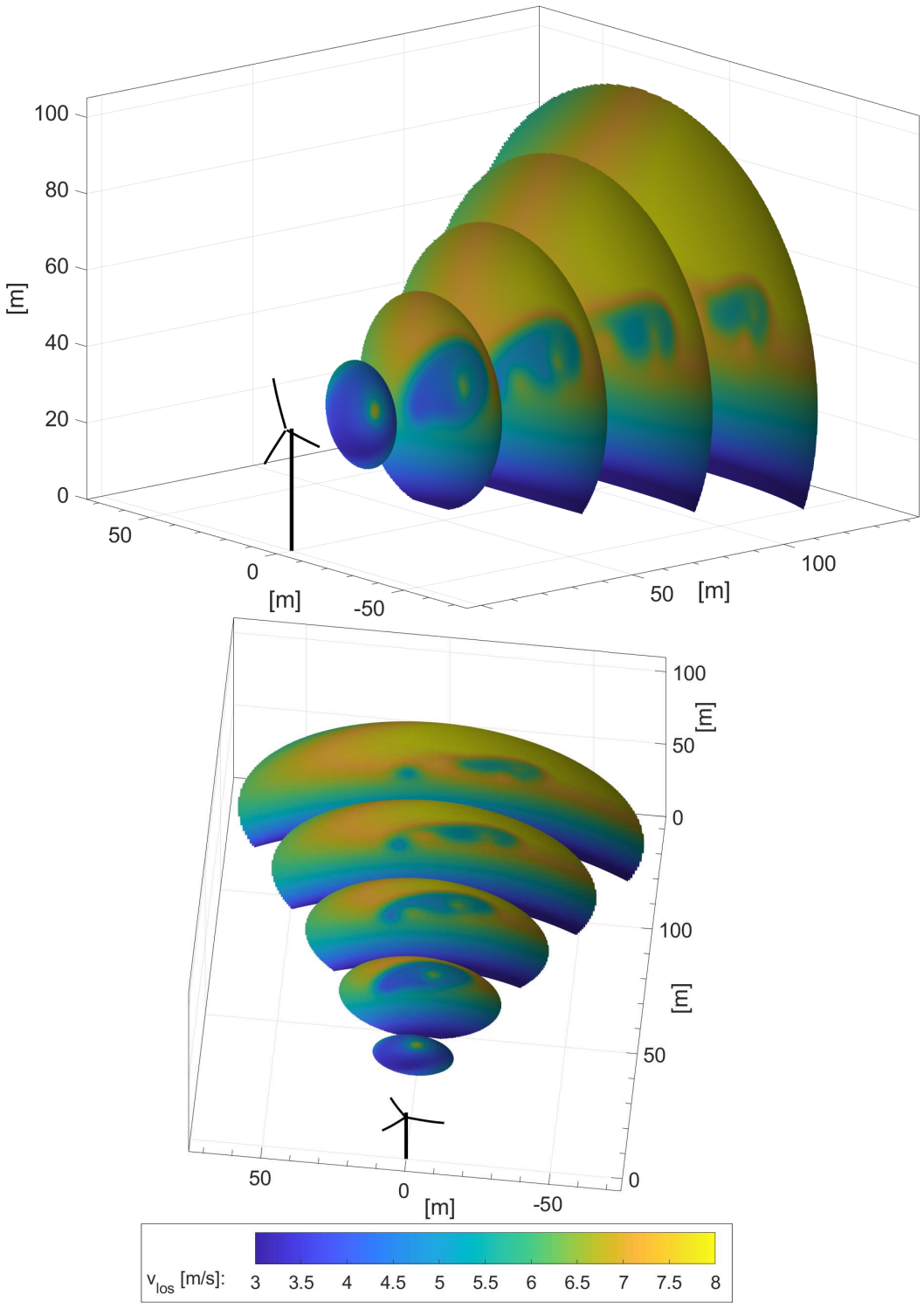

Figure 5.8: GVLM wake result 1-5D for Scenario 2

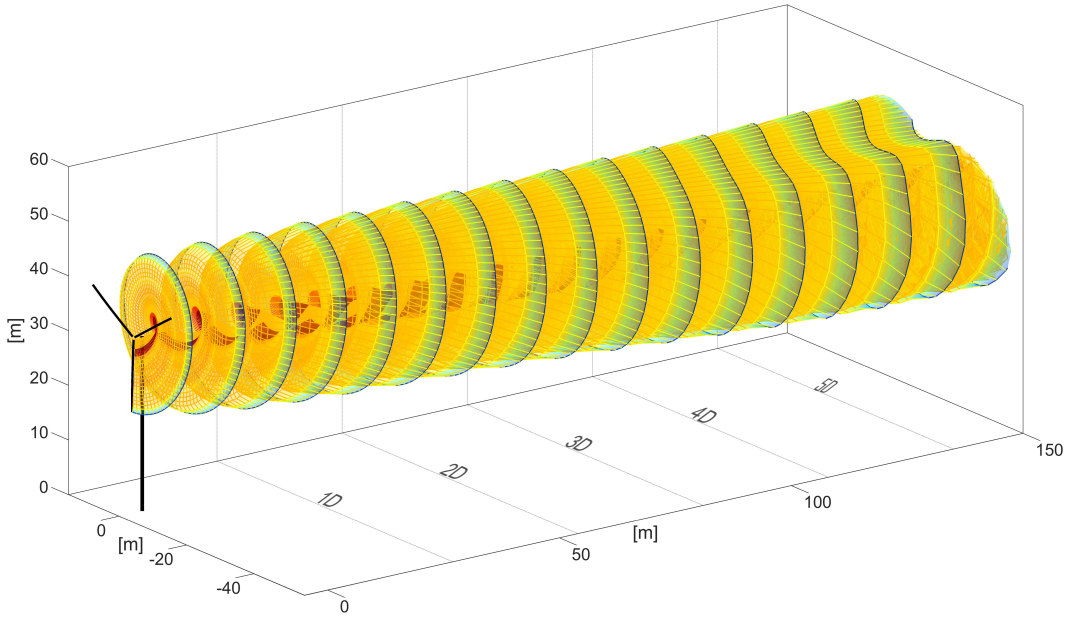

Figure 5.9: Complete vortex lattice wake for Table4.1 scenario 3

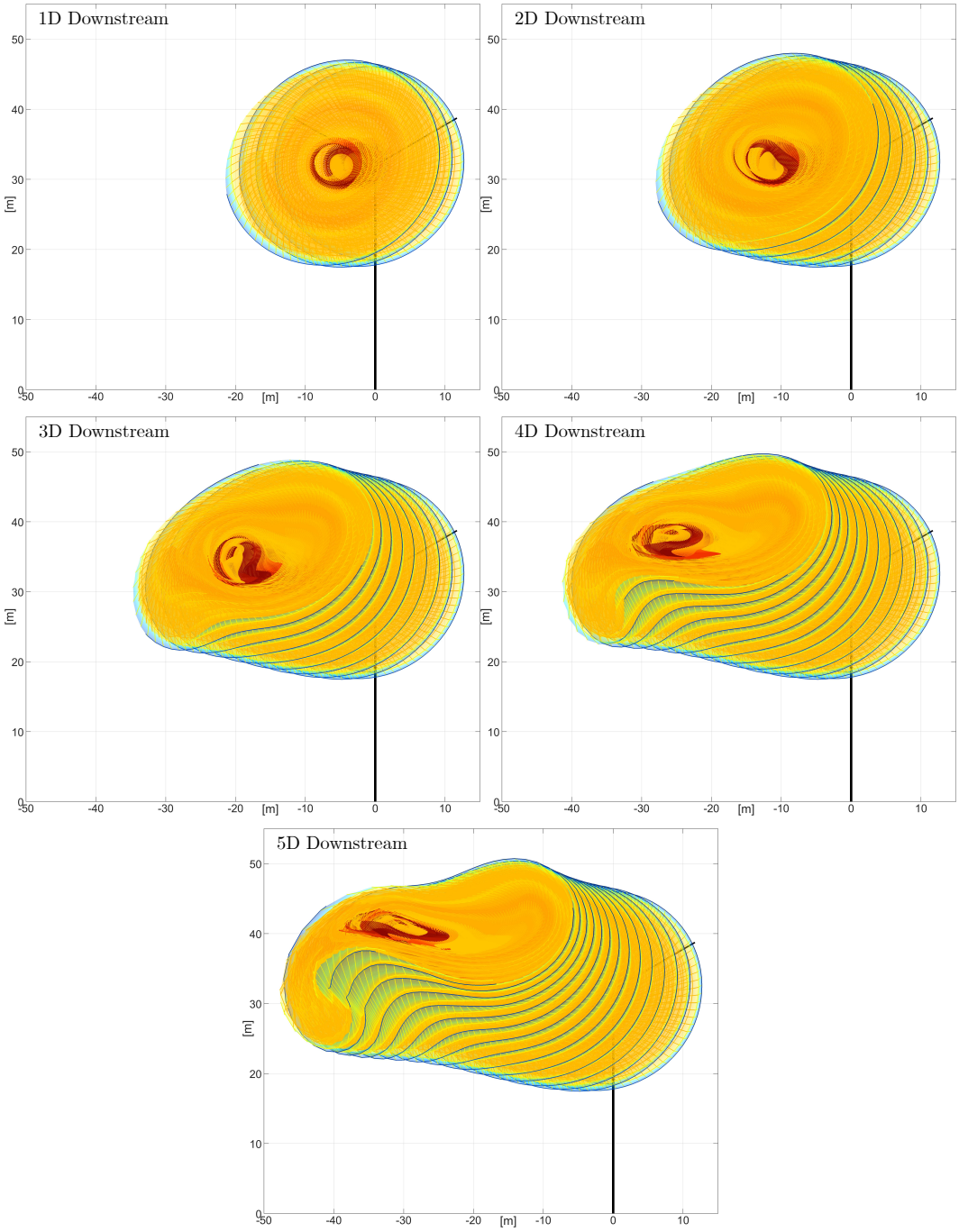

Figure 5.10: Rear view of vortex lattice wake at different distances downstream of the turbine for Table4.1 scenario 3

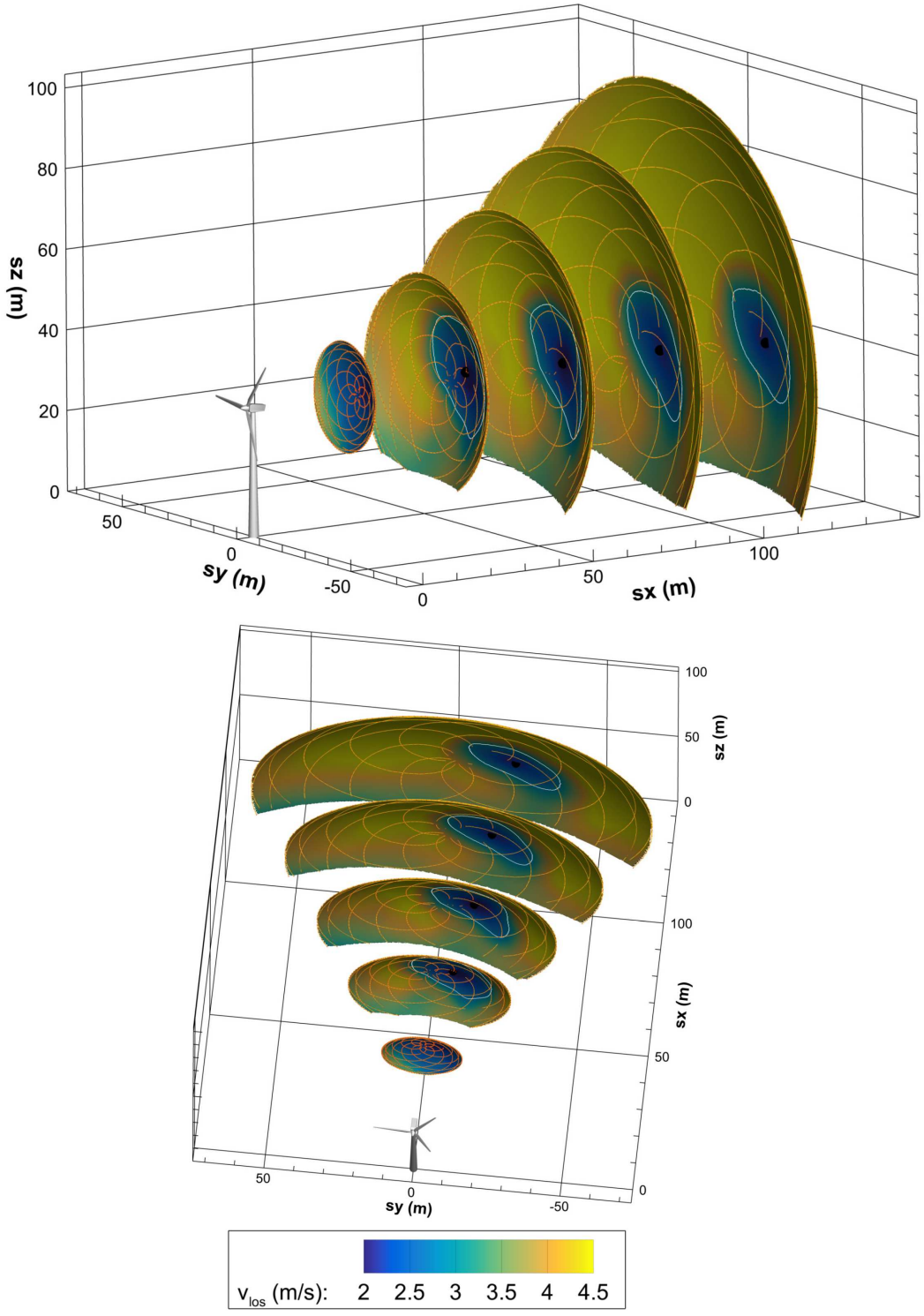

Figure 5.11: Lidar wake measurement 1-5D from [2] figure 11

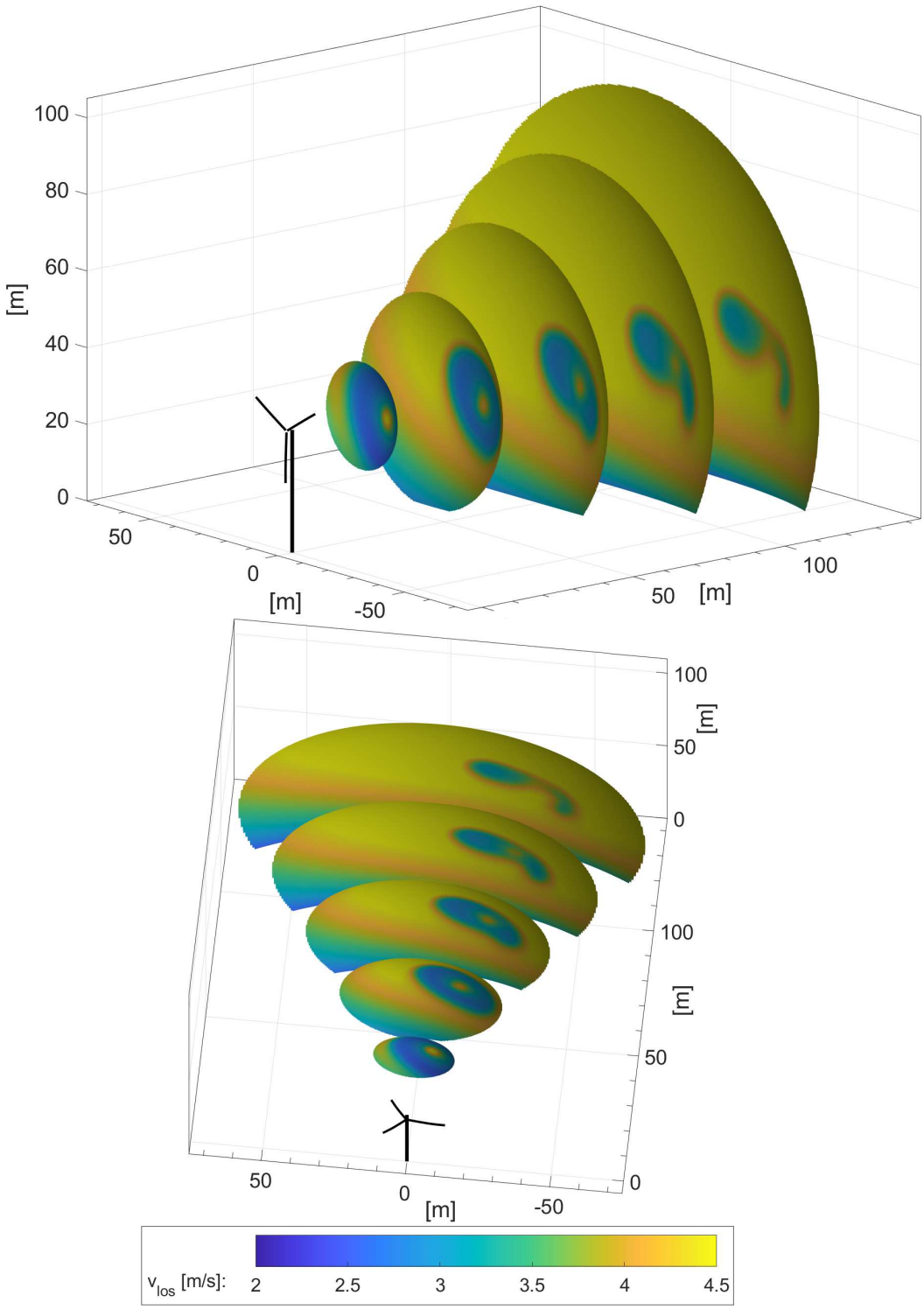

Figure 5.12: GVLM wake result 1-5D for Scenario 1

This phase of our simulations with field inflow data demonstrates the remarkable similarity with the lidar measurements - despite the differences between the V27 turbine installed on site and the N5M27 used for our simulations. This led to the next phase of our validation campaign involving SNL's novel NRT blade.

5.2 SNL-NRT Simulations

The focus of this phase of the simulations was to study the effect of varying the stiffness of the blade on its vortex wake. Since the NRT blades will be replacing the V27 rotor, GVLM simulations were run with the NRT blade and its different flex variations, subjected to typical day and night time conditions, both with and without a yaw offset. Continuing our observations as before, we shall see plots of the vortex lattice wake of the different NRT blades. Since we can obtain the induced velocities resolved in any of its components, we shall observe the component of the wake velocity along the freestream wind direction. This is helpful in understanding the wind "faced" by a downwind/waked rotor and hence is extremely useful for the study of the aeroelastic behavior of waked rotors. A deeper understanding of the rotor's behavior has both short- and long-term benefits. Accurate simulations help in the development of control strategies aimed at optimizing the performance of the entire farm, not just a single turbine. It is also important to understand the fatigue loads on the turbine blades for their longevity, and safe operation of the entire system

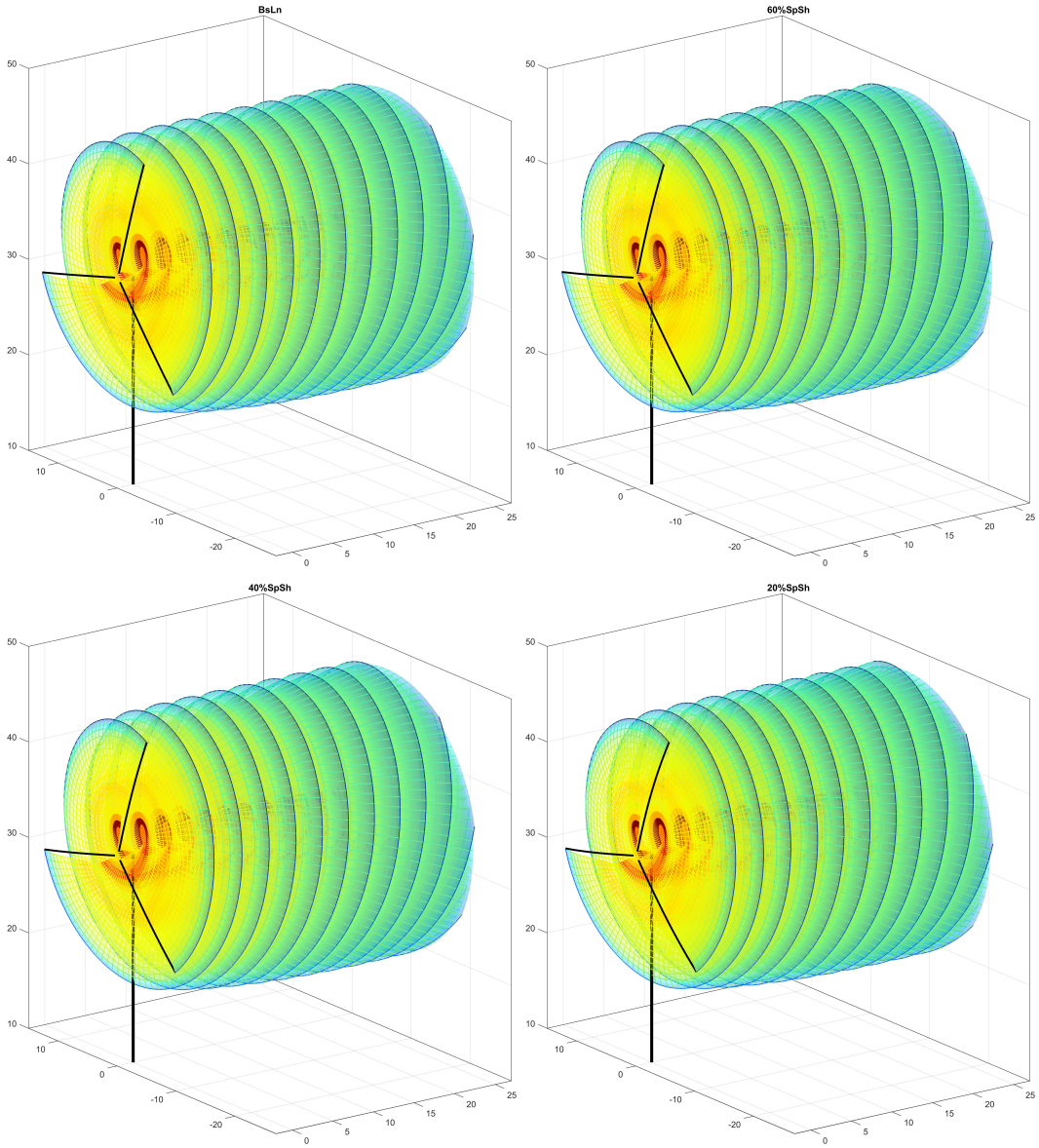

Figure 5.13: Close-up view of the vortex lattice wake of the NRT blade and its flex variations for the NRTN2 scenario. (All axes in [m]).

throughout its life-time. We begin by observing the wakes of the NRT blade and its flex variations.

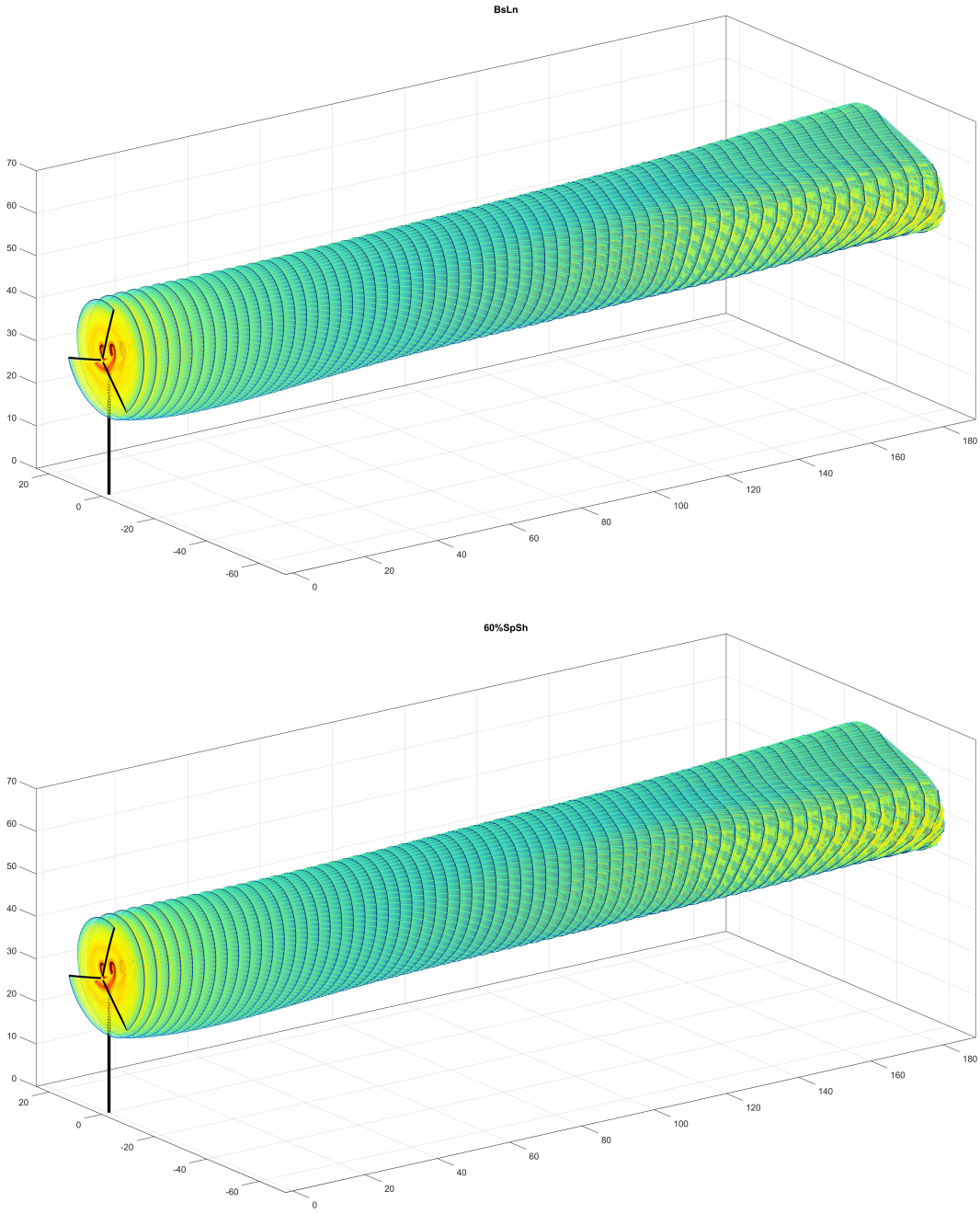

Figure 5.14: Perspective view of the vortex lattice wake of the NRT blade BsLn (top) and the 60SpSh(bottom) flex variation for the NRTN2 scenario. (All axes in [m]).

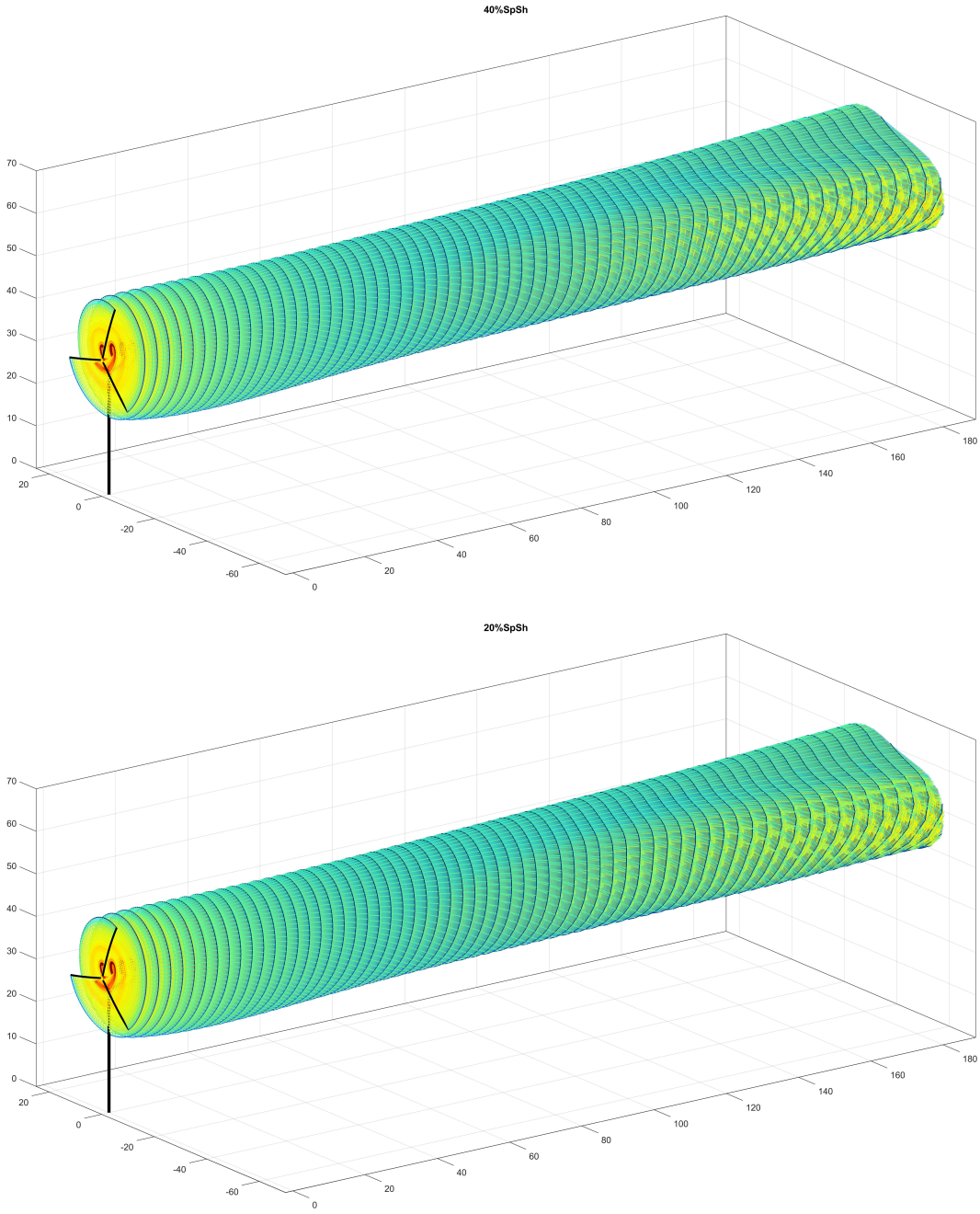

Figure 5.15: Perspective view of the vortex lattice wake of the NRT blade 40SpSh (top) and 20SpSh(bottom) flex variation for the NRTN2 scenario. (All axes in [m]).

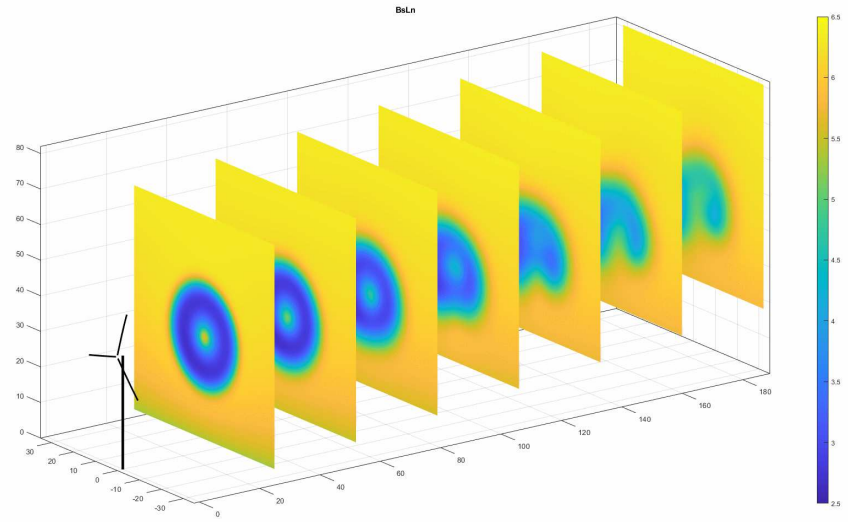

Figure 5.16: Perspective view of the streamwise velocity at cut-planes located every 1D downstream for the NRTD1 scenario. (All axes in [m]).

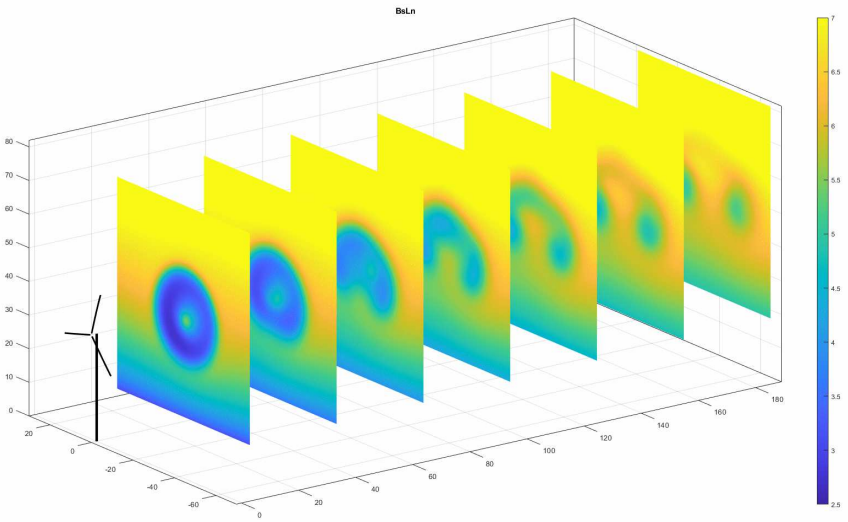

Figure 5.17: Perspective view of the streamwise velocity at cut-planes located every 1D downstream for the NRTN2 scenario. (All axes in [m]).

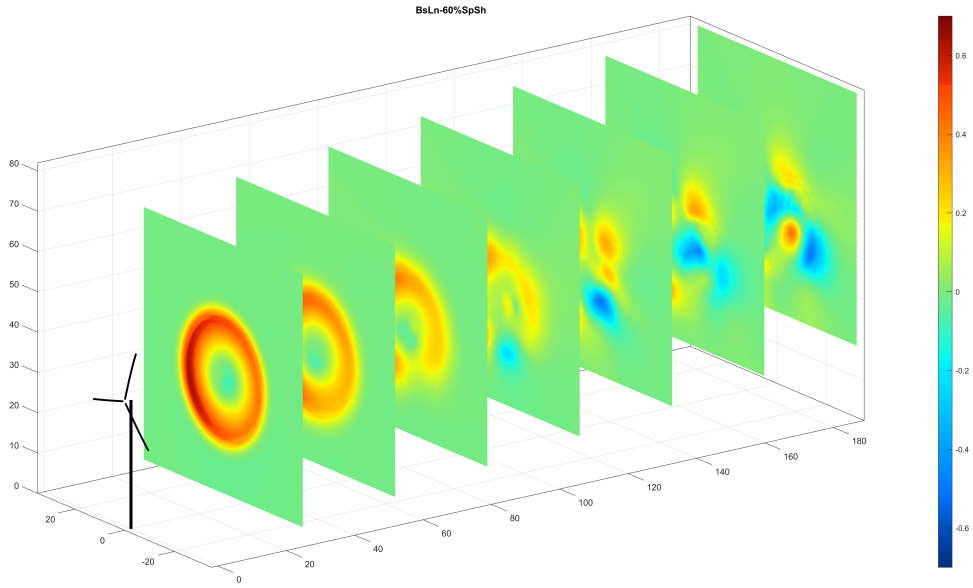

Figure 5.18: Perspective view of the streamwise wake velocity difference between the BsLn and 60SpSh variant at cut-planes located every 1D downstream for the NRTD1 scenario. (All axes in [m]).

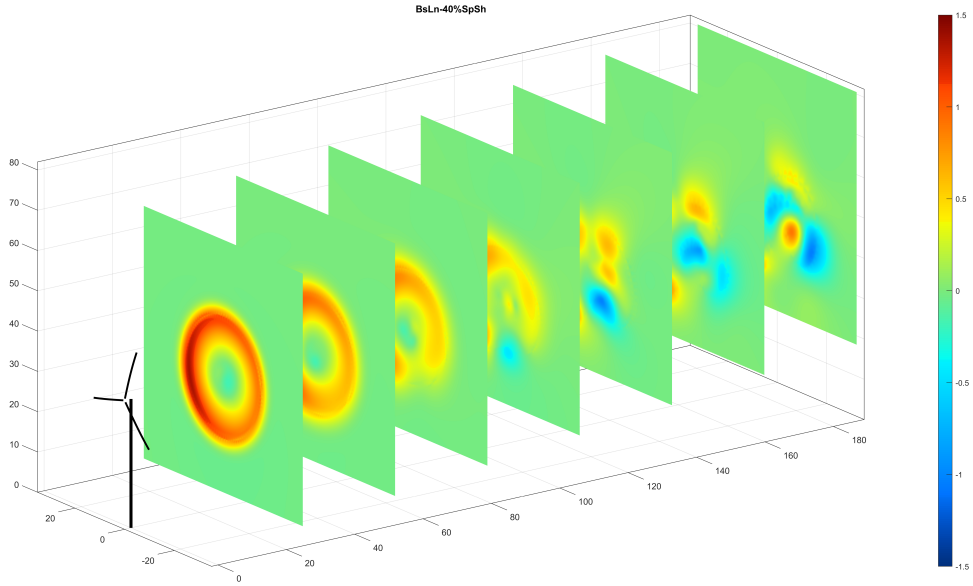

Figure 5.19: Perspective view of the streamwise wake velocity difference between the BsLn and 40SpSh variant at cut-planes located every 1D downstream for the NRTD1 scenario. (All axes in [m]).

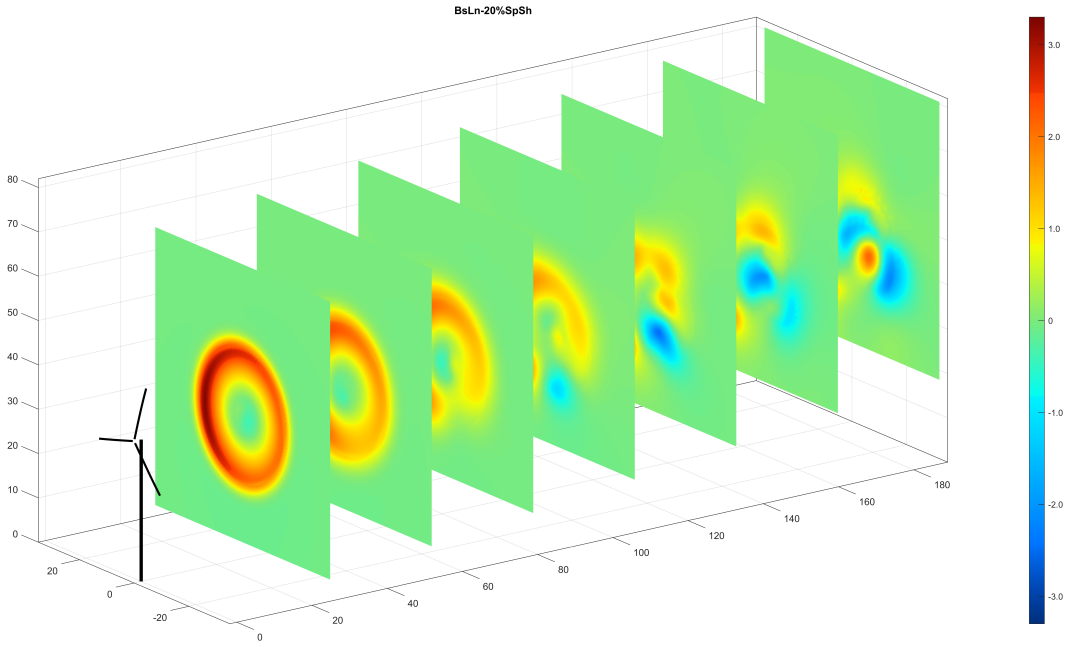

Figure 5.20: Perspective view of the streamwise wake velocity difference between the BsLn and 20SpSh variant at cut-planes located every 1D downstream for the NRTD1 scenario. (All axes in [m]).

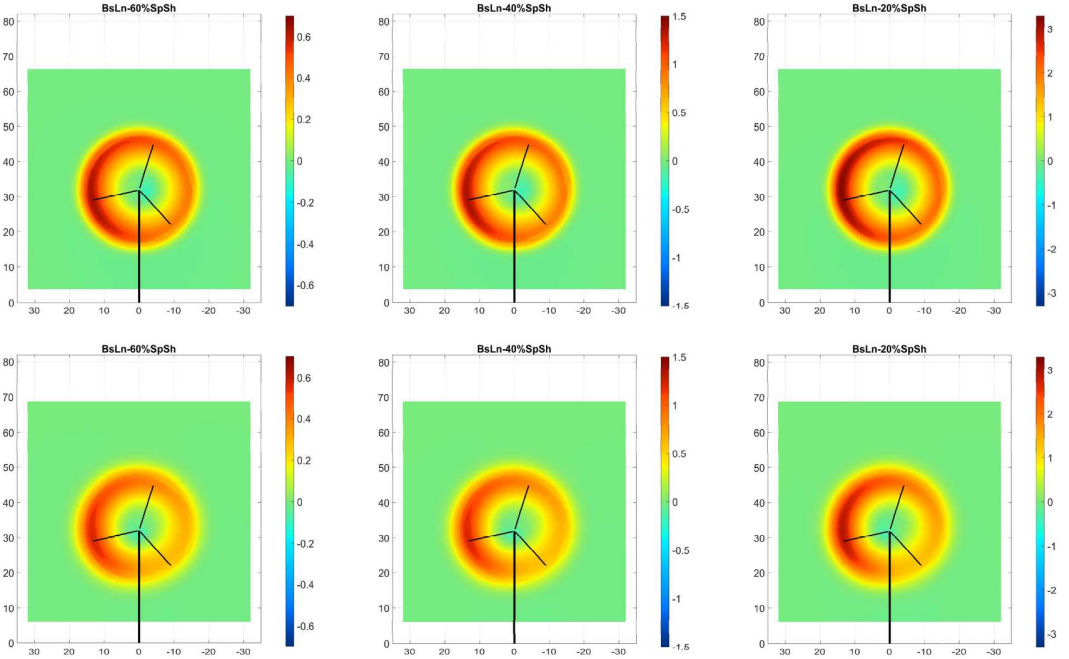

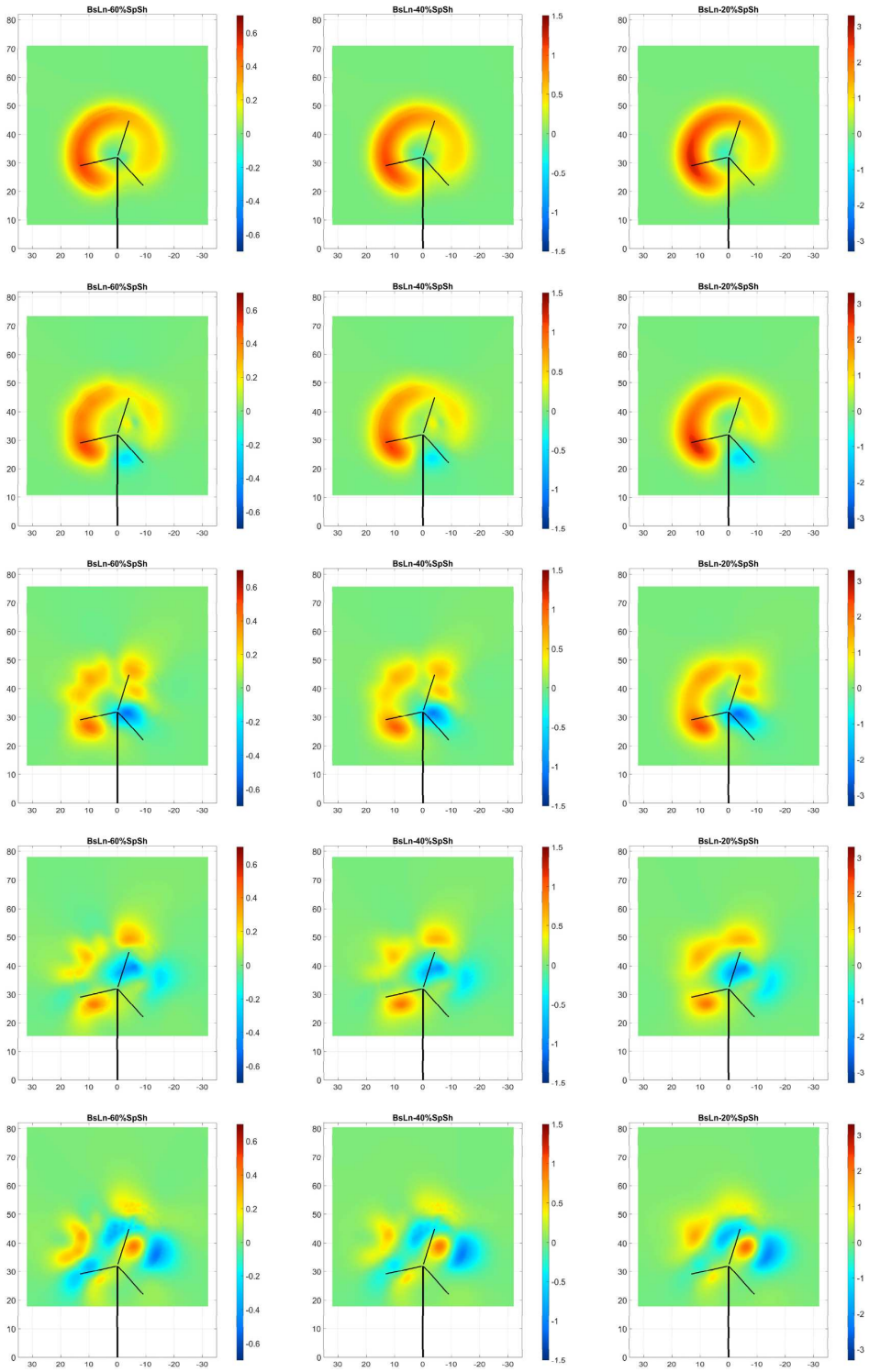

Figure 5.21: Streamwise wake velocity difference between the BsLn blade and its flex variants at cut-planes located every 1D downstream represented in each row for the NRTD1 scenario. (All axes in [m]).

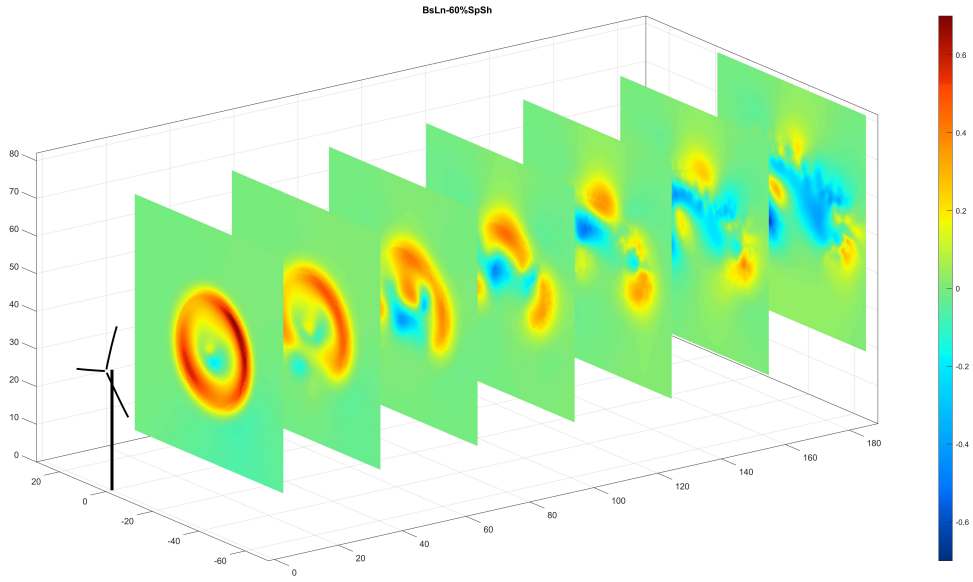

Figure 5.22: Perspective view of the streamwise wake velocity difference between the BsLn and 60SpSh variant at cut-planes located every 1D downstream for the NRTN2 scenario. (All axes in [m]).

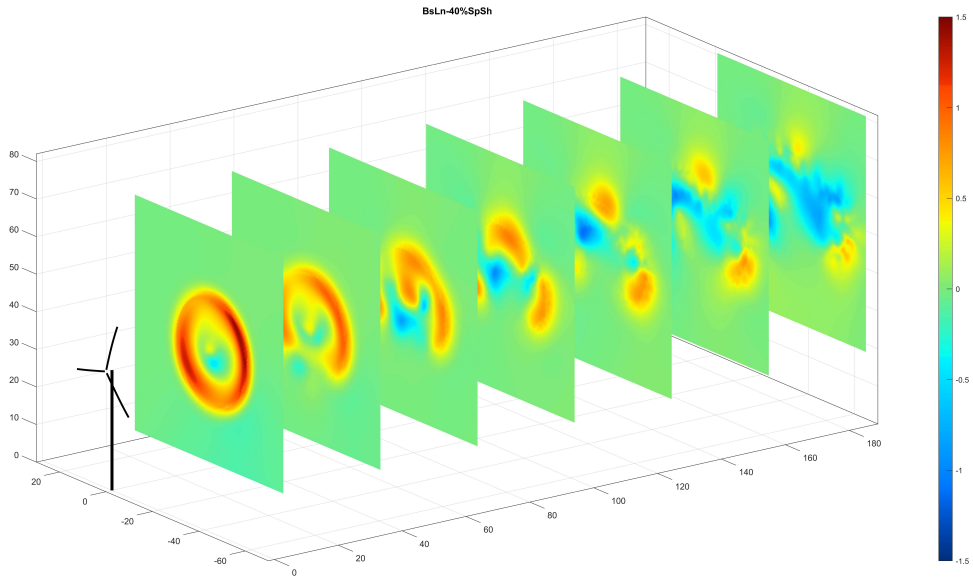

Figure 5.23: Perspective view of the streamwise wake velocity difference between the BsLn and 40SpSh variant at cut-planes located every 1D downstream for the NRTN2 scenario. (All axes in [m]).

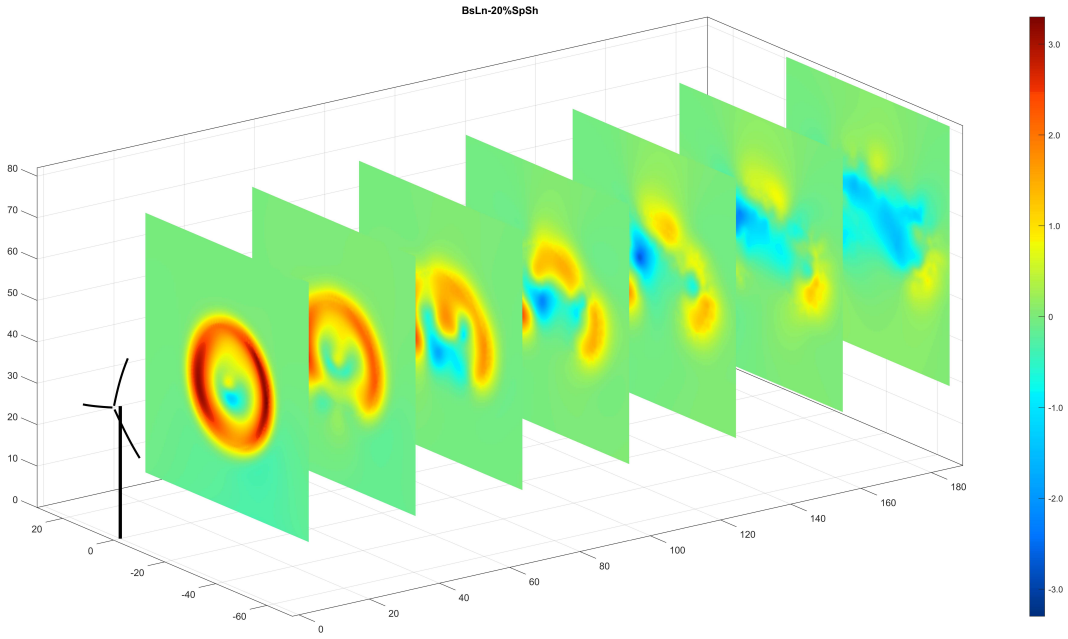

Figure 5.24: Perspective view of the streamwise wake velocity difference between the BsLn and 20SpSh variant at cut-planes located every 1D downstream for the NRTN2 scenario. (All axes in [m]).

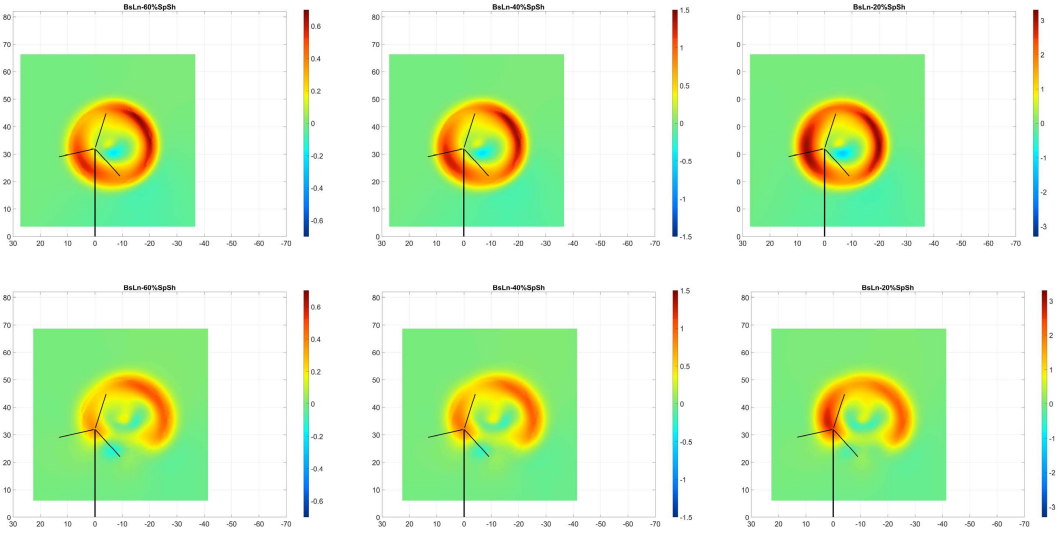

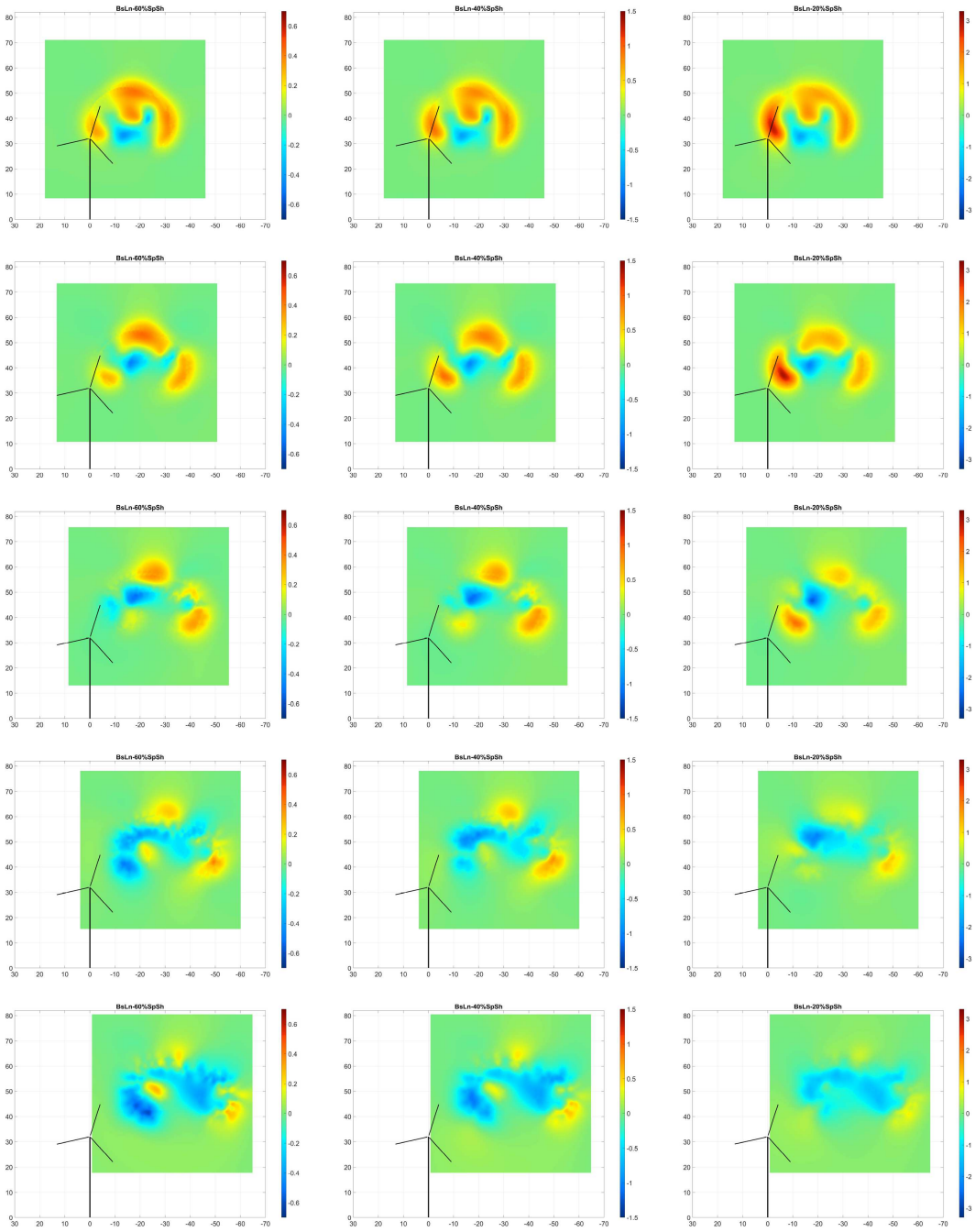

Figure 5.25: Streamwise wake velocity difference between the BsLn blade and its flex variants at cut-planes located every 1D downstream represented in each row for the NRTN2 scenario. (All axes in [m]).

5.3 SNL-NRT with Anemometry Data

The SITA cases demonstrate remarkable qualitative similarities with the reported lidar measurements. However, being average values, they do not capture the complexities of the various scales of fluctuations in real-world inflow. The fluctuations in the aerodynamic loads for the SITA cases are primarily because of the cyclical motion of the blades as they traverse through the variable flow field. These variations in the flow field are a consequence of the wind shear, veer, rotor tilt and yaw. With the inclusion of the fluctuations of the wind, instead of SITA inputs, the differences in the response of the BsLn and the other flex variations are bound to increase. The flex variants of the NRT blade have different natural frequencies. The inclusion of the temporal variations in the wind will consequently lead to different aeroelastic responses of the rotors. This in turn would lead to significant differences in the vortex-shedding process, ultimately altering the vortex wake and evolution for each blade.

Since CODEF easily accepts these variations in the input, we incorporated the temporally varying anemometry information (AmDat) to our model inflow. To obtain these inflow inputs, we scaled the anemometer measurement sample to the prescribed typical day and night time conditions at SWiFT. The variations were included for all the input parameters - wind speed, direction, vertical shear exponent

(alpha), and veer.

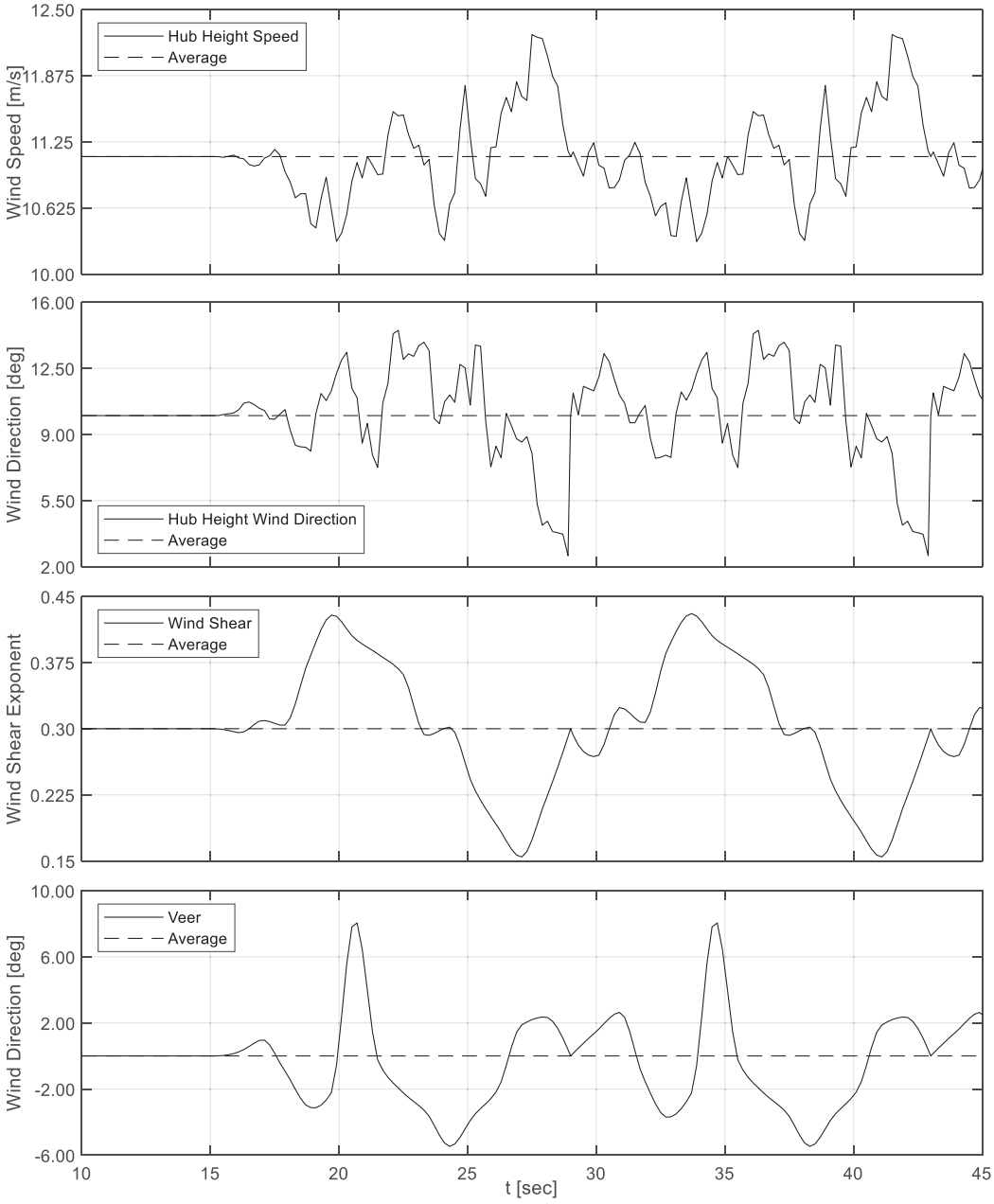

Figure 5.26: Anemometry sample with fluctuations in yaw offset, shear exponent and veer scaled to NRT nominal wind speed.

We can see the differences in the evolution of the vortex lattice wake and the velocity patterns as a consequence of the temporally varying inflow in figures 5.27 and 5.28.

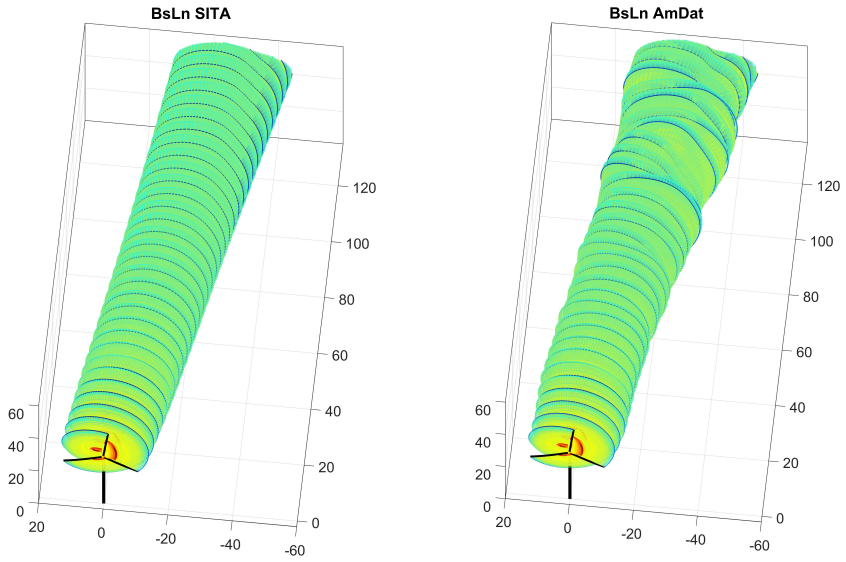

Figure 5.27: Comparison of vortex lattice wake for the SITA and AmDat inflow inputs. (All axes in [m]).

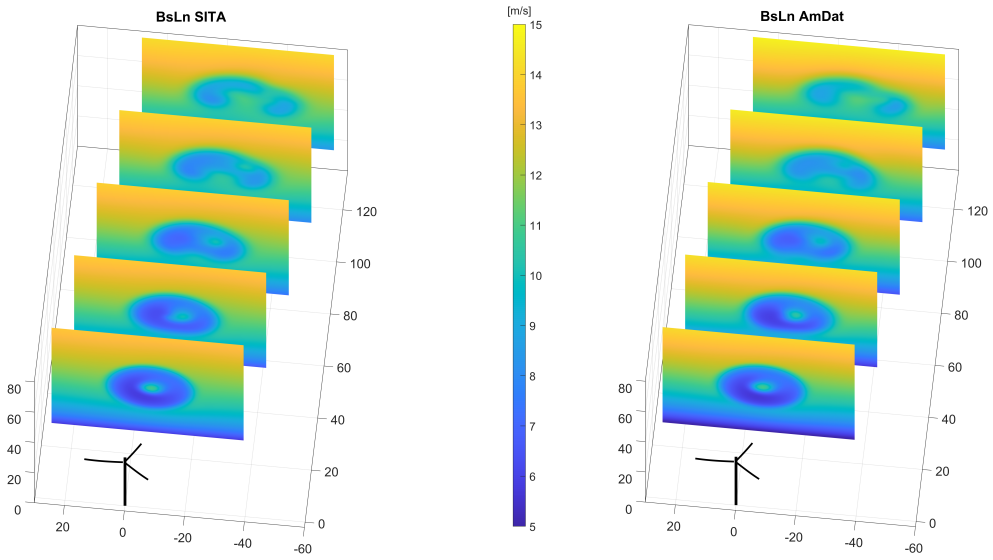

Figure 5.28: Comparison of velocity patterns for the SITA and AmDat inflow inputs. (All axes in [m]).

The results discussed hitherto demonstrate the ability of the GVLM to respond to different kinds of blades and temporally varying inflow inputs. The variations in the vortex lattice and the downstream wake velocity led to the next stage of simulations involving multi-turbine wind farms.

Chapter 6

Simulation of the Wake Interaction of SNL-NRT in Twin-Turbine Tandem Configuration

6.1 Aeroelastic Response of Twin-turbine Farm Rotors

For our first set of farm simulations we used the NRT BsLn blade in a twin-turbine, tandem configuration (similar to the WTGa1 and WTGa2 located at the SWiFT facility). These simulations are designed for the analyses of the turbine-to-turbine

interaction and the aeroelastic response of waked rotors.

The twin-turbine simulations were conducted for the NRT BsLn blade and its flex variations with SITA inflow inputs. These cases were run for a period of time sufficient for the vortex lattice wakes of both the turbines to grow, overlap and interact with one another. Figures 6.1 and 6.2 show the evolution of the vortex lattice wakes for NRT BsLn twin-turbine farm operating in the NRTN1 scenario.

As seen in these figures, the twin-wakes evolve for a certain amount of time and then reach a statistically stable regime (since we have SITA inflow). This situation can be better appreciated by observing the aeroelastic response of two turbine rotors. Figures 6.3 and 6.4 present the time evolution of the blade tip deflection and hub torque of the upwind (T1) and downwind (T2) turbine. We see that after an initial transitional period, where the wakes grow, overlap, and interact, the two signals exhibit a stable oscillatory regime. Fundamental statistical values (Mean, Minimum, Maximum, Max Amplitude) of several turbine parameters were obtained for the interval of this regime. The parameters are namely the blade-tip deflection, blade-root flapwise bending moment, and the rotors' torque, thrust and power. These parameters are summarized for the BsLn blade and its flex variations for all the conditions from 4.3 in subsequent tables. We can also observe the variation of these values with the change in the blade mass as a consequence of the reduction in the stiffnesses of the different NRT flex variants.

Although useful for basic characterisations, simplified statistical representations insuffciently capture such the rich, dynamic evolution and interaction of the vortex wakes. This can lead to inaccurate predictions of the turbine loads and power production. When wakes of multiple turbines interact with each other, with varying levels of overlap, simplified methods further exacerbate these predictions. Hence, the choice of the characterisation is extremely important for the development of collective-farm control strategies.

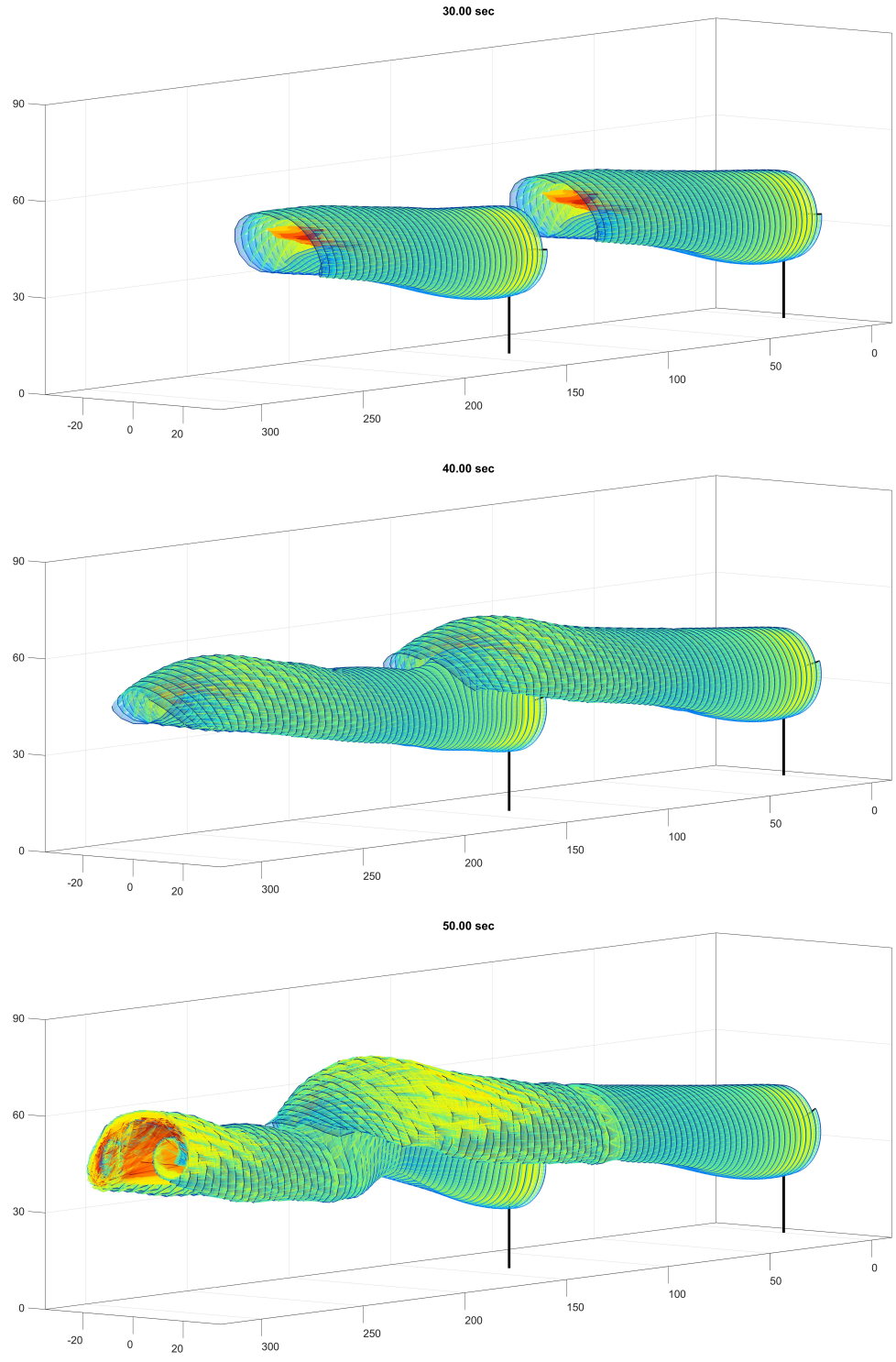

Figure 6.1: Vortex wake evolution of the NRT BsLn twin-turbine, tandem configuration from 30-50sec for the NRTN1 scenario. (All axes in [m]).

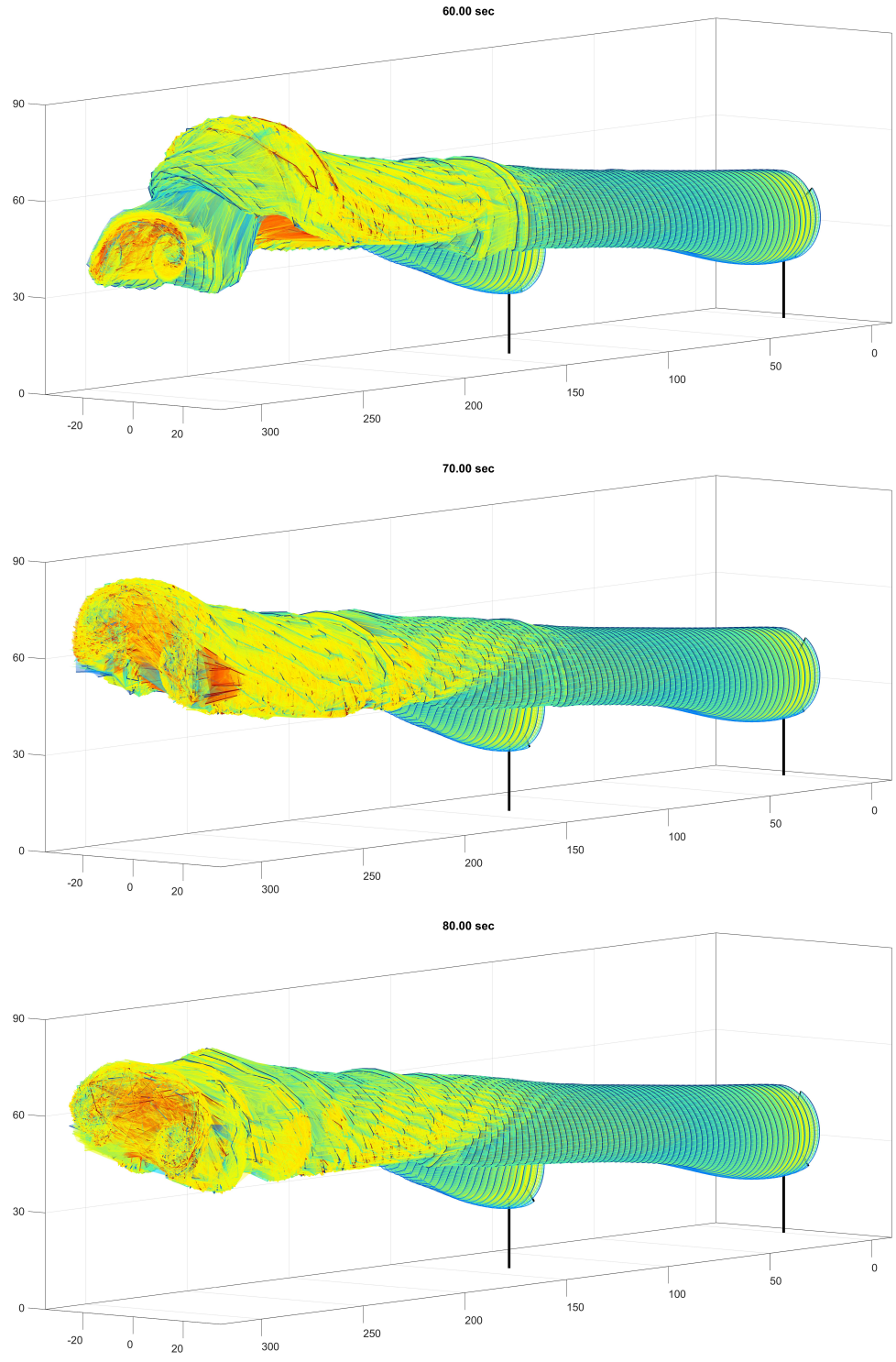

Figure 6.2: Vortex wake evolution of the NRT BsLn twin-turbine, tandem configuration from 60-80sec for the NRTN1 scenario. (All axes in [m]).

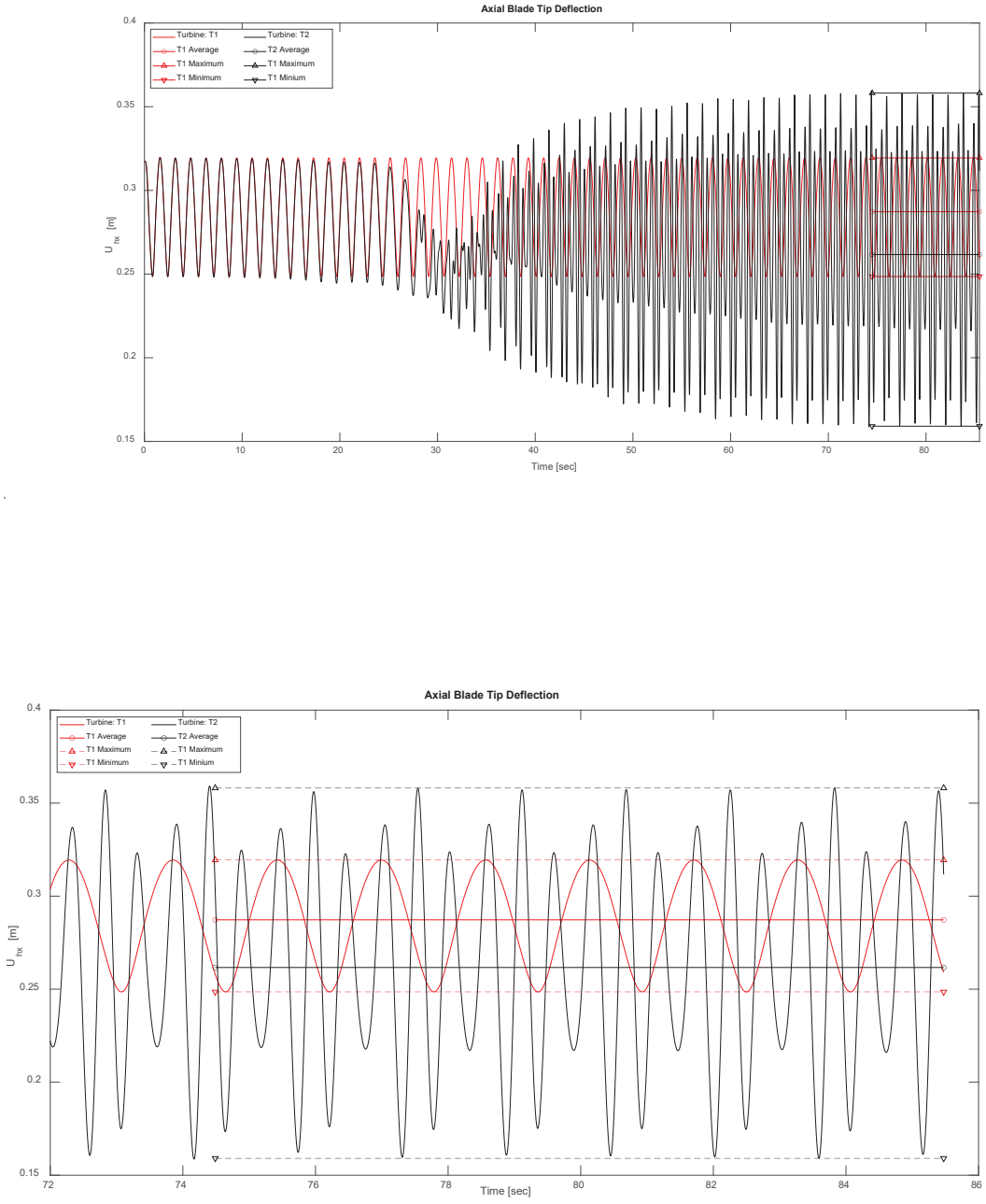

Figure 6.3: Time evolution of the blade tip deflection of the NRT BsLn twin-turbine, tandem configuration for the NRTN1 scenario. Top: Full signal, Bottom: Close-up of the stable oscillatory regime.

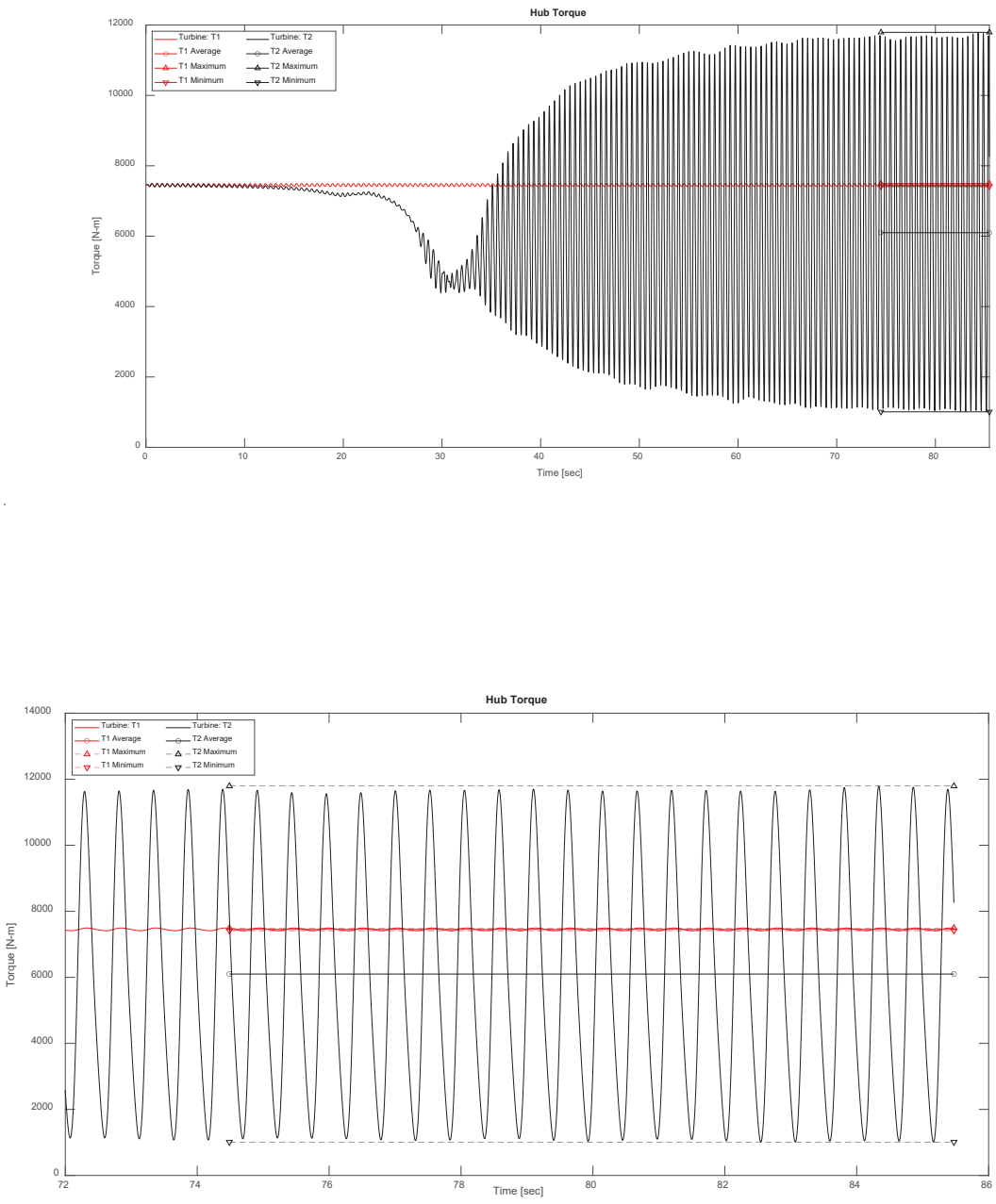

Figure 6.4: Time evolution of the hub torque of the NRT BsLn twin-turbine, tandem configuration for the NRTN1 scenario. Top: Full signal, Bottom: Close-up of the stable oscillatory regime.

Table 6.1
Summary of Axial Tip Deflection values of T1 and T2 in the stable oscillatory regime for the NRTD1 and NRTD2 scenarios.

Axial Tip Deflection [m]	Avg		Max		Min		Amp	
	T1	T2	T1	T2	T1	T2	T1	T2
BsLn D1	0.2884	0.2021	0.2950	0.3544	0.2802	0.1060	0.0148	0.2485
60SpSh D1	0.4082	0.2768	0.4177	0.4931	0.3962	0.1236	0.0216	0.3695
40SpSh D1	0.5543	0.3639	0.5668	0.6535	0.5382	0.1449	0.0286	0.5086
20SpSh D1	0.9586	0.5895	0.9764	1.0476	0.9350	0.2063	0.0414	0.8413
BsLn D2	0.2835	0.2780	0.2895	0.3054	0.2751	0.2344	0.0144	0.0710
60SpSh D2	0.4005	0.3933	0.4093	0.4259	0.3876	0.3248	0.0217	0.1010
40SpSh D2	0.5430	0.5326	0.5565	0.5665	0.5247	0.4322	0.0318	0.1343
20SpSh D2	0.9362	0.9090	0.9724	0.9821	0.8988	0.6954	0.0735	0.2867

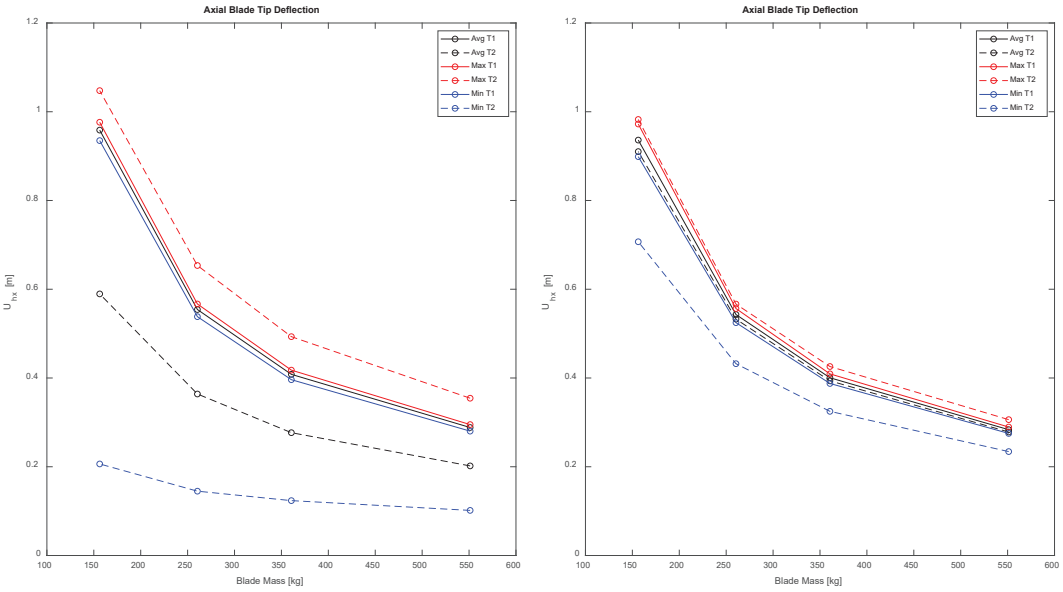

Figure 6.5: Plot of Axial Tip Deflection vs the mass of the NRT flex variants in the stable oscillatory regime for the NRTD1 and NRTD2 scenarios.

Table 6.2
Summary of Axial Tip Deflection values of T1 and T2 in the stable oscillatory regime for the NRTN1 and NRTN2 scenarios.

Axial Tip Deflection [m]	Avg		Max		Min		Amp	
	T1	T2	T1	T2	T1	T2	T1	T2
BsLn N1	0.2873	0.2615	0.3194	0.3581	0.2485	0.1591	0.0709	0.1991
60SpSh N1	0.4060	0.3659	0.4552	0.4894	0.3465	0.2181	0.1088	0.2713
40SpSh N1	0.5507	0.4917	0.6201	0.6338	0.4661	0.3103	0.1540	0.3235
20SpSh N1	0.9492	0.8349	1.0722	0.9874	0.7992	0.6279	0.2729	0.3595
BsLn N2	0.2820	0.2778	0.3124	0.3260	0.2428	0.2187	0.0696	0.1073
60SpSh N2	0.3978	0.3918	0.4449	0.4610	0.3373	0.3084	0.1076	0.1526
40SpSh N2	0.5386	0.5298	0.6063	0.6266	0.4524	0.4242	0.1539	0.2024
20SpSh N2	0.9255	0.9063	1.0541	1.0886	0.7711	0.7554	0.2830	0.3332

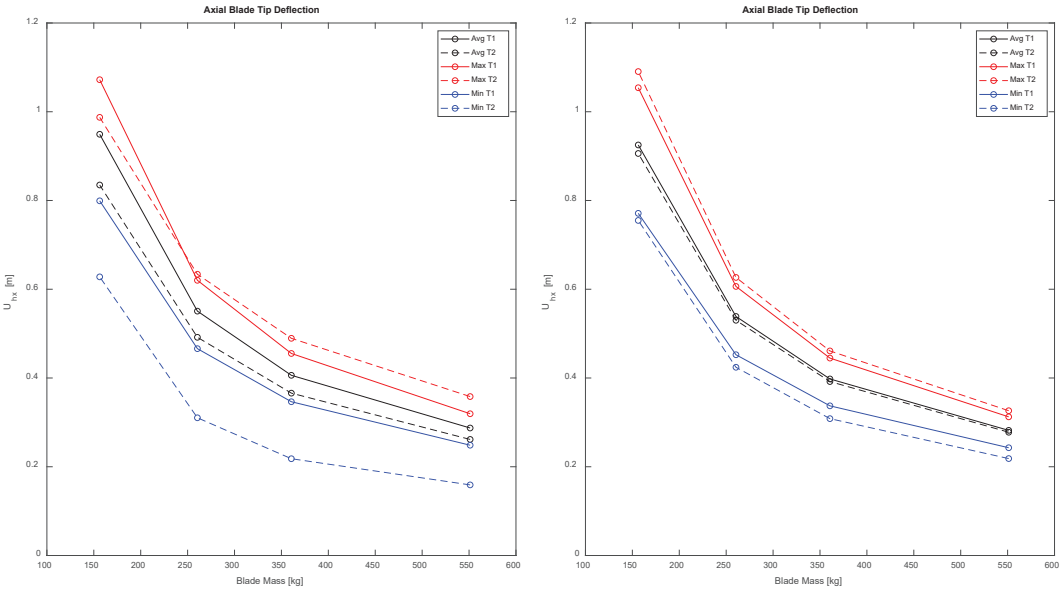

Figure 6.6: Plot of Axial Tip Deflection vs the mass of the NRT flex variants in the stable oscillatory regime for the NRTN1 and NRTN2 scenarios.

Table 6.3
Summary of blade-root flapswise bending moment values of T1 and T2 in the stable oscillatory regime for the NRTD1 and NRTD2 scenarios.

Root Bend Mom [N-m]	Avg		Max		Min		Amp	
	T1	T2	T1	T2	T1	T2	T1	T2
BsLn D1	32,969.30	23,130.49	33,662.59	39,447.96	32,122.51	13,075.19	1,540.08	26,372.76
60SpSh D1	29,497.38	19,871.09	30,146.83	34,757.11	28,697.53	9,621.39	1,449.30	25,135.72
40SpSh D1	27,568.98	17,903.08	28,165.25	31,768.54	26,824.51	7,680.64	1,340.74	24,087.90
20SpSh D1	25,155.31	15,038.63	25,622.09	26,985.77	24,566.69	5,904.69	1,055.40	21,081.08
BsLn D2	32,395.85	31,968.40	33,126.61	34,511.02	31,418.69	27,783.12	1,707.93	6,727.91
60SpSh D2	28,919.67	28,585.45	29,618.00	30,461.38	27,968.96	24,298.40	1,649.05	6,162.99
40SpSh D2	26,987.27	26,641.22	27,688.40	28,205.11	26,054.60	22,307.38	1,633.79	5,897.73
20SpSh D2	24,558.06	24,076.02	25,446.91	25,725.47	23,593.90	19,162.83	1,853.01	6,562.64

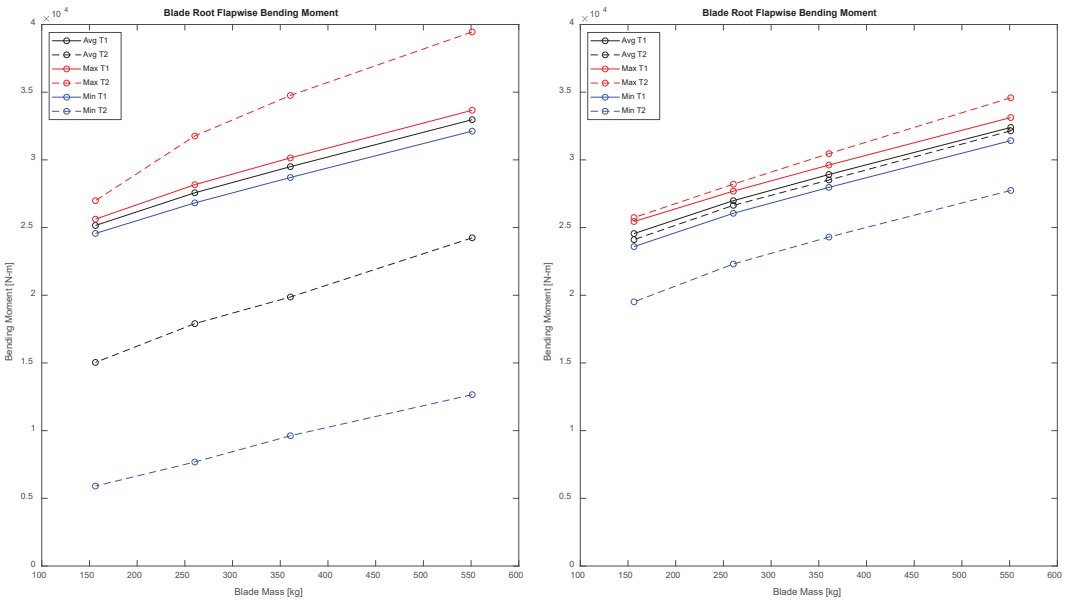

Figure 6.7: Plot of blade-root flapswise bending moment vs the mass of the NRT flex variants in the stable oscillatory regime for the NRTD1 and NRTD2 scenarios.

Table 6.4
Summary of blade-root flapswise bending moment values of T1 and T2 in the stable oscillatory regime for the NRTN1 and NRTN2 scenarios.

Root Bend Mom [N-m]	Avg		Max		Min		Amp	
	T1	T2	T1	T2	T1	T2	T1	T2
BsLn N1	32,881.00	30,412.91	36,197.95	39,739.22	28,943.84	19,833.07	7,254.12	19,906.15
60SpSh N1	29,386.44	26,932.07	32,650.95	34,406.08	25,506.24	17,205.91	7,144.71	17,200.17
40SpSh N1	27,439.75	24,954.80	30,634.91	31,268.48	23,622.81	16,714.98	7,012.09	14,553.50
20SpSh N1	24,978.72	22,439.75	27,968.93	26,015.69	21,404.16	17,387.13	6,564.77	8,628.56
BsLn N2	32,274.55	31,951.48	35,502.84	36,877.16	28,200.29	25,722.03	7,302.55	11,155.12
60SpSh N2	28,776.91	28,500.91	31,984.02	33,047.87	24,744.95	22,862.43	7,239.07	10,185.44
40SpSh N2	26,826.29	26,544.56	30,018.60	30,949.82	22,851.79	21,586.28	7,166.80	9,363.54
20SpSh N2	24,351.82	24,009.50	27,532.00	28,355.09	20,596.45	20,209.97	6,935.54	8,145.11

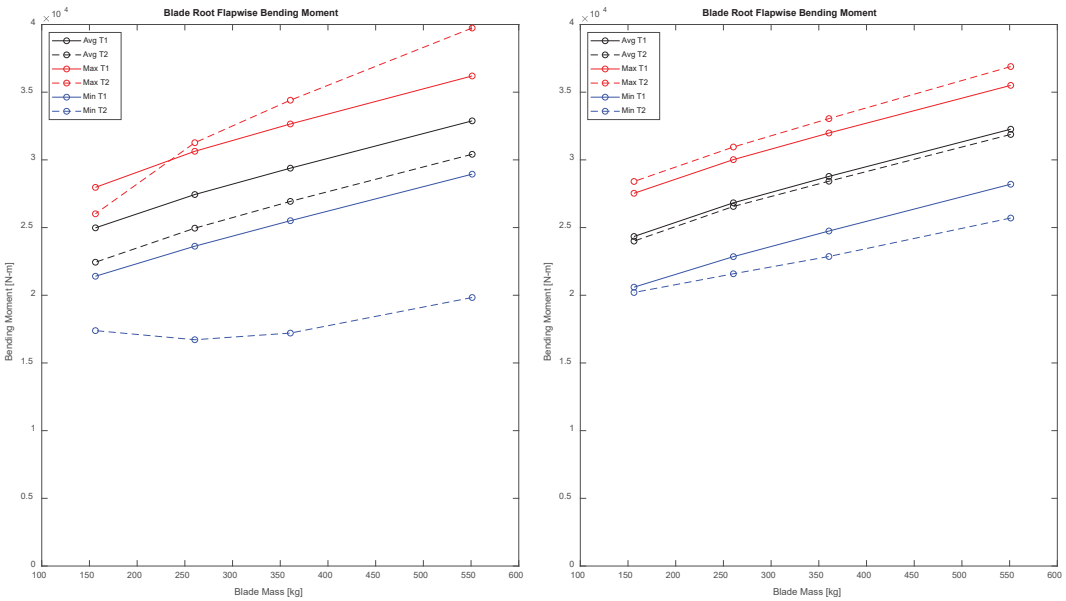

Figure 6.8: Plot of blade-root flapswise bending moment vs the mass of the NRT flex variants in the stable oscillatory regime for the NRTN1 and NRTN2 scenarios.

Table 6.5
Summary of hub torque values of T1 and T2 in the stable oscillatory regime for the NRTD1 and NRTD2 scenarios.

Torque [N-m]	Avg		Max		Min		Amp	
	T1	T2	T1	T2	T1	T2	T1	T2
BsLn D1	7,438.95	2,433.98	7,454.06	3,923.18	7,423.92	1,329.09	30.14	2,594.09
60SpSh D1	7,410.39	2,499.83	7,423.15	3,748.04	7,397.92	1,594.54	25.23	2,153.50
40SpSh D1	7,377.11	2,488.12	7,387.73	3,267.82	7,367.07	1,830.07	20.66	1,437.75
20SpSh D1	7,250.89	2,325.01	7,257.06	2,809.52	7,244.69	1,792.93	12.38	1,016.60
BsLn D2	7,082.87	6,858.61	7,098.58	8,487.82	7,067.70	5,551.21	30.88	2,936.61
60SpSh D2	7,056.06	6,893.57	7,067.70	8,147.81	7,042.33	5,707.20	25.37	2,440.61
40SpSh D2	7,025.84	6,849.27	7,032.11	7,865.77	7,015.52	5,755.58	16.59	2,110.18
20SpSh D2	6,912.37	6,696.98	6,918.08	7,435.94	6,908.36	5,629.36	9.72	1,806.58

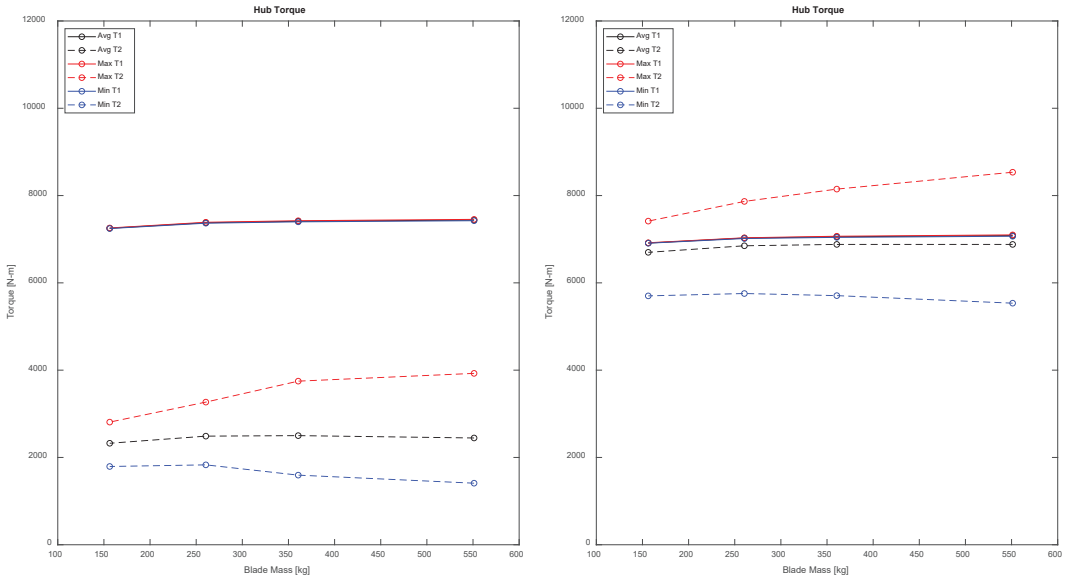

Figure 6.9: Plot of hub torque vs the mass of the NRT flex variants in the stable oscillatory regime for the NRTD1 and NRTD2 scenarios.

Table 6.6
Summary of hub torque values of T1 and T2 in the stable oscillatory regime for the NRTN1 and NRTN2 scenarios.

Torque [N-m]	Avg		Max		Min		Amp	
	T1	T2	T1	T2	T1	T2	T1	T2
BsLn N1	7,452.02	5,956.92	7,494.37	11,791.48	7,411.42	1,009.05	82.96	10,782.43
60SpSh N1	7,416.89	5,935.79	7,450.65	10,547.95	7,385.04	1,521.54	65.61	9,026.40
40SpSh N1	7,374.64	5,890.31	7,403.34	9,506.51	7,350.43	2,002.44	52.91	7,504.08
20SpSh N1	7,220.34	5,767.71	7,247.93	7,893.99	7,200.62	3,024.62	47.32	4,869.36
BsLn N2	7,134.87	6,968.44	7,201.23	8,620.77	7,084.94	5,609.63	116.29	3,011.14
60SpSh N2	7,101.21	6,975.41	7,163.93	8,327.12	7,053.08	5,717.65	110.85	2,609.47
40SpSh N2	7,061.17	6,939.44	7,123.99	8,024.47	7,008.80	5,797.52	115.19	2,226.96
20SpSh N2	6,913.89	6,770.57	6,980.37	7,427.68	6,852.90	5,954.30	127.47	1,473.38

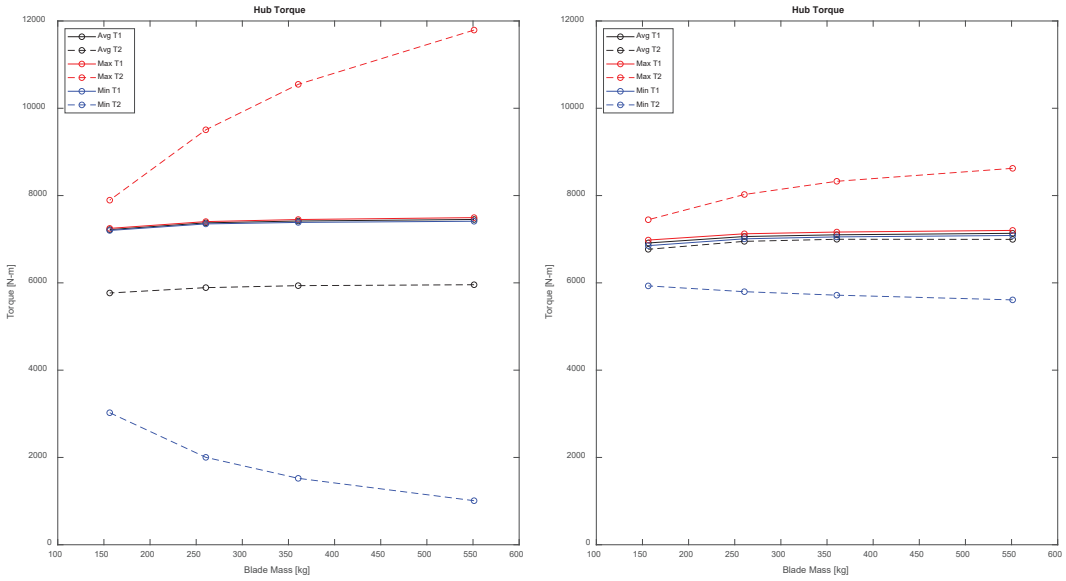

Figure 6.10: Plot of hub torque vs the mass of the NRT flex variants in the stable oscillatory regime for the NRTN1 and NRTN2 scenarios.

Table 6.7
Summary of hub thrust values of T1 and T2 in the stable oscillatory regime for the NRTD1 and NRTD2 scenarios.

Thrust [N]	Avg		Max		Min		Amp	
	T1	T2	T1	T2	T1	T2	T1	T2
BsLn D1	9,238.45	5,408.45	9,246.13	5,963.10	9,230.75	4,903.73	15.37	1,059.37
60SpSh D1	9,206.87	5,427.34	9,213.41	5,920.17	9,200.47	5,012.53	12.94	907.65
40SpSh D1	9,164.92	5,361.42	9,170.44	5,654.89	9,159.78	5,119.02	10.66	535.87
20SpSh D1	9,018.18	5,112.54	9,021.50	5,225.25	9,014.91	4,968.21	6.59	257.04
BsLn D2	9,010.09	8,882.39	9,018.17	9,592.50	9,001.65	8,198.46	16.52	1,394.04
60SpSh D2	8,976.89	8,880.51	8,982.67	9,431.53	8,969.50	8,294.07	13.17	1,137.46
40SpSh D2	8,932.99	8,830.64	8,937.14	9,275.70	8,926.71	8,315.20	10.43	960.50
20SpSh D2	8,780.20	8,637.39	8,784.00	8,941.27	8,774.77	8,194.17	9.23	747.10

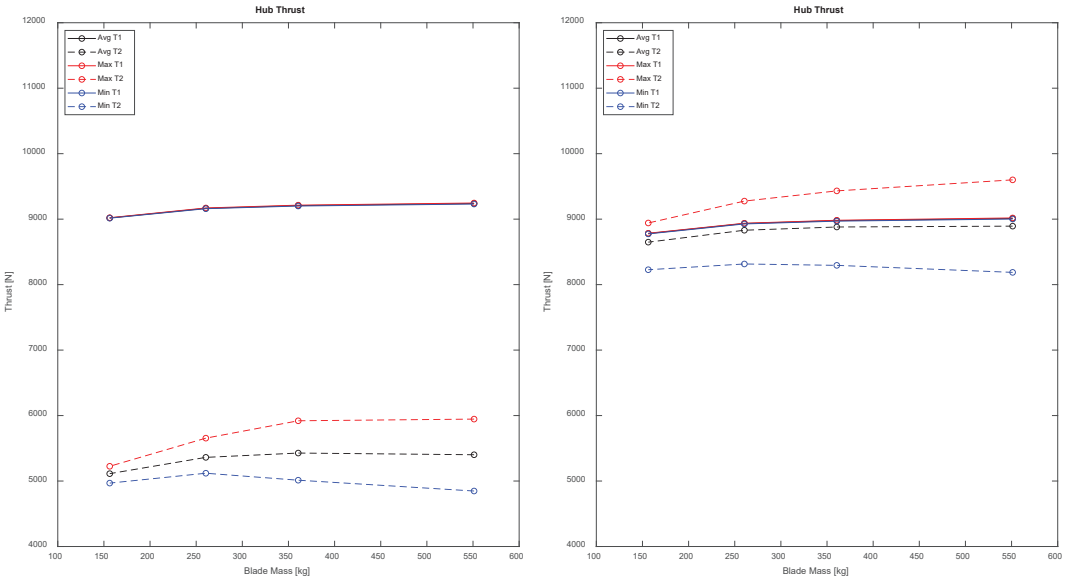

Figure 6.11: Plot of hub thrust vs the mass of the NRT flex variants in the stable oscillatory regime for the NRTD1 and NRTD2 scenarios.

Table 6.8
Summary of hub thrust values of T1 and T2 in the stable oscillatory regime for the NRTN1 and NRTN2 scenarios.

Thrust [N]	Avg		Max		Min		Amp	
	T1	T2	T1	T2	T1	T2	T1	T2
BsLn N1	9,210.70	8,334.28	9,236.76	10,986.73	9,184.67	5,716.63	52.09	5,270.10
60SpSh N1	9,174.32	8,301.07	9,195.35	10,465.62	9,153.32	6,052.33	42.03	4,413.29
40SpSh N1	9,126.03	8,241.78	9,142.89	9,945.89	9,109.30	6,349.03	33.60	3,596.86
20SpSh N1	8,961.20	8,055.16	8,975.03	8,964.42	8,948.15	6,859.99	26.88	2,104.43
BsLn N2	8,971.14	8,873.46	8,995.14	9,558.36	8,949.82	8,193.16	45.31	1,365.20
60SpSh N2	8,933.39	8,854.87	8,955.37	9,412.82	8,914.69	8,268.72	40.67	1,144.11
40SpSh N2	8,883.36	8,803.26	8,904.04	9,246.30	8,866.15	8,296.35	37.89	949.95
20SpSh N2	8,712.19	8,607.99	8,730.19	8,864.66	8,693.93	8,265.32	36.26	599.33

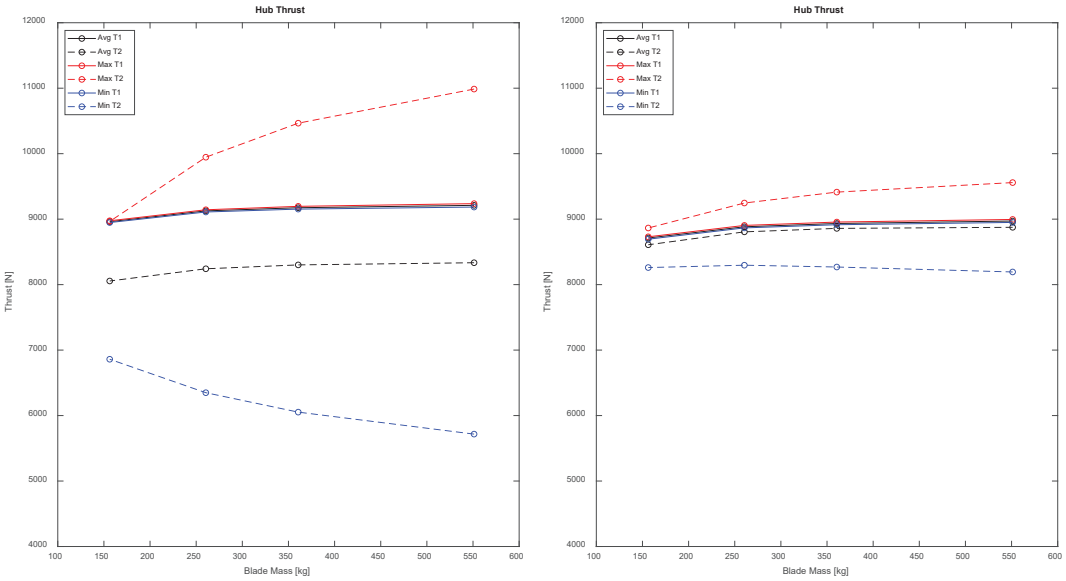

Figure 6.12: Plot of hub thrust vs the mass of the NRT flex variants in the stable oscillatory regime for the NRTN1 and NRTN2 scenarios.

Table 6.9
Summary of power values of T1 and T2 in the stable oscillatory regime for the NRTD1 and NRTD2 scenarios.

Power [W]	Avg		Max		Min		Amp	
	T1	T2	T1	T2	T1	T2	T1	T2
BsLn D1	29,755.80	9,735.91	29,816.24	15,692.71	29,695.70	5,316.37	120.55	10,376.35
60SpSh D1	29,641.56	9,999.32	29,692.60	14,992.18	29,591.67	6,378.17	100.93	8,614.00
40SpSh D1	29,508.44	9,952.49	29,550.92	13,071.27	29,468.29	7,320.27	82.63	5,751.00
20SpSh D1	29,003.57	9,203.82	29,028.25	11,238.10	28,978.75	7,171.70	49.50	4,066.40
BsLn D2	28,331.49	27,434.46	28,394.31	33,951.30	28,270.79	22,204.85	123.52	11,746.45
60SpSh D2	28,224.24	27,574.29	28,270.81	32,591.26	28,169.33	22,828.82	101.48	9,762.44
40SpSh D2	28,103.34	27,446.89	28,128.43	31,463.06	28,062.07	23,022.33	66.36	8,440.73
20SpSh D2	27,649.49	26,787.92	27,672.32	29,743.76	27,633.43	22,517.43	38.90	7,226.33

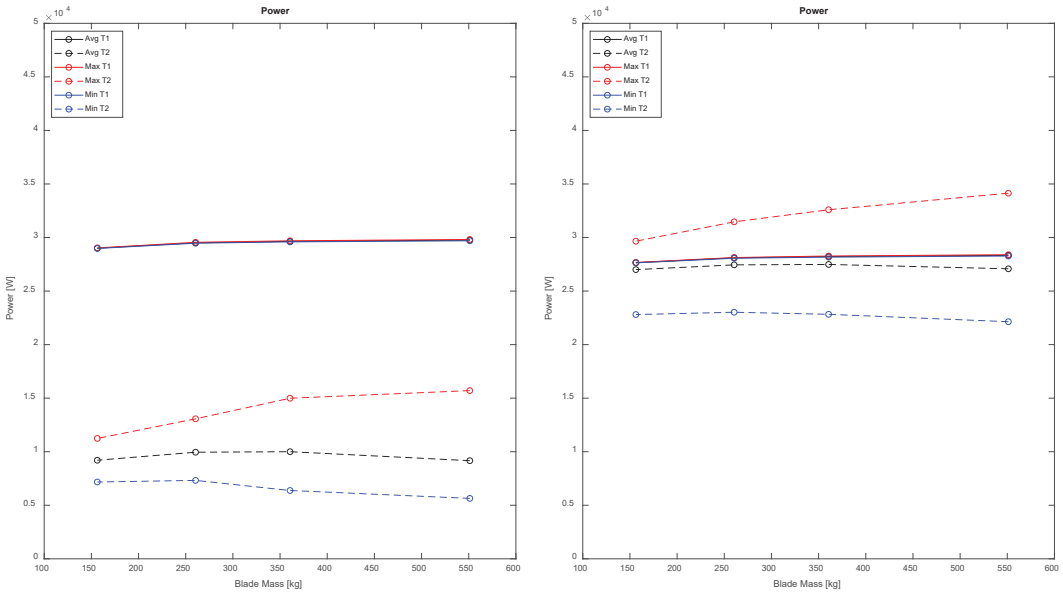

Figure 6.13: Plot of powerv vs the mass of the NRT flex variants in the stable oscillatory regime for the NRTD1 and NRTD2 scenarios.

Table 6.10
Summary of power values of T1 and T2 in the stable oscillatory regime for the NRTN1 and NRTN2 scenarios.

Power [W]	Avg		Max		Min		Amp	
	T1	T2	T1	T2	T1	T2	T1	T2
BsLn N1	29,808.09	23,827.69	29,977.50	47,165.92	29,645.66	4,036.18	331.83	43,129.74
60SpSh N1	29,667.57	23,743.18	29,802.60	42,191.78	29,540.16	6,086.17	262.44	36,105.62
40SpSh N1	29,498.55	23,561.24	29,613.36	38,026.06	29,401.72	8,009.74	211.65	30,016.32
20SpSh N1	28,881.38	23,070.83	28,991.73	31,575.96	28,802.47	12,098.50	189.26	19,477.46
BsLn N2	28,539.47	27,873.76	28,804.93	34,483.07	28,339.77	22,438.53	465.16	12,044.54
60SpSh N2	28,404.84	27,901.66	28,655.71	33,308.47	28,212.32	22,870.59	443.39	10,437.88
40SpSh N2	28,244.67	27,757.78	28,495.94	32,097.89	28,035.19	23,190.07	460.75	8,907.82
20SpSh N2	27,655.56	27,082.28	27,921.47	29,710.71	27,411.59	23,817.18	509.88	5,893.52

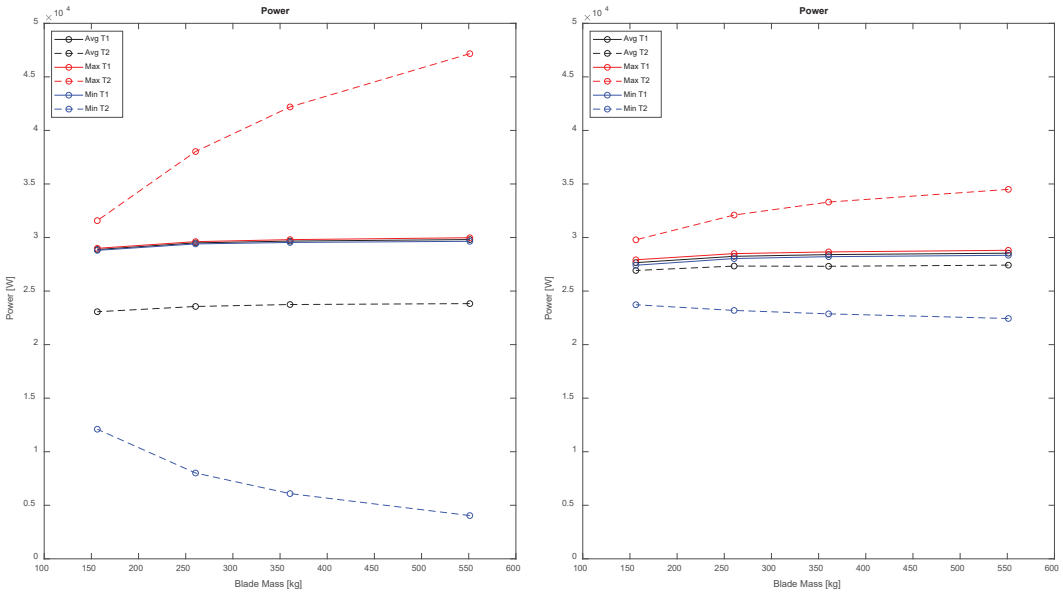

Figure 6.14: Plot of power vs the mass of the NRT flex variants in the stable oscillatory regime for the NRTN1 and NRTN2 scenarios.

6.2 Vortex Wake Evolution in Twin-Turbine Farm

In this section we focus on the turbine-to-turbine wake interaction within a farm. This complex wake interactions are depicted by the axial wake velocity patterns at several transverse planes located along the streamwise axis of the wind turbine farm. From a distance of 1D upstream of T1, these transverse planes are located every 1D downstream upto T2. From T2 to further 5D downstream of it, they're located every 0.25D, resulting in the planes located at a total distance of 10D from T1.

Velocity patterns for the twin-turbine NRT BsLn farm for the scenarios in 4.3 are presented below. A perspective view of all the cut planes is followed by front view of each individual transverse plane.

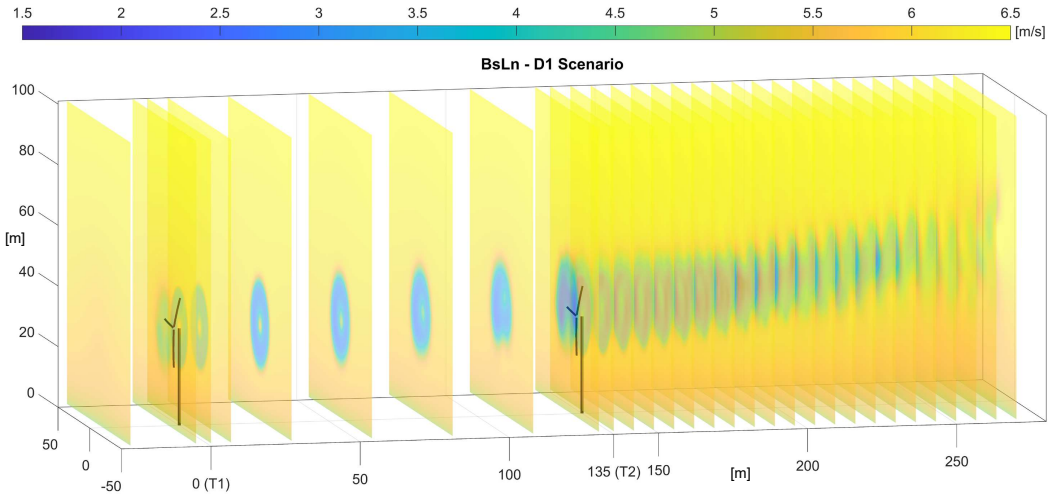

Figure 6.15: Velocity pattern of the twin-turbine wake for the BsLn twin-turbine farm operating in the NRTD1 scenario at several transverse planes along the streamwise direction.

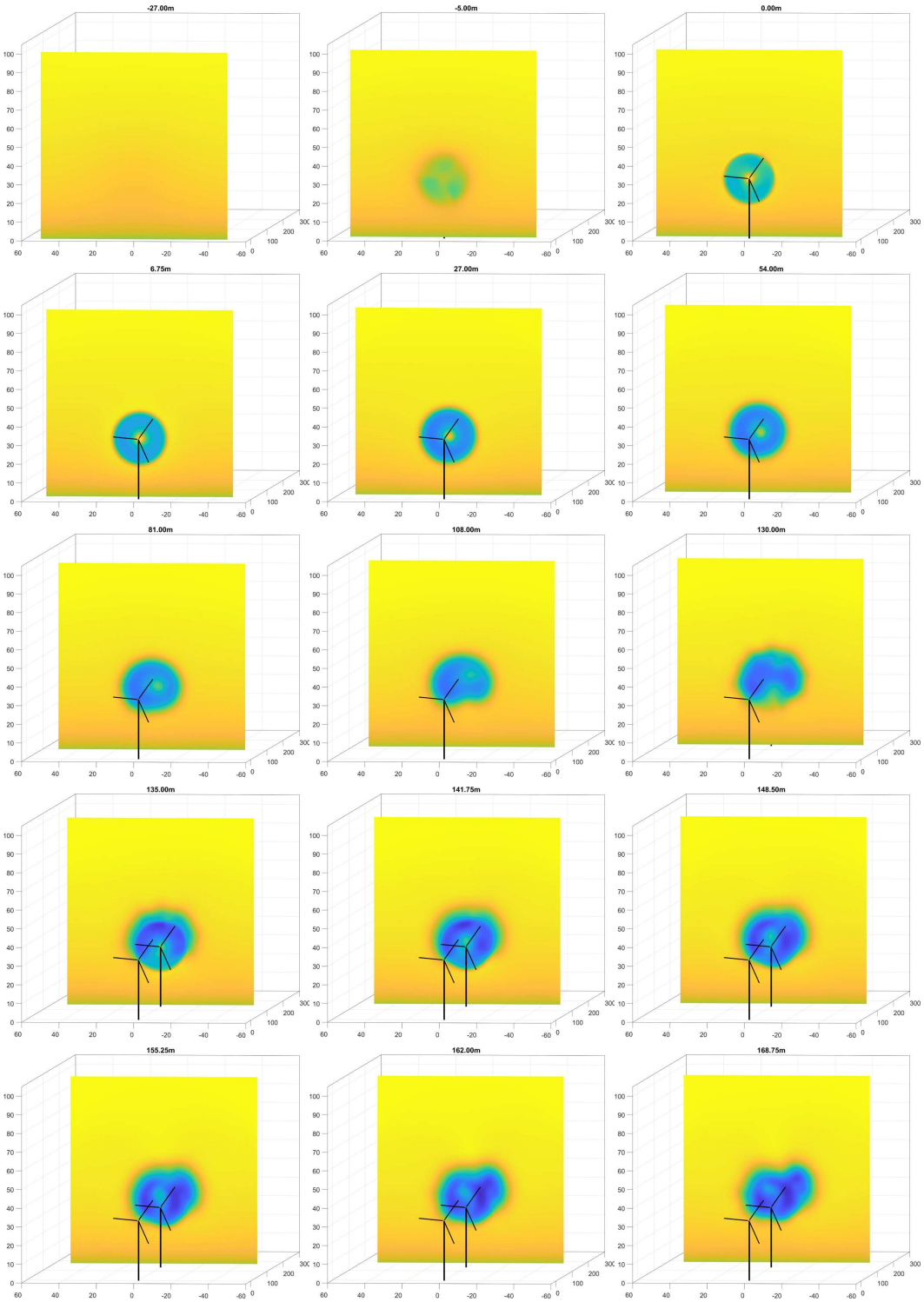
-27.00m
-5.00m
0.00m
6.75m
27.00m
54.00m
81.00m
108.00m
130.00m
135.00m
141.75m
148.50m
155.25m
162.00m
168.75m

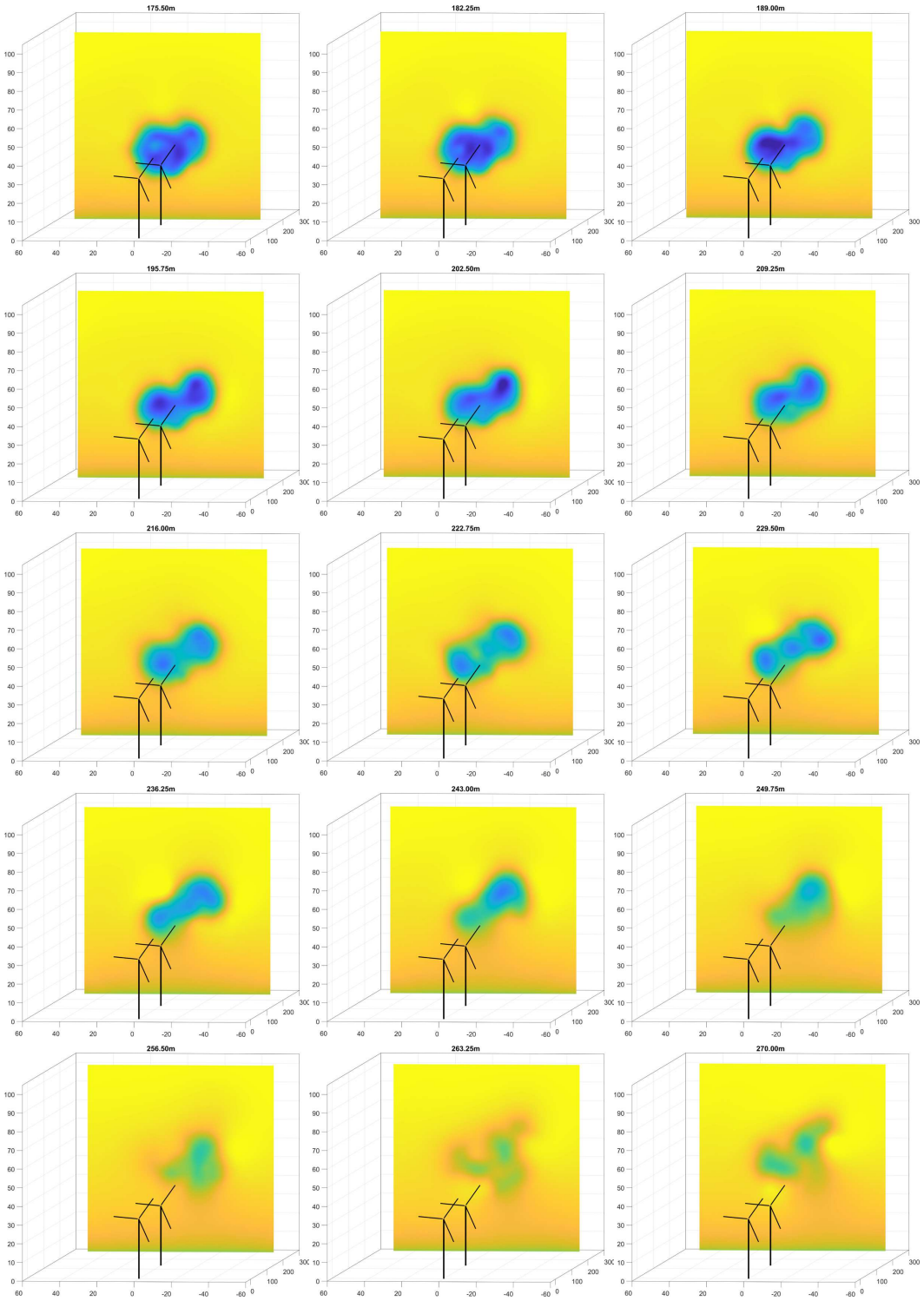

Figure 6.16: Front view of streamwise wake velocity at individual transverse planes along the streamwise direction for the BsLn twin-turbine farm operating in the NRTD1 scenario. (All axes in [m]).

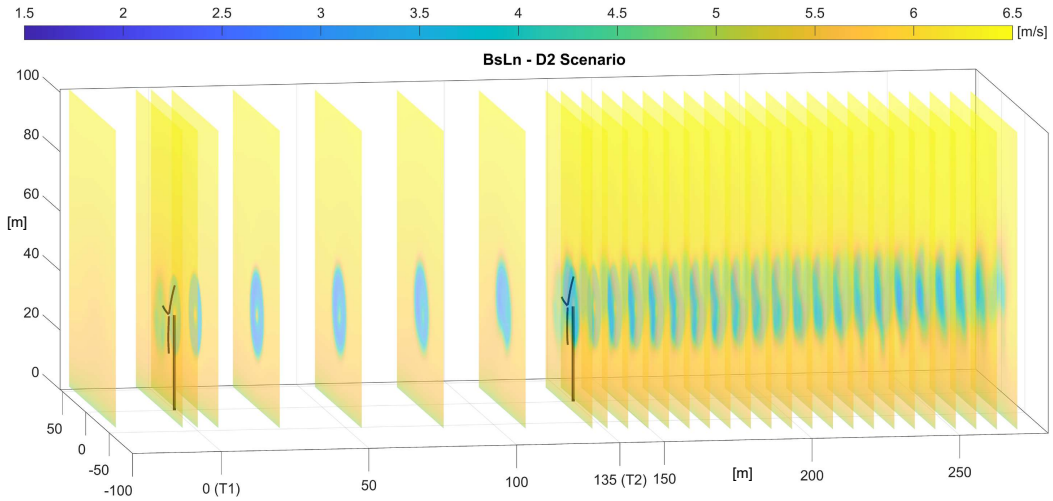

Figure 6.17: Velocity pattern of the twin-turbine wake for the BsLn twin-turbine farm operating in the NRTD2 scenario at several transverse planes along the streamwise direction.

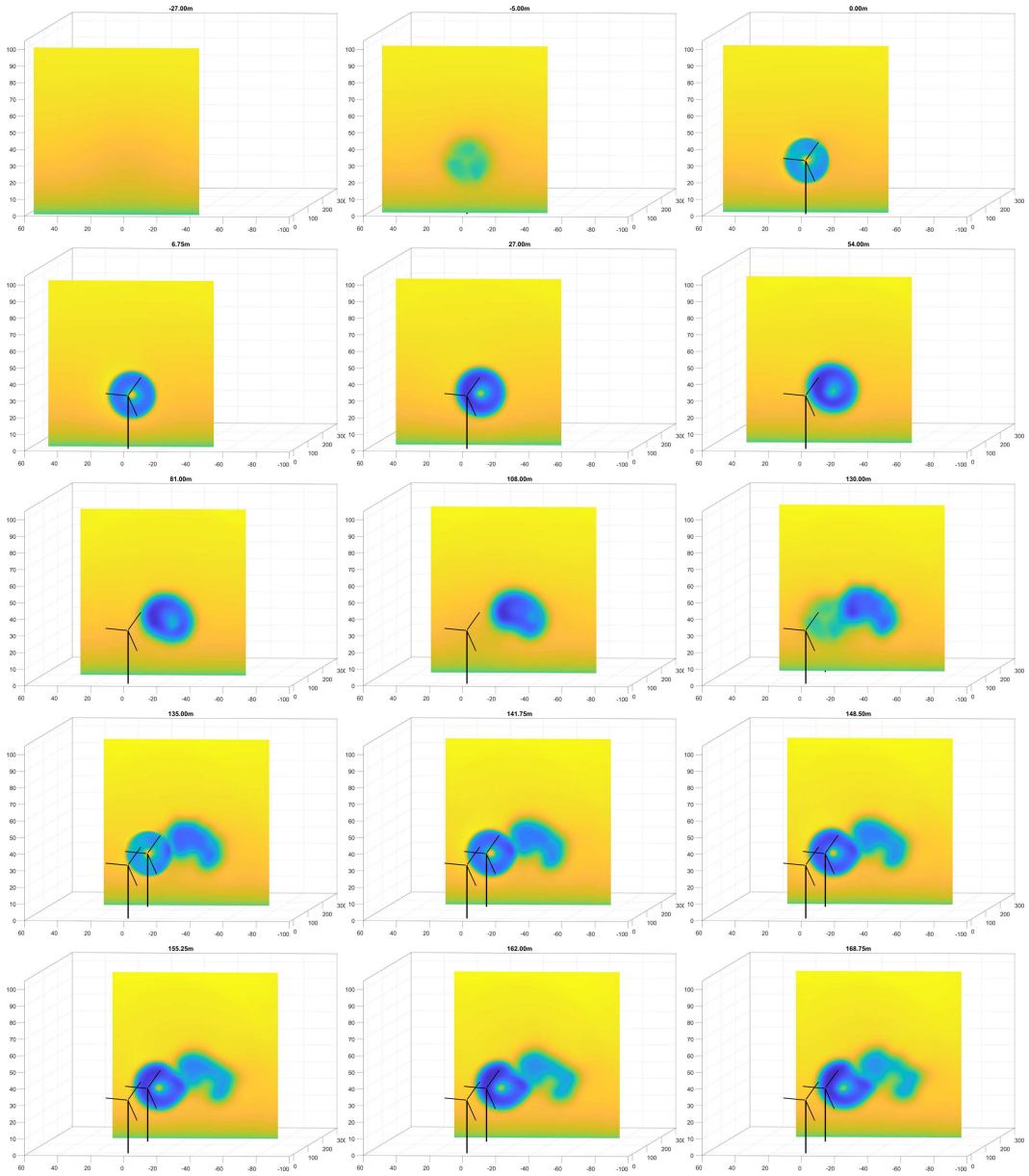
-27.00m
-5.00m
0.00m
6.75m
27.00m
54.00m
81.00m
108.00m
130.00m
135.00m
141.75m
148.50m
155.25m
162.00m
168.75m

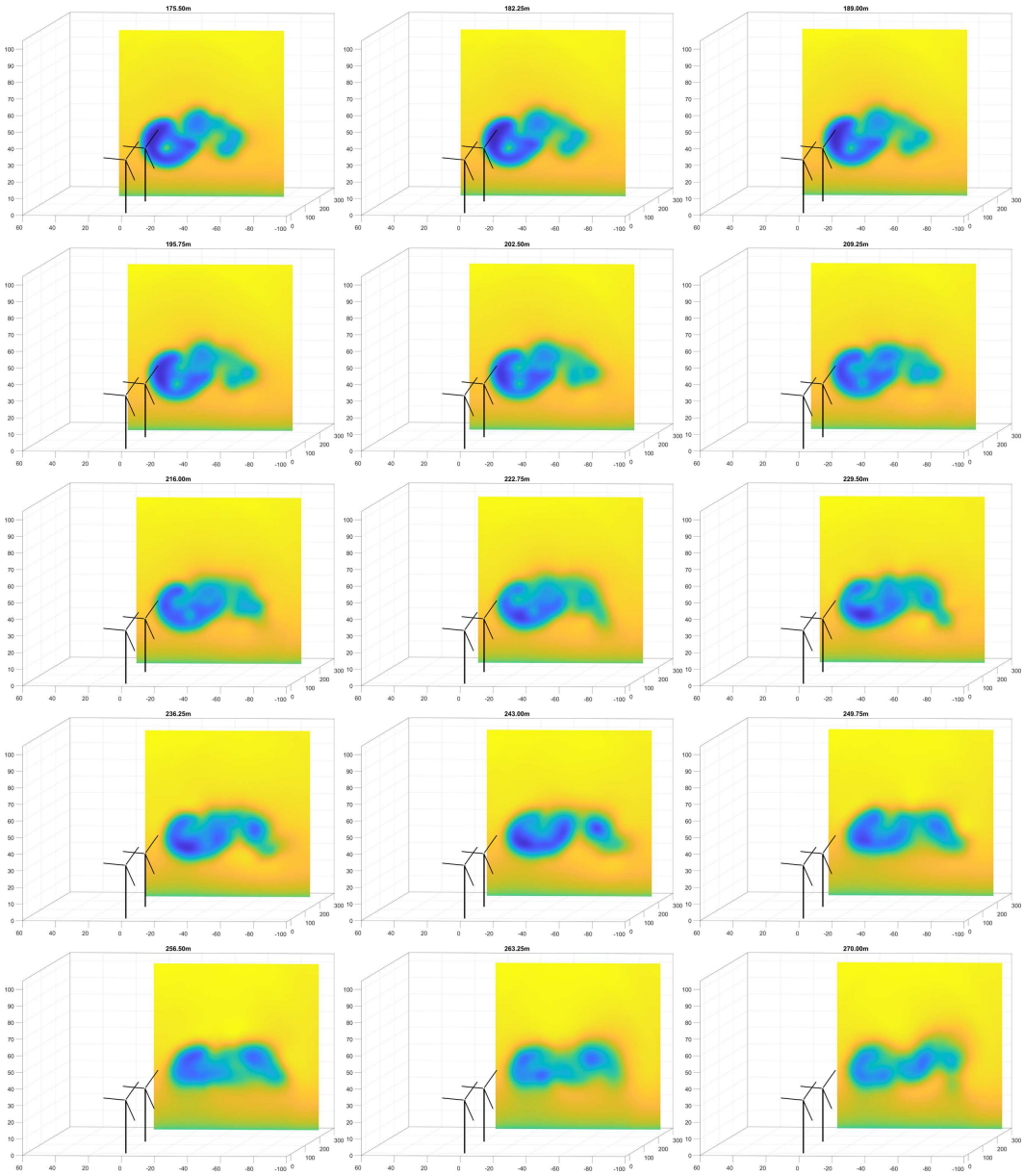

Figure 6.18: Front view of streamwise wake velocity at individual transverse planes along the streamwise direction for the BsLn twin-turbine farm operating in the NRTD2 scenario. (All axes in [m]).

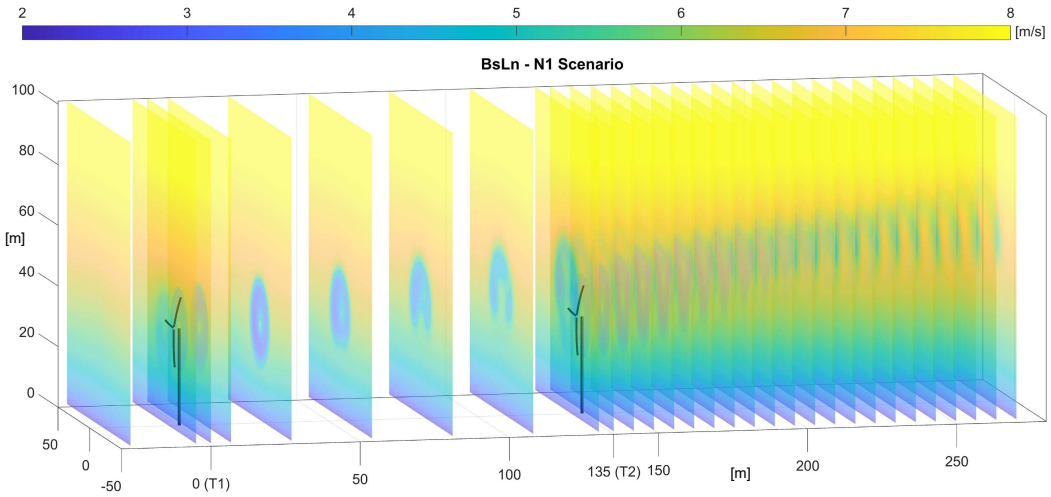

Figure 6.19: Velocity pattern of the twin-turbine wake for the BsLn twin-turbine farm operating in the NRTN1 scenario at several transverse planes along the streamwise direction.

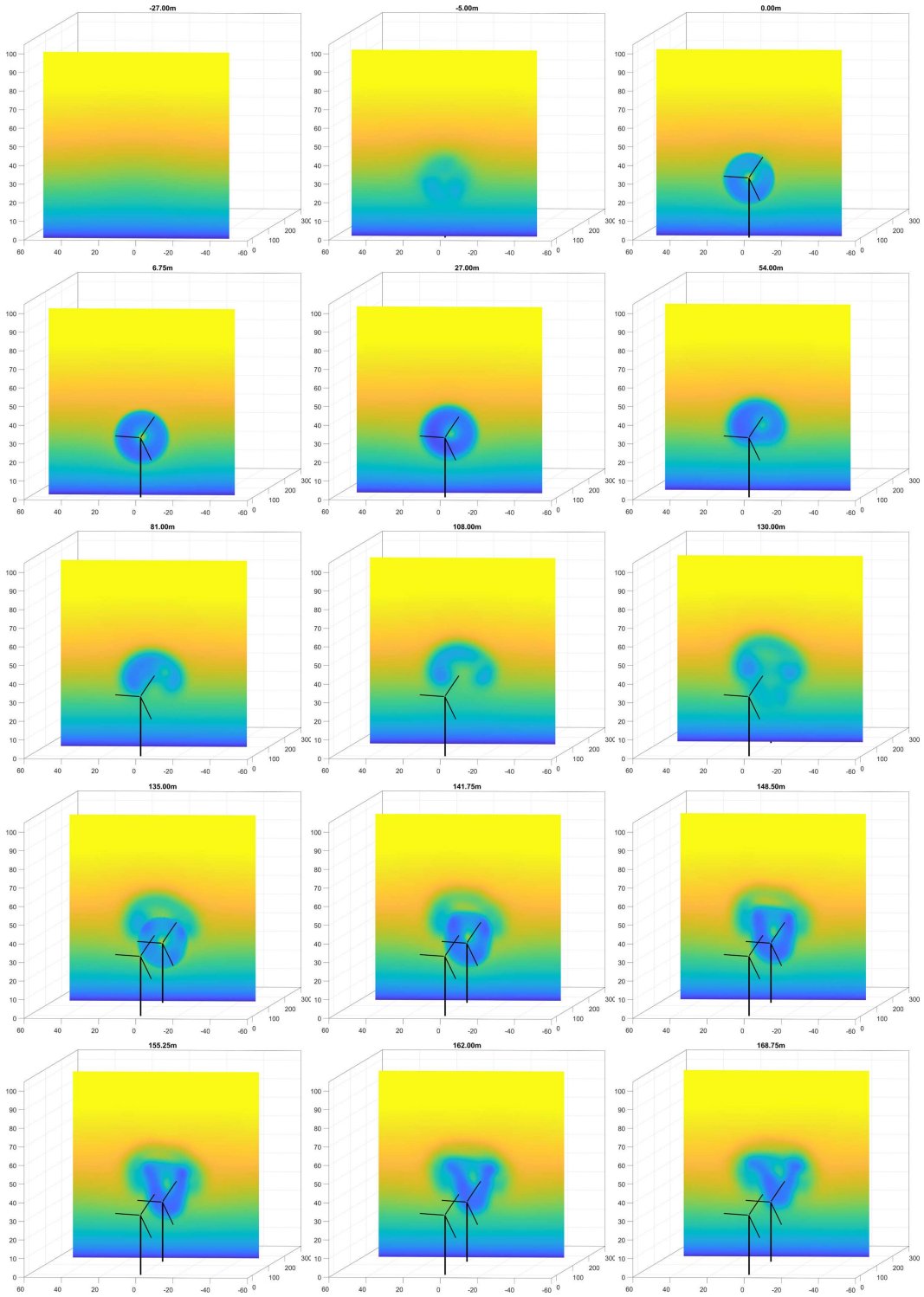
-27.00m
-5.00m
0.00m
6.75m
27.00m
54.00m
81.00m
108.00m
130.00m
135.00m
141.75m
148.50m
155.25m
162.00m
168.75m

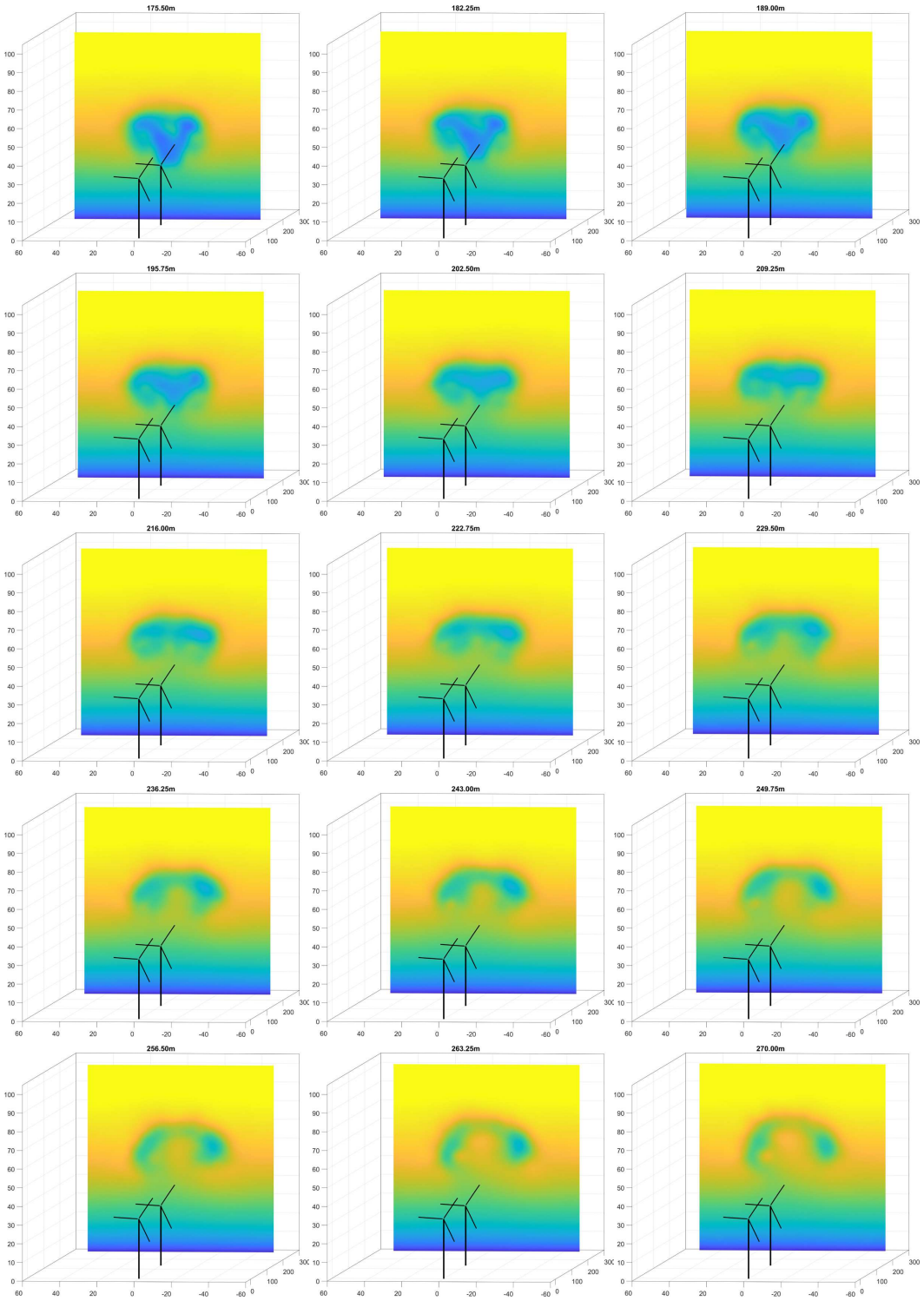

Figure 6.20: Front view of streamwise wake velocity at individual transverse planes along the streamwise direction for the BsLn twin-turbine farm operating in the NRTN1 scenario. (All axes in [m]).

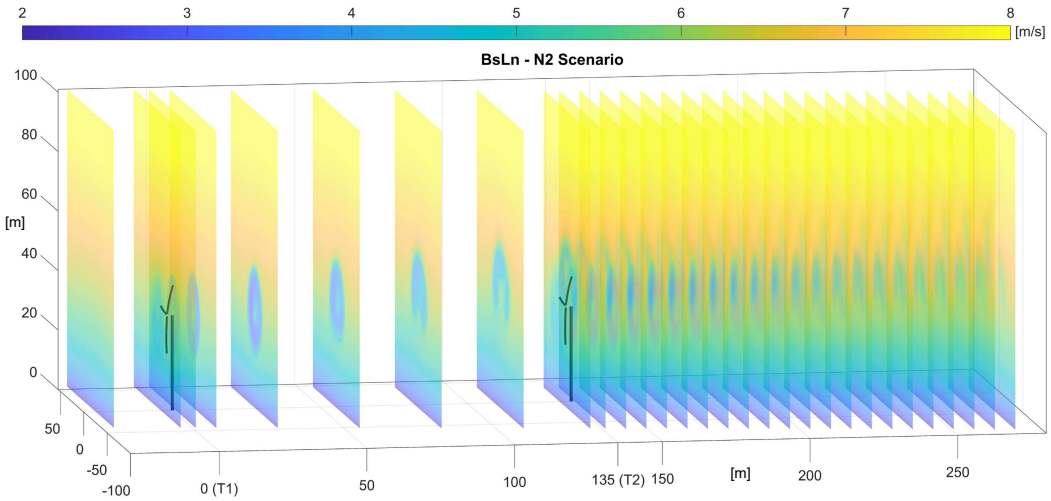

Figure 6.21: Velocity pattern of the twin-turbine wake for the BsLn twin-turbine farm operating in the NRTN2 scenario at several transverse planes along the streamwise direction.

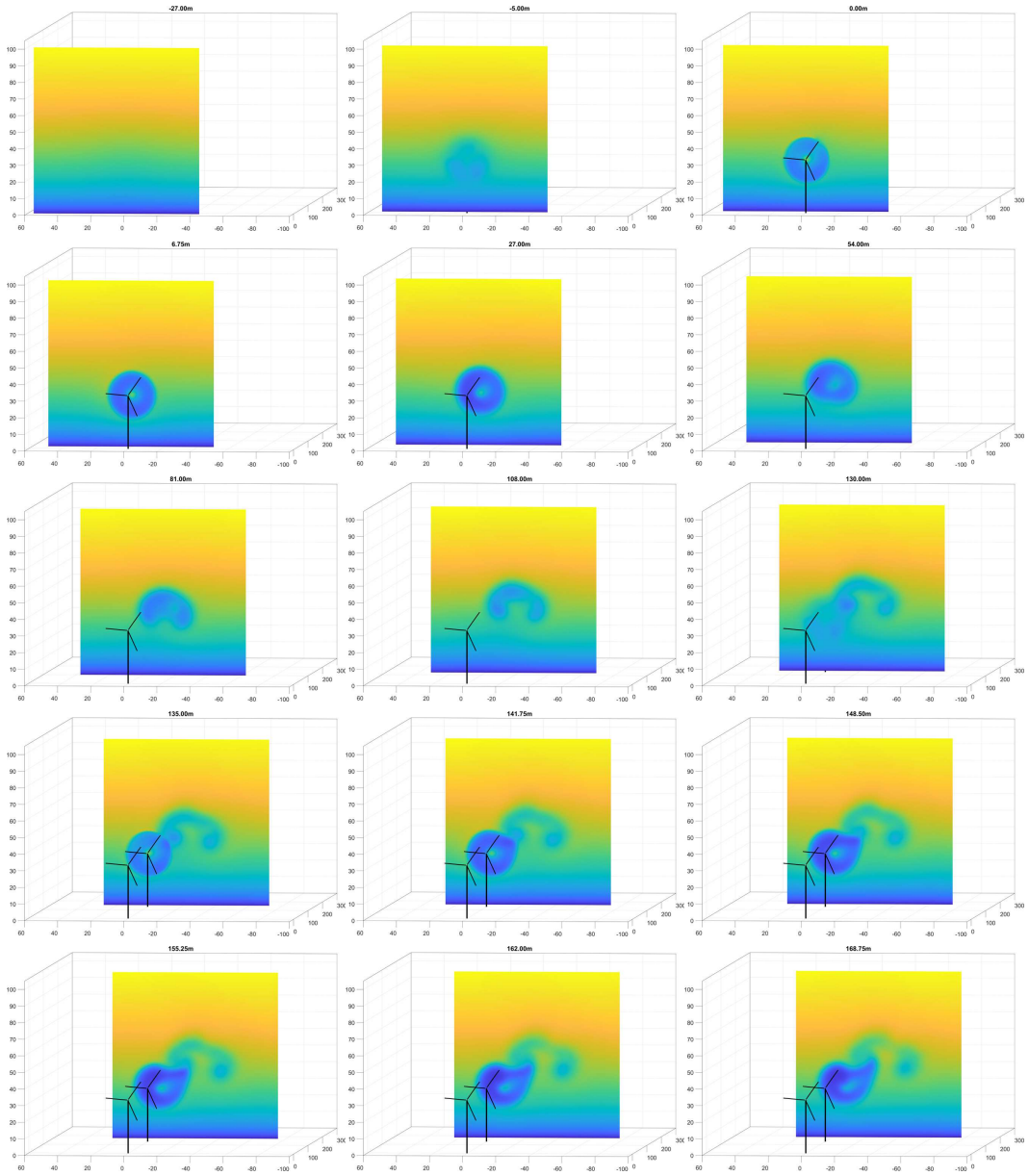
-27.00m
-5.00m
0.00m
6.75m
27.00m
54.00m
81.00m
108.00m
130.00m
135.00m
141.75m
148.50m
155.25m
162.00m
168.75m

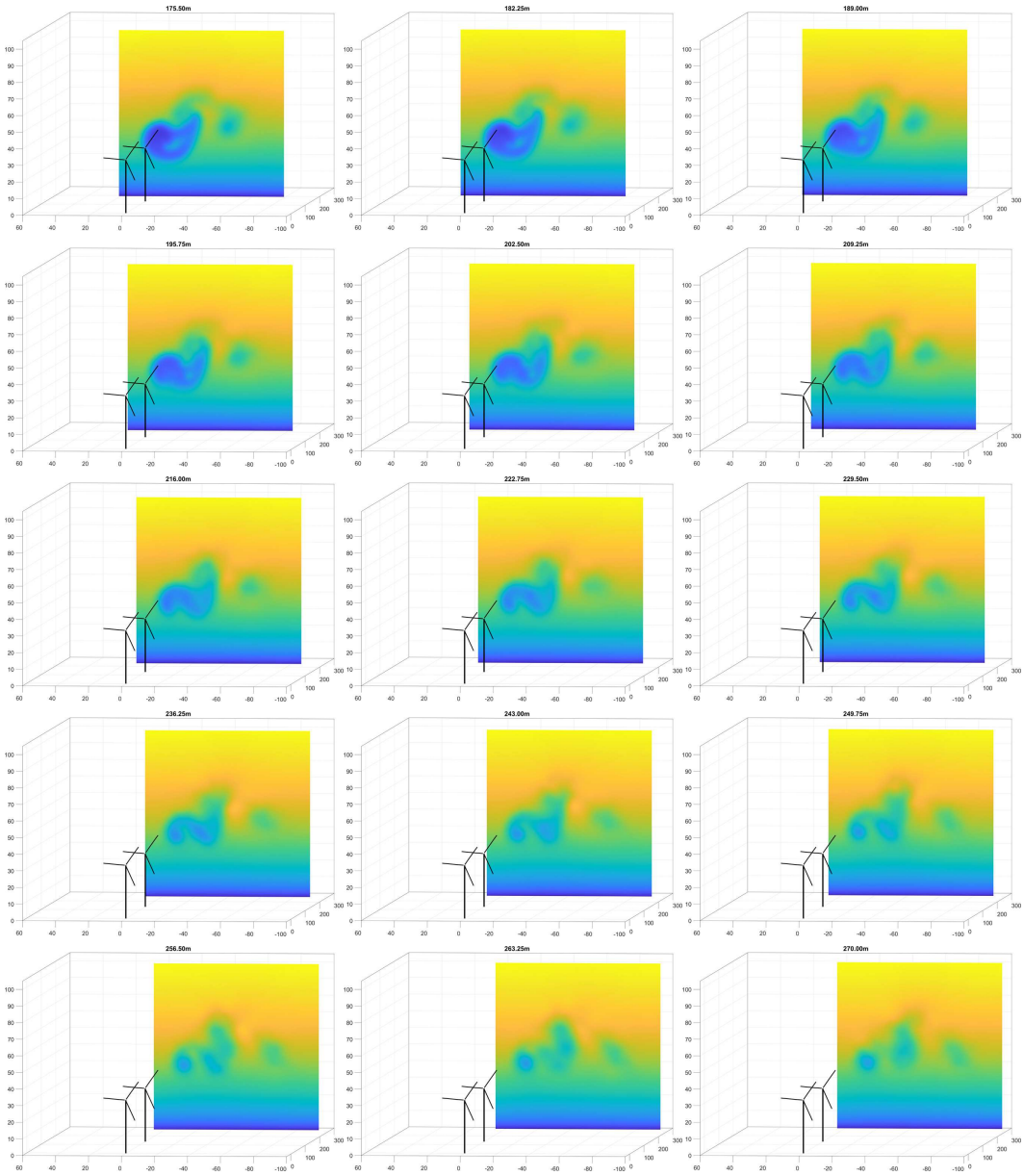

Figure 6.22: Front view of streamwise wake velocity at individual transverse planes along the streamwise direction for the BsLn twin-turbine farm operating in the NRTN2 scenario. (All axes in [m]).

Chapter 7

Simulation of the Collective Wake Interaction in Multi-Turbine Wind Farm Arrays

4-Turbine NRT Farm

After observing the successful turbine-to-turbine interaction of the twin-turbine, tandem configuration, we proceeded for simulations of farms with an increasing number of turbines. Our next iteration was a four turbine farm, arranged as a 2x2 array, with a streamwise spacing of 5D and cross-stream spacing of 3D. This layout was chosen similar to the spacing of turbines at the SWiFT facility, in line with future expansions

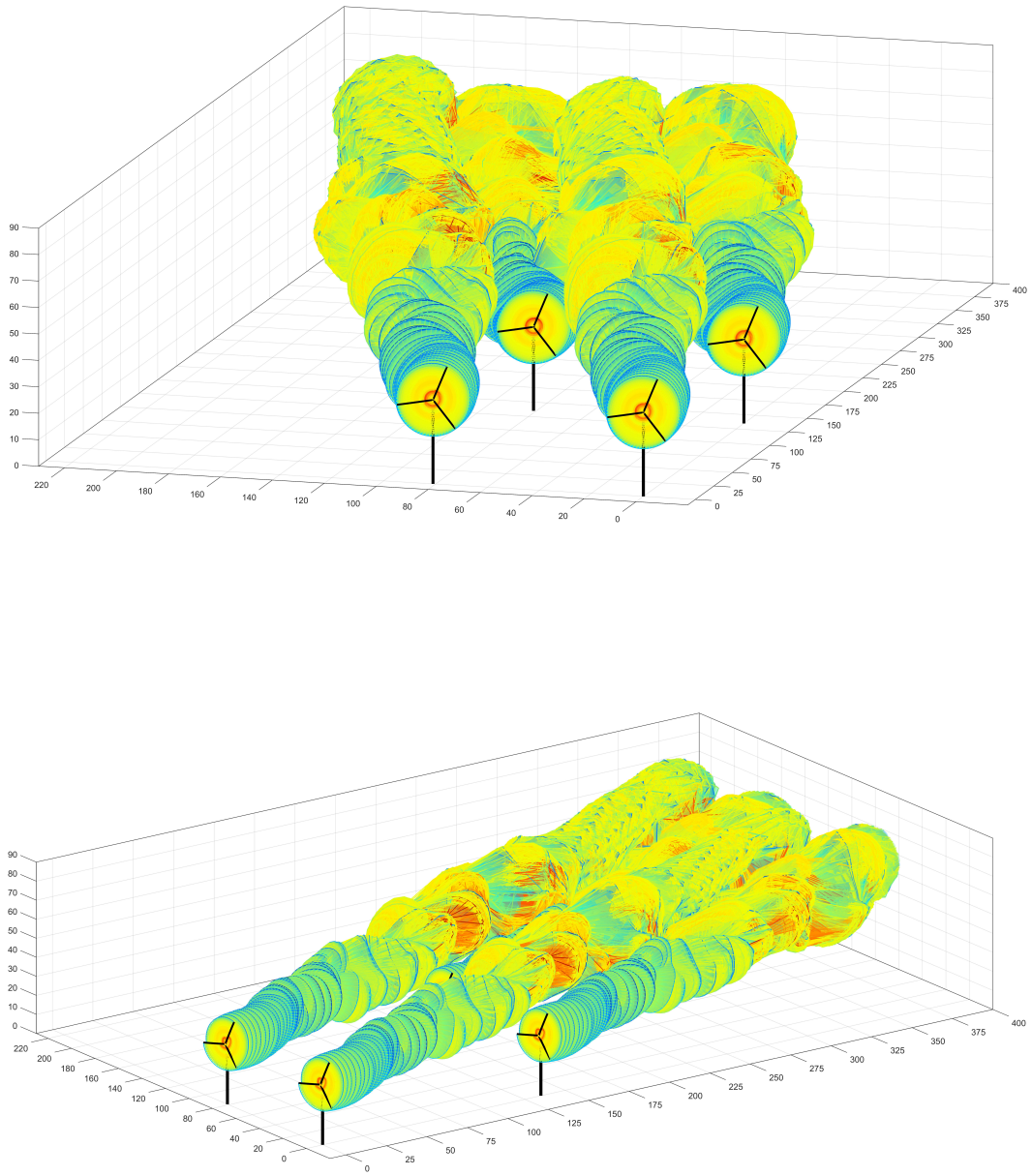

Figure 7.1: Different perspective views of the vortex lattice wake interaction of the 2x2 Farm. (All axes in [m]).

and wake measurment campaigns as described in [35].

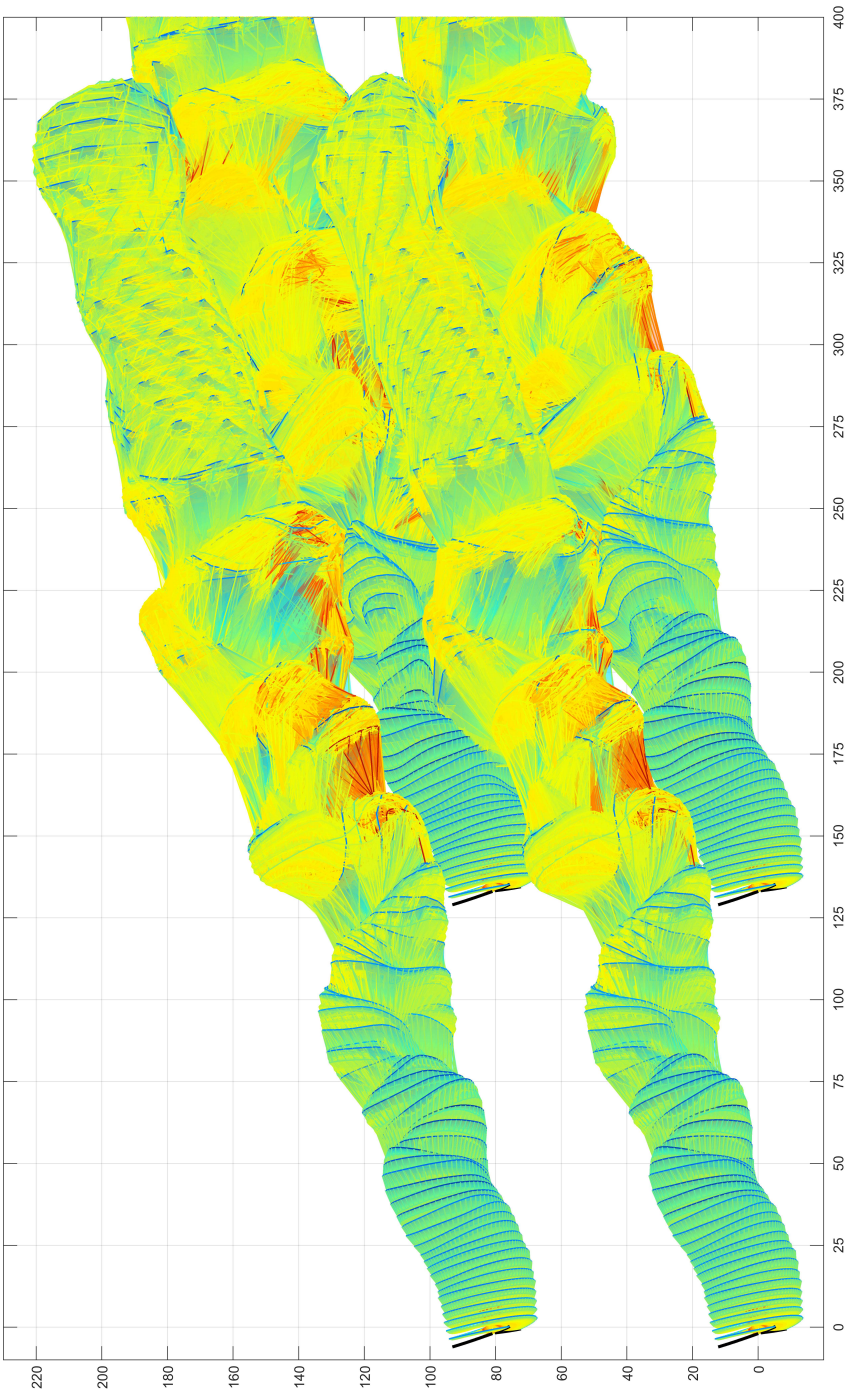

Figure 7.2: Top view of the vortex lattice wake interaction of the 2x2 Farm. (All axes in [m]).

9-Turbine NRT Farm

Further extending the farm size, we designed a farm with 9 NRT turbines in a 3x3 layout. This arrangement allowed for the evolution of the vortex wake over 2 downstream rows of turbine. It enables the complex interaction of the wakes of different turbines based on varying amounts of overlap with each other.

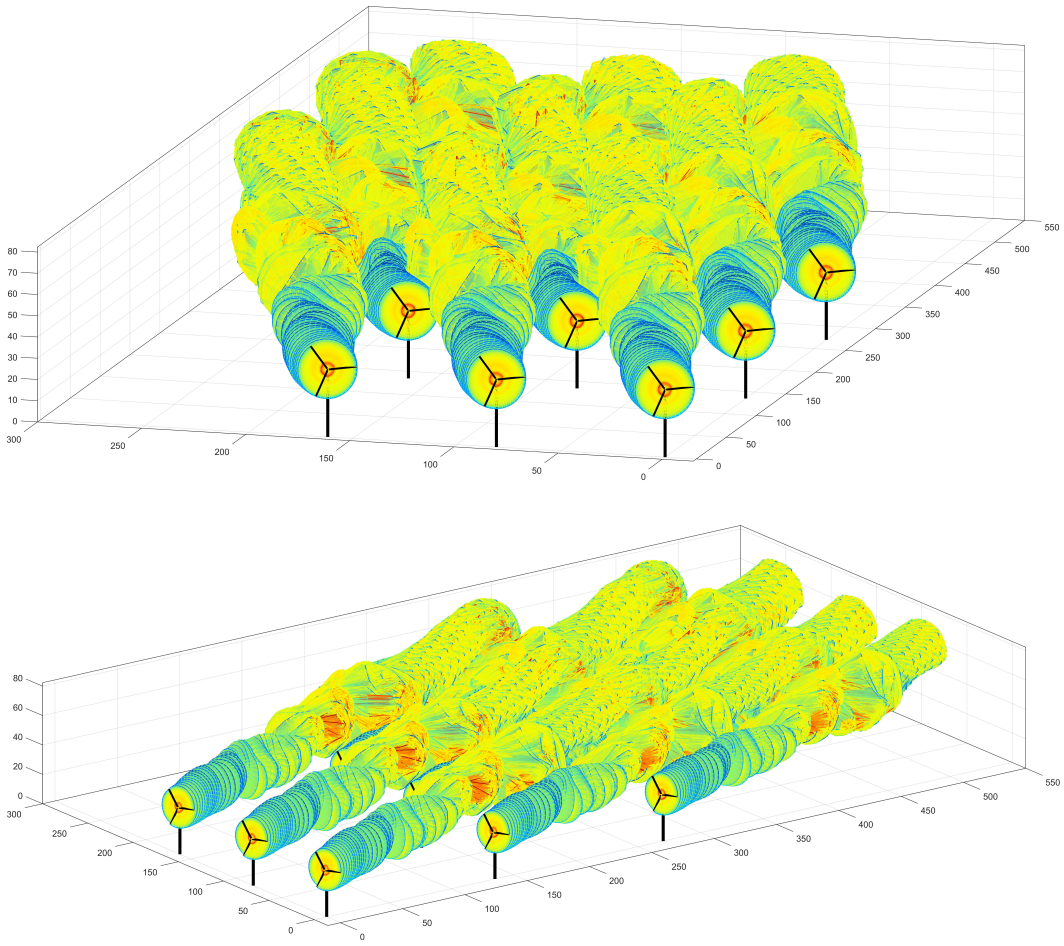

Figure 7.3: Different perspective views of the vortex lattice wake interaction of the 3x3 Farm. (All axes in [m]).

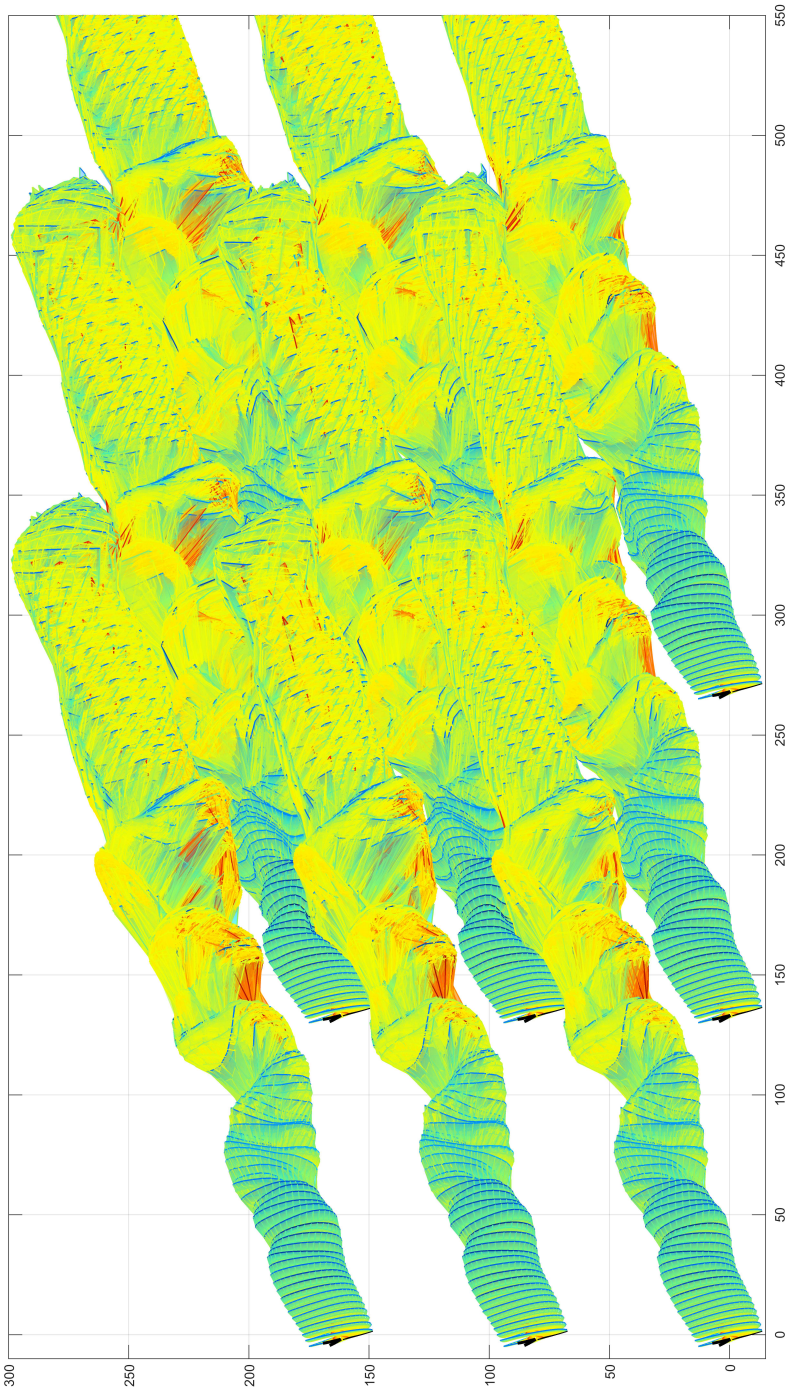

Figure 7.4: Top view of the vortex lattice wake interaction of the 3x3 Farm. (All axes in [m]).

20-Turbine NRT Farm

Finally, we ran simulations to the maximum available computational hardware - a workstation with a 64-core AMD ThreadripperPro 3995WX (Zen2) CPU. With four cores to spare for network and other system tasks, the 20-turbine farm simulation completely utilises the remaining sixty available cores for the simulation. The computational cost of this simulation is orders of magnitude lower than that of a comparable LES (which would require a HPC cluster) - especially with the considerations of the simulations being run on a desktop workstation computer of a form factor and size comparable to that of performance desktop computers, and its associated low power consumption scaling.

The 20-turbine farm consisted of four rows of five turbines each. The inflow input consisted of a complete transient anemometry measurement, with the average parameters namely, wind speed of 6.87m/s, wind direction : 217°(wind coming from the S-SW), vertical shear exponent of 0.39, and veer of 16.14 °.

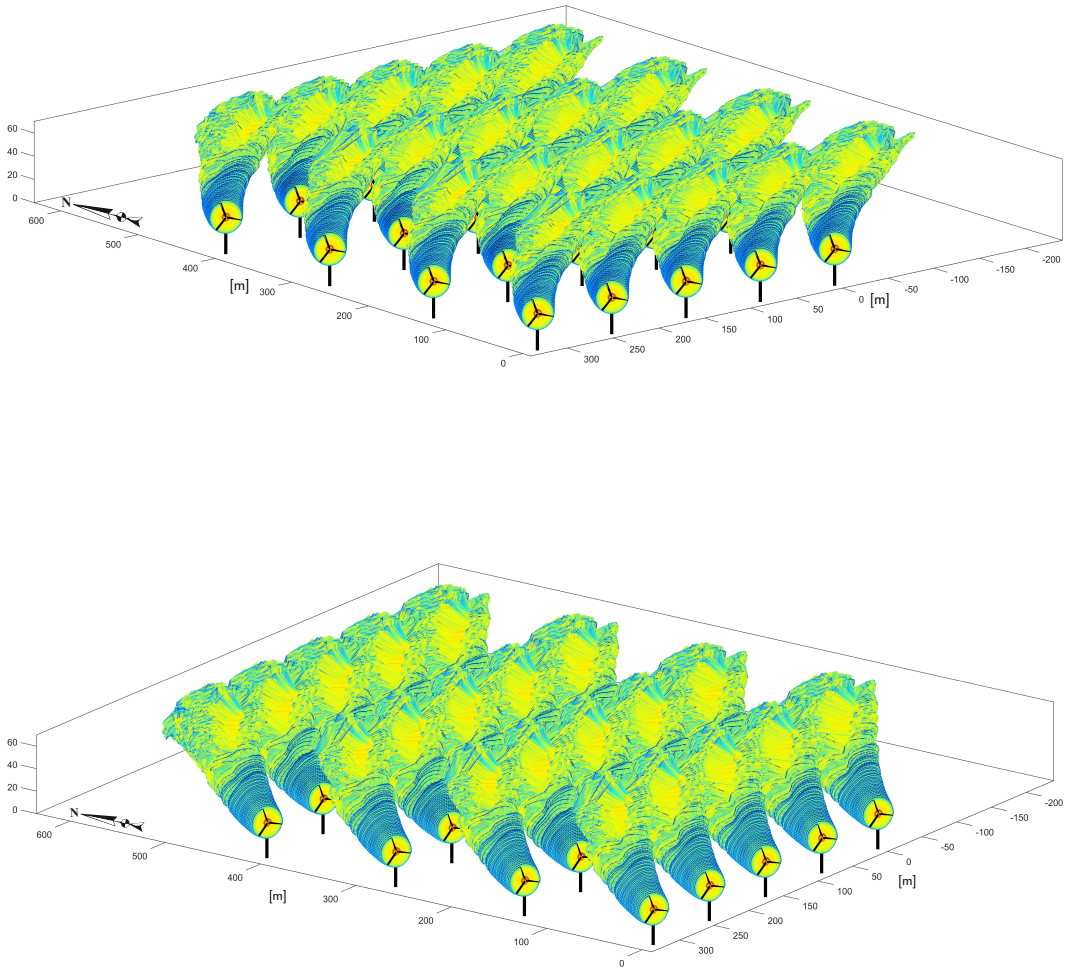

Figure 7.5: Different perspective views of the vortex lattice wake interaction of the 4x5 Farm.

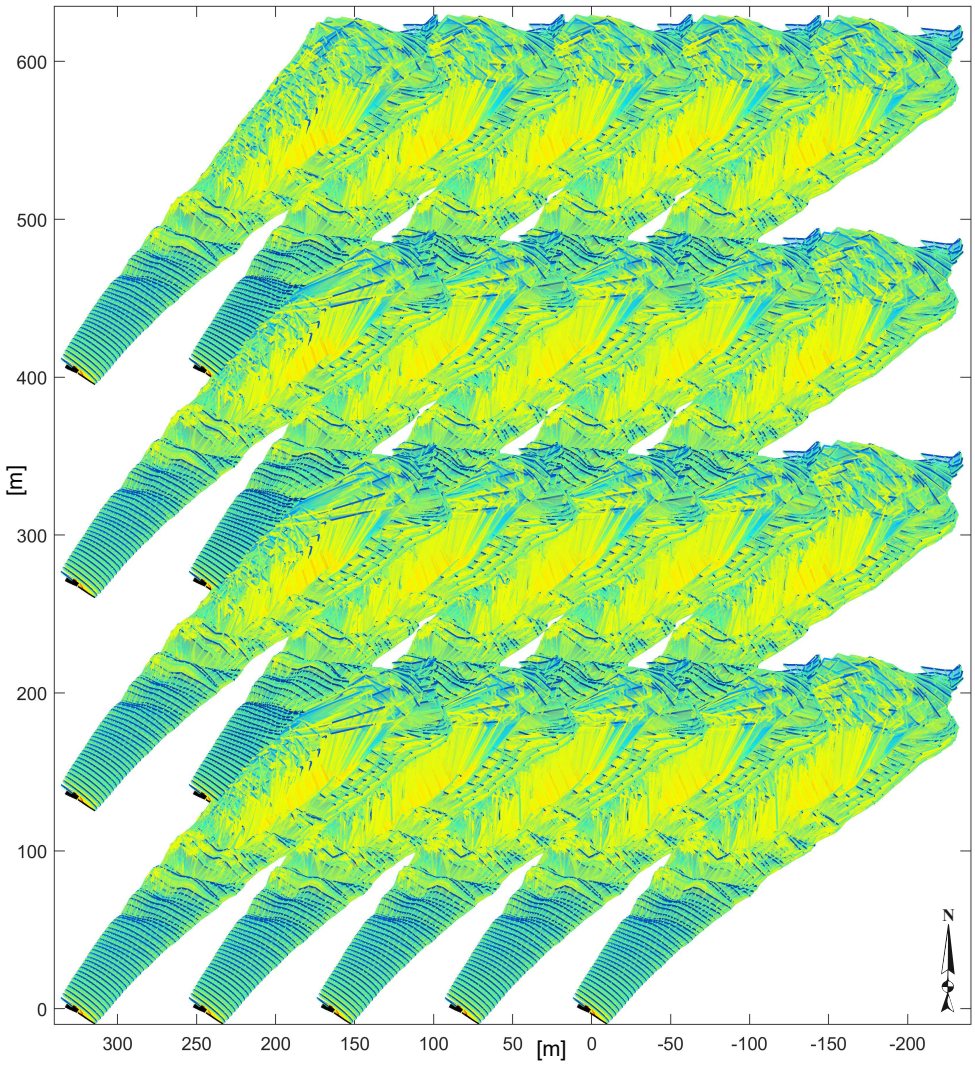

Figure 7.6: Top view of the vortex lattice wake interaction of the 4x5 Farm.

Chapter 8

Conclusion and Future Work

Through the current endeavor presented in this dissertation, we've seen the successful integration of the Gaussian-core vortex lattice model with the high-fidelity aeroelastic routines, DRD-BEM thereby expanding the capabilities of the CODEF multi-physics suite.

The vortex wake implementation is devoid of any singularities/computational irregularities. The stability of the model was demonstrated for the N5M-RWT with a vortex wake *extending more than 15D downstream*. This initial model validation paved the way for simulations with complex inflows for a diverse set of wind turbine blades.

The field validation campaign showcases the model's responsiveness to the transient wind inputs and different turbine blades. The current GVLM implementation involves

the use of the same flow details obtained from the met tower (or as experienced at the turbine) to compute the propagation of every filament node of all lattices. Despite this initial simple approach, the *remarkable qualitative similarities* in the computed and lidar measured v_{los} demonstrate the model's capabilities in *accurately* capturing the complex evolution of the vortex wake and the highly dynamic wake-to-wake interaction. Such similarities in the absence of any spatially-varying transient wind flow inputs reinforces the strength of the model and its responsiveness to the *tunable* parameters. Hence, even in its current form, the model can be extremely useful for quick, moderately-high fidelity engineering design stages involving wind turbine wakes.

The current model is stable to run farms comprised of multiple wind turbines using computational hardware which is available at a mere fraction of the cost (human, capital, and operational) of contemporary LES without significant compromise to its fidelity/results. Two turbine cases can be easily run on routine, performance desktop computers. Farms of up to *20-turbines* can be simulated on commercially available off-the-shelf, high-end desktop (HEDT) workstations.

Finally, scaling the simulation for up to 80-turbines, can be easily achieved with minimal modifications to the code. This 80-turbine capability is based on the planned/-expected commercial debut of twin-, 128-core CPU based HEDT workstations (AMD EPYC Zen series processors). Such low-cost, accessible high-performance hardware

eases model adoption and simulation scaling by orders of magnitude when compared to the complex HPC clusters required for LES simulations.

With this strong foundation, future endeavors are bound to augment GVLM's fidelity without a substantial increase in resources required. In terms of improvements to the model, developments to include the effects of the tower and nacelle would lead to an accurate depiction of the real flow dynamics and the (especially near-field) vortex wake evolution.

One of the most important aspects in establishing accurate quantitative comparisons to the lidar wake measurements is to have spatially-varying transient flow inputs. The addition of the transient wind/flow information over the entire region of a wind farm has multiple benefits :

1. It helps in the accurate determination of the *tunable* parameters.
2. It provides a realistic representation of the turbine wake's propagation and evolution by incorporating the local fluid velocity at every vortex filament node.
3. Consequently, it accurately models the complex vortex dynamics and wake interactions, thereby improving the fidelity of the aeroelastic response of the waked rotors.
4. This leads to a holistic and accurate representation of all the multi-physics aspects - comprised of the aeroelastic behavior of the turbines, the vortex wake

interactions, the farm-collective and farm micro-grid controls, and finally the overall performance - of the wind farm.

Finally, in terms of the computational improvements, the current implementation maximizes computational performance using CPUs. However, the computations that form the bulk of the model are well-suited for GP-GPUs. A hardware system involving the twin-, 128-core CPU coupled with their compatible GP-GPUs would easily scale the simulation size to as many as 256 turbines $\sim$ more than twice the size of the largest currently envisioned commercial wind farms made up of wind turbines rated 5MW or higher.

These future efforts position CODEF to be well-suited for high-fidelity wind farm simulations that incorporate farm-collective and the electric micro-grid control strategies to optimize the overall output. It can be the perfect tool that can assist in the development of better informed, data-driven solutions in the global push towards diversifying sustainable renewable power generation and the move towards large, offshore farms in the very-near-future.

References

[1] IEC, . Wind turbine generator systems – part 13: Measurement of mechanical loads. Report IEC/TS 61400–13; International Electrotechnical Commission (IEC); 2001.

[2] Herges, T., Maniaci, D.C., Naughton, B.T., Mikkelsen, T., Sjöholm, M.. High resolution wind turbine wake measurements with a scanning lidar. In: Journal of Physics: Conference Series; vol. 854. IOP Publishing; 2017, p. 012021.

[3] IRENA, . Global energy transformation : A roadmap to 2050 (2019 edition). Tech. Rep.; International Renewable Energy Agency, Abu Dhabi; 2019.

[4] Dykes, K.L., Veers, P.S., Lantz, E.J., Holttinen, H., Carlson, O., Tuohy, A., et al. Iea wind tcp: Results of iea wind tcp workshop on a grand vision for wind energy technology 2019;doi:\bibinfo{doi}{10.2172/1508509}. URL https://www.osti.gov/biblio/1508509.

[5] Veers, P., Dykes, K., Lantz, E., Barth, S., Bottasso, C.L., Carlson, O., et al.

Grand challenges in the science of wind energy. Science 2019;366(6464):eaau2027. doi:\bibinfo{doi}{10.1126/science.aau2027}. https://www.science.org/doi/pdf/10.1126/science.aau2027; URL https://www.science.org/doi/abs/10.1126/science.aau2027.

[6] Glauert, H.. The analysis of experimental results in the windmill brake and vortex ring states of an airscrew. Tech. Rep. Reports and Memoranda Volume 1026; Great Britain Aeronautical Research Committee; 1926.

[7] Glauert, H.. Airplane propellers. In: Aerodynamic theory. Springer; 1935, p. 169–360.

[8] Manwell, J.F., McGowan, J.G., Rogers, A.L.. Wind energy explained: Theory, design and application. Chichester, UK: Wiley; 2009.

[9] Burton, T., Sharpe, D., Jenkins, N., Bossanyi, E.. Wind Energy Handbook. Chichester, UK: Wiley; 2001.

[10] Crawford, C.. Re-examining the precepts of the blade element momentum theory for coning rotors. Wind Energy 2006;9(5):457–478.

[11] Lanzafame, R., Messina, M.. Fluid dynamics wind turbine design: Critical analysis, optimization and application of {BEM} theory. Renewable Energy 2007;32(14):2291 – 2305.

[12] Leishman, J.G., Beddoes, T.S.. A generalised model for airfoil unsteady aerodynamic behaviour and dynamic stall using the indicial method. In: 42nd. Annual Forum of the American Helicopter Society, Washington D. C. 1986, p. 243–266.

[13] Griffin, D.A.. Blade system design studies volume I: Composite technologies for large wind turbine blades. Report SAND2002-1879; Sandia National Laboratories; 2002.

[14] Ponta, F.L., Otero, A.D., Lago, L.I., Rajan, A.. Effects of rotor deformation in wind-turbine performance: The dynamic rotor deformation blade element momentum model (drd–bem). Renewable Energy 2016;92:157–170.

[15] Otero, A.D., Ponta, F.L.. Structural analysis of wind-turbine blades by a generalized Timoshenko beam model. Journal of Solar Energy Engineering 2010;132:011015.

[16] Yu, W., Hodges, D.H., Volovoi, V., Cesnik, C.E.S.. On Timoshenko-like modeling of initially curved and twisted composite beams. Int J Sol and Struct 2002;39:5101–5121.

[17] Hodges, D.H.. Nonlinear Composite Beam Theory. Reston, Virginia: AIAA; 2006.

[18] Jonkman, J., Butterfield, S., Musial, W., Scott, G.. Definition of a 5-MW reference wind turbine for offshore system development. Tech. Rep. NREL/TP-500-38060; National Renewable Energy Laboratory; 2009.

[19] Jamieson, P.. Innovation in wind turbine design. Wiley; 2011.

[20] Crawford, C., Platts, J.. Updating and optimization of a coning rotor concept. Journal of Solar Energy Engineering 2008;130:031002.

[21] Menon, M., Ponta, F.. Dynamic aeroelastic behavior of wind turbine rotors in rapid pitch-control actions. Renewable Energy 2017;107:327–339.

[22] Otero, A.D., Ponta, F.L.. On the sources of cyclic loads in horizontal-axis wind turbines: The role of blade-section misalignment. Renewable Energy 2018;117:275–286.

[23] Xudong, W., Shen, W.Z., Zhu, W.J., Sorensen, J., Jin, C.. Shape optimization of wind turbine blades. Wind Energy 2009;12(8):781–803.

[24] Scully, M.. A method of computing helicopter vortex wake distortion. Massachusetts Institute of Technology, Aeroelastic and Structures Research ...; 1967.

[25] Landgrebe, A.J.. An analytical method for predicting rotor wake geometry. Journal of the American Helicopter Society 1969;14(4):20–32.

[26] Lamb, H.. Hydrodynamics 6th ed. Cambridge, UK: Cambridge University Press; 1932.

[27] Ponta, F.L.. Vortex decay in the kármán eddy street. Physics of Fluids 2010;22:093601.

[28] Kelley, C.L.. Aerodynamic design of the national rotor testbed. Tech. Rep.; Sandia National Lab.(SNL-NM), Albuquerque, NM (United States); 2015.

[29] Mikkelsen, T., Angelou, N., Hansen, K., Sjöholm, M., Harris, M., Slinger, C., et al. A spinner-integrated wind lidar for enhanced wind turbine control. Wind Energy 2013;16(4):625–643.

[30] Sjöholm, M., Pedersen, A.T., Angelou, N., Abari, F.F., Mikkelsen, T., Harris, M., et al. Full two-dimensional rotor plane inflow measurements by a spinner-integrated wind lidar. In: European Wind Energy Association Conference. 2013,.

[31] Machefaux, E., Larsen, G.C., Troldborg, N., Hansen, K.S., Angelou, N., Mikkelsen, T., et al. Investigation of wake interaction using full-scale lidar measurements and large eddy simulation. Wind Energy 2016;19(8):1535–1551.

[32] Horváth, Z.L., Bor, Z.. Focusing of truncated gaussian beams. Optics communications 2003;222(1-6):51–68.

[33] Angelou, N., Mann, J., Sjöholm, M., Courtney, M.. Direct measurement of the spectral transfer function of a laser based anemometer. Review of scientific instruments 2012;83(3).

[34] Herges, T.G., Maniaci, D.C., Naughton, B., Hansen, K., Sjoholm, M., Angelou, N., et al. Scanning lidar spatial calibration and alignment method for wind turbine wake characterization. In: 35th wind energy symposium. 2017, p. 0455.

[35] Barone, M.F., White, J.. Doe/snl-ttu scaled wind farm technology facility. Tech. Rep.; Sandia National Lab.(SNL-NM), Albuquerque, NM (United States); 2011.

Appendix A

Copyright Agreements

Figures 5.3, 5.7, and 5.11 from chapter 5 is adopted from [2]. Content from [2] may be used under the terms of the Creative Commons Attribution 3.0 license. Under this license, permission is granted to

1. **Share** - copy and redistribute the material in any medium or format for any purpose, even commercially
2. **Adapt** - remix, transform, and build upon the material for any purpose, even commercially

Under the following terms:

1. **Attribution** - You must give appropriate credit, provide a link to the license, and indicate if changes were made. You may do so in any reasonable manner, but not in any way that suggests that the licensor endorses you or your use.

2. **No additional restrictions** - You may not apply legal or technological measures that legally restrict others from doing anything the license permits.

ATTRIBUTION: Figures 5.3, 5.7, and 5.11 were adopted from [2]. The figures have been resized to fit the portrait layout of this dissertation. No other changes have been made. The source for these figures is doi :10.1088/1742-6596/854/1/012021 and the license can be found in Creative Commons Attribution 3.0 licence.